Monthly Scientific-Technical and Production Journal

The Paton WELDING JOURNAL

October 2001 # 10

English translation of the monthly «Avtomaticheskaya Svarka» journal published in Russian since 1948

The National Academy of Sciences of Ukraine
The E.O. Paton Electric Welding Institute of the NAS of Ukraine
International Association «Welding»

«The Paton Welding Journal»
is published monthly by the International Association «Welding»

Promotion group:
V.N.Lipodaev, V.I.Lokteva
A.T.Zelnichenko (exec. director)
Translators:
S.A.Fomina, I.N.Kutianova,
T.K.Vasilenko
Editor
N.A.Dmitrieva
Electron galley:
I.V.Petushkov, T.Yu.Snegireva

Editorial and advertising offices
are located at PWI,
International Association «Welding»,
11, Bozhenko str., 03680,
Kyiv, Ukraine
Tel.: (38044) 227 67 57
Fax: (38044) 268 04 86
E-mail: journal@paton.kiev.ua

State Registration Certificate
KV 4790 of 09.01.2001

Subscriptions:
$460, 12 issues per year,
postage and packaging included.
Back issues available

«The Paton Welding Journal» Website:
http://www.nas.gov.ua/pwj

CONTENTS

DEAR PROFESSORS, ASSOCIATES AND STUDENTS OF THE EAST-UKRAINIAN NATIONAL UNIVERSITY!

Your institution was the first in Donbas to start training machine engineers in 1921, and during 80 years since its foundation has transformed from the Engineering Institute into one of the leading universities of Ukraine. The Siberia largest higher education institution, now the Omsk State Technical University, was established on the base of the Institute, which had been evacuated there during the Great Patriotic War. The East-Ukrainian University was established in 1993 on the base of the Lugansk Engineering Institute and a number of higher education establishments of the Lugansk district. At present, the University provides education in 107 specialities of liberal, economic, natural, social and technical fields of knowledge. During 80 years it has trained more than 100,000 highly skilled specialists. 1200 masters and 31 Ph.D. have been trained in the last years for 70 countries worldwide.

The University is active in fundamental and applied research and provides postgraduate studies for scientific and scientific-pedagogical staff. The University is a leading scientific-methodical centre, while in its structure it is oriented to practical implementation of the stepwise education in Ukraine. Owing to a high level of the staff and logistical support, the University successfully meets the needs for specialists in the sphere of economics and state structures of the Lugansk and other districts of Ukraine.

The University continues to successfully develop training of technical specialists. The Welding Chair has educated more than 1500 welding engineers for more than 35 years. Many of them became the leading specialists and managers of major enterprises and organizations of Ukraine, as well as far- and near-foreign countries. Welding engineers, the graduates of your University, are the key specialists of welding production at such large-scale enterprises of the Lugansk district as the Association «Luganskteplovoz», Stakhanov Car Building Works and others. Since 1999 the University has started training students in speciality «Technology and Equipment for Repair and Increase of Wear Resistance of Machines and Structures».

The E.O. Paton Electric Welding Institute is constantly strengthening contacts and rendering assistance to the scientific-pedagogical staff of higher education institutions, including your University, in conducting research, providing advanced scientific-and-technical information in the field of welding and related technologies and training the scientific-pedagogical staff. Professors and associates of the University participate in conferences and seminars held by the E.O. Paton Electric Welding Institute and systematically publish results of their research in the «Avtomaticheskaya Svarka» Journal. This issue of the Journal includes a selection of articles written by professors and associates of the University on the basis of results of their recent research.

The E.O. Paton Electric Welding Institute of the National Academy of Sciences of Ukraine and the editorial board of the «Avtomaticheskaya Svarka» Journal heartily congratulate the teaching staff, students and associates of the East-Ukrainian National University with the eightieth anniversary since its foundation. We wish you all happiness, good health and new achievements in educating highly skilled specialists in all scientific areas, including welding and related technologies, as well as creative success and progress in the field of fundamental and applied research.

Boris E. Paton

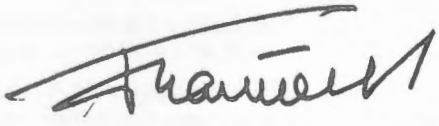

FEATURES OF STRESSES AND DEFORMATIONS DEVELOPING IN WELDED JOINTS OF CORROSION-RESISTANT 10Kh13G18D STEEL

A.I. GEDROVICH and **I.A. GALTSOV**
East-Ukrainian National University, Lugansk, Ukraine

ABSTRACT

Features of formation of stresses and deformations in welding corrosion-resistant steel of 10Kh13G18D grade are described. Kinetics of phase-structural transformations in the process of welding and in the post-welding period is given. Most typical structurally-stressed zones of the metal welded are distinguished.

Key words: *welding, stress, deformation, thermo-deformational cycle, phase, corrosion-resistant steel, austenite, ferrite, plastic deformation zone*

Corrosion-resistant steel of 10Kh13G18D grade (TU 14-4-435–98) is used in fabrication of diesel-multiple-unit trains in «Lugansk teplovoz» Works. Casing sheet thickness of 1.7 mm is specified to reduce the carriage weight. During fabrication of the carriage side wall, casing sheets are joined to a rigid frame, using butt, fillet and plug joints (Figure 1).

Total length of welds, made during the casing forming, is 85 m on one side wall and 650 m on the entire carriage.

A large number of welds and their considerable length, promote formation of residual stresses and deformations, that distort the design dimensions of the item (up to 180 mm sagging, when side walls are made) and require considerable expenses for assembly and postweld treatment (impact and impact-free straightening), the cost of which is up to 30 – 40 % of the overall fabrication cost.

Physical properties of 10Kh13G18D* and St.3** steels

Physical properties	*10Kh13G18D*	*St.3*
Density, $\rho \cdot 10^3$, kg/m^3	7.90	7.85
Melting temperature, °C	1400 – 1450	1500
Heat conductivity at 100 °C, W/(m·K)	0.16	0.39
Coefficient of linear expansion, $\alpha \cdot 10^{-6}$, at the temperature from 0 up to 100 °C	16.6 – 20.0	12.0
Electrical resistance at 20 °C, Ohm·mm^2/m	0.73	0.15
Temperature of the start of intensive formation of scale, °C	850 – 900	550
Magnetic properties	Nonmagnetic	Magnetic

*C – 0.1; Cr – 13.0; Mn – 18.0; Cu – 1.0 wt.%; Fe – balance.
**C – 0.14 – 0.22; Mn – 0.3 – 0.6; Si – 0.05 – 0.17; S – up to 0.05; P – up to 0.04 wt.%; Fe – balance.

Welding, as a technology of making permanent joints, is characterised by a highly local input of heat energy into the metal. The thermo-deformational cycle of welding induces residual welding deformations and stresses in the parts and components. The latter in stainless austenitic steels can greatly exceed the material yield point [1]. This is further promoted by the fact that stainless austenitic steels have a low coefficient of heat conductivity, high coefficient of linear expansion and are prone to hardening (Table).

The aim of this work consisted in experimental investigation of plastic deformation distribution in the weld zone, evaluation of the level of residual stresses, phase transformations of weld and HAZ metal during the thermo-deformational cycle of welding and after welding.

Formation of residual deformations and stresses, as well as the level of phase transformations in stainless austenitic steels, are affected by plastic deformation, developing during welding and subsequent cooling [1, 2].

In welding a number of phase transformations proceed in the weld and HAZ metal, the level of which is determined by the factors, affecting the development of plastic deformation (welding modes, metal cooling rate, etc.). The structure of corrosion-resistant steels is characterised by the following phases: austenite, carbide, ferrite and martensite. The latter three have ferromagnetic properties, and austenite has

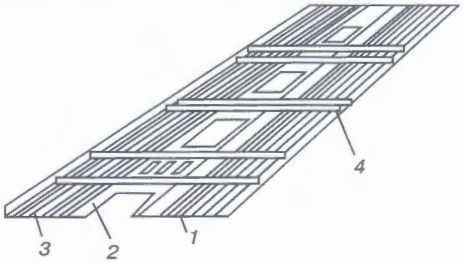

Figure 1. Elements of side wall casing: *1* – 7-bead corrugated profiled sheet, forming the bottom part; *2* – casing corrugated sheet, forming the window openings; *3* – 3-bead corrugated profiled sheet, forming the upper part; *4* – rigid frame

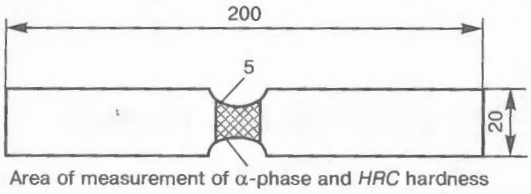

Figure 2. Specimen for tensile mechanical testing

paramagnetic properties. Primary magnetic properties of the metal (saturation magnetisation) depend on phase composition and crystalline lattice type, and, therefore, their study will yield data, necessary for plotting the equilibrium diagrams of the metal at plastic deformation. Therefore, change of saturation magnetisation of the item is recorded at the change of phase composition or phase structure of the weld and HAZ metal [3].

Specific magnetisation usually depends on metal composition, stress level and plastic deformation. Composition of single-phase paramagnetic metal of the weld and the HAZ can be determined from a graph, plotted in the co-ordinates of metal specific magnetisation–deformation (stress).

Mechanical tensile testing of 1.7 × 20 × 200 mm flat specimens with a soft Mesnager stress raiser, R = = 5 mm, in the specimen center (Figure 2), was performed in R-5 tensile testing machine, in order to simulate the deformations and stresses, arising in the weld and the HAZ metal in welding. Testing demonstrated that plastic deformation is localised at the stress raiser and is accompanied by phase transformations of γ-austenite into α-ferrite (with α-ferrite content of up to 12 % at rupture).

Mechanical testing, according to GOST 1497–84, revealed that the yield point of this steel is 435 MPa, ultimate strength is 760 MPa and relative elongation is 25 – 30 %.

Investigation of the zone of plastic deformations (between the stress raisers) at varying load (measurement error up to ±2 %), using flux-gate pole finder FP-1M and FA-1M ferrite meter, demonstrated that phase transformation with α-ferrite formation developed at applied tensile stresses above σ_y of the metal equal to 430 MPa, and had a non-linear dependence (Figure 3).

The conducted experiments demonstrated, that magnetic α-phase forms only in the zone of tensile stresses, since austenite, having a face-centered lattice of γ-iron, is characterised by a higher density and smaller specific volume, than ferrite with a less

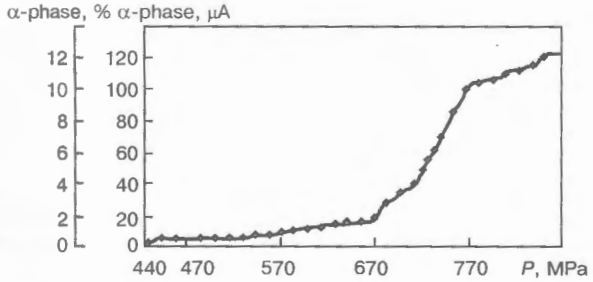

Figure 3. Dependence of α-phase appearance on applied tensile load P

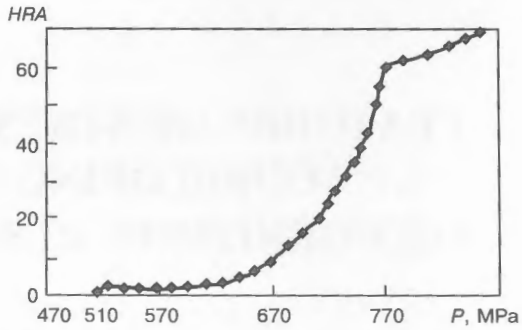

Figure 4. Dependence of the increase of specimen *HRA* hardness on the applied tensile load

densely packed lattice of α-iron [4]. At tensile plastic deformation, the dense lattice of α-phase is rather easily rearranged into a less dense one. At compressive plastic deformation no noticeable change of γ-phase lattice density is observed [5]. Plastic deformation causes austenitic grain fragmentation, block refinement and increase of their disorientation angle.

At specimen hardness measurement by the Rockwell method (GOST 9013–59), it was found that the metal in the stress concentrator zone is greatly strengthened from *HRA* 50 (before load application) up to *HRA* 69 – 71 (after rupture) (Figure 4), this being indicative of formation of ε-martensite of deformation. Higher susceptibility of chromium-manganese austenite to martensite transformation at deformation, is related to a low energy of stacking faults, that are the nuclei of the crystals of ε- and α-martensite of deformation.

Austenite-martensite transformation is characterised by rearrangement of the lattice, without changing the concentration of the reacting phases. Since it is diffusionless, carbon does not precipitate from the solution, and just the rearrangement of iron atoms occurs during transformation. Located in austenite in the form of a face-centered cube, they are redistributed during transformation, into a body-centered lattice, this being accompanied by increase of the metal volume by 1.0 – 1.5 % [4]. Appearance of ε-martensite of deformation and decrease of the indi-

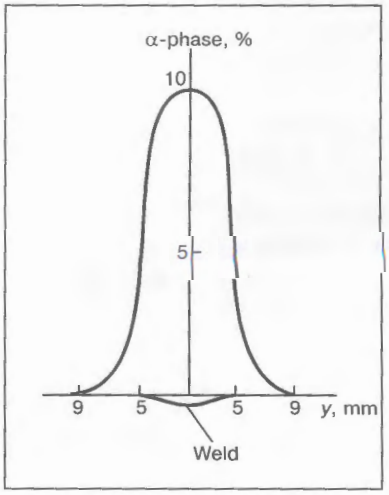

Figure 5. Distribution of α-phase over the cross-section of a welded specimen in the weld and HAZ metal

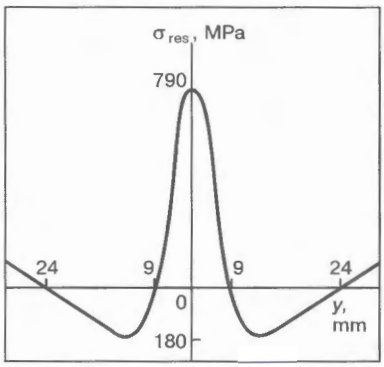

Figure 6. Kinetics of distribution of residual stresses in the welded joint

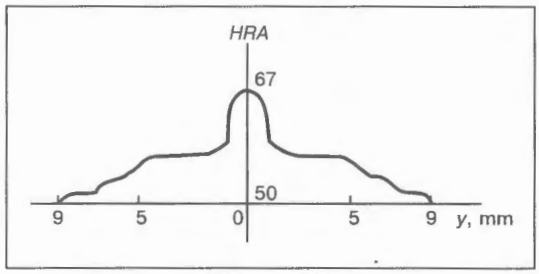

Figure 7. Dependence of distribution of *HRA* hardness in the weld and HAZ metal

ces of austenitic γ-properties are characterised by phase transformation equation $\gamma \rightarrow \varepsilon \rightarrow \alpha$.

In order to study the features of stress and deformation development in welded structures, the process of carriage welding was simulated on sheets of 10Kh13G18D stainless steel of 1.7 × 220 × 450 mm size in the jig (to provide the required rigidity).

After welding a specimen of this steel in argon (I_a = 40 A, U_a = 19 V, v_w = 16 – 17 m/h) with Sv-08Kh20N9G7T (C – 0.8; Cr – 20.0; Si – 0.5; Mn – 7.0; Ni – 9.0; Ti – 0.8 wt.%) wire of 1.2 mm diameter, its complete cooling and removal from the jig, it was found that the content of α-phase could be up to 9 – 10 % in the weld and HAZ metal (Figure 5), then it abruptly dropped to zero across the specimen width (non-linearly). The width of the zone, containing α-phase, was 8 – 9 mm after welding.

The residual stress field in the welded specimen is characterised by a high level of tensile stresses σ_{res} = = 785 MPa and their considerable gradient across the width (Figure 6).

The thermo-deformational cycle of welding results in hardness increase from *HRA* 50 (before welding) up to *HRA* 65 – 67 (after welding) in the weld and HAZ metal (Figure 7).

After complete cooling of the specimen and its removal from the jig, its deformation was observed. Maximal deformation (sagging) occurs in the first 10 min after taking the specimen out of the jig and is f = 11.2 mm on 220 mm base.

During storage of welded specimens of the above steel, the residual stress field, deformations and phase-structural composition of the metal do not remain stable, the level of residual welding stresses is reduced by 10 % of the initial value, and the amount of α-phase in the weld and HAZ metal is also changed. Both the processes proceed in a synchronous manner. Stress relaxation with increase of deformation (up to f_{rel} = = 12 mm), drop of the residual stress level (σ_{res} = = 680 MPa) and lowering of α-ferrite content (to 7.5 %) proceed for 72 h.

The relaxation process running is due to the reverse process of phase-structural $\alpha \rightarrow \varepsilon \rightarrow \gamma$ transformation, accompanied by a change of the degree of martensite tetragonality, and also its partial decomposition, reduction of ferritic α-phase and recovery of austenitic γ-properties of the material, this, in its turn, promoting activation of tensile stresses, accumulated by the weld and the HAZ metal, lowering of their level and increase of material deformability.

Analysis of residual stress epure and qualitative content of α-phase, as well as the results of integrated study of the process of deformation with time of welded joints on austenitic steel of 10Kh13G18D grade, allows the following most characteristic structurally-stressed zones to be distinguished (Figure 8):

- zone *1* – maximal tensile stresses. The metal of the weld and the HAZ (~ 8 mm width) is in the plastic deformation zone. The level of maximal tensile stresses is 785 – 790 MPa. Maximal content of α-phase is 9 – 10 %;
- zone *2* – maximal compressive stresses (~ 4 mm length). Located in base metal, undergoing plastic deformation during the thermo-deformational cycle of welding. The level of maximal compressive stresses is 180 MPa, no α-phase detected;
- zone *3* – compressive stresses. Located in the base metal, not undergoing plastic deformation in welding. The level of maximal compressive stresses is 150 MPa (zone length is ~ 12 mm), no α-phase found;
- zone *4* – tensile stresses. Located in the base metal outside the plastic deformation zone. The level of maximal tensile stresses is 85 MPa, maximal content of α-phase is 0.5 – 0.7 % at ~ 6 mm length.

Based on the derived experimental data, it should be noted that the maximal tensile residual stresses were found in zone *1*. They are one of the main con-

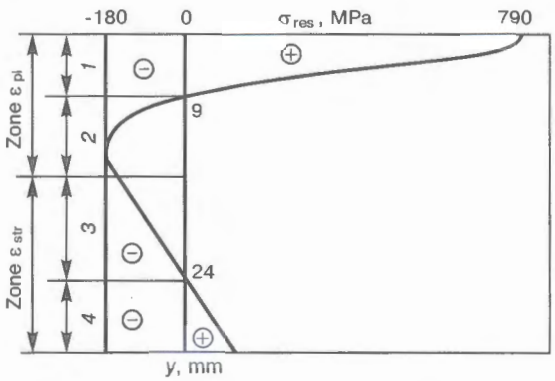

Figure 8. Characteristic structurally-stressed zones of the welded specimen

ditions of phase transformations of austenite, by their level they are 1.6 – 1.8 times higher, than the material relaxation limit, and their reduction after welding (during storage) is maximal. In addition, in this zone after the thermo-deformational cycle of welding, α-phase content is maximal, compared to other zones, alongside the high level of tensile residual stresses, and it changes during storage. In the other three zones, the level of residual welding stresses is 2 – 3 times lower, than the material relaxation limit, and the drop of their level during storage is slight, whereas no change of α-phase content was found during the entire period of storage. All this leads to the conclusion, that zone *1* is the main source of deformations of the entire welded joint with time.

CONCLUSIONS

1. Deformation of welded structures, related to structural transformations, is the result of the impact of thermal cycle of welding in individual zones of the welded joint and formation of unstable structures in them. After welding, the zones with unstable structure, develop structural transformations, inducing additional inherent stresses, that deform the structure.

2. With the increase of residual stresses, α-phase content grows with a continuously rising gradient. Applying different methods to change the level of residual stresses formed during the process of irreversible plastic deformations of the weld and HAZ metal, it is possible to change to a certain extent, the content of α-phase, as one of the main factors, determining the dimensional stability and other important service properties of the item.

REFERENCES

1. Sagalevich, V.M., Saveliev, V.F. (1986) *Stability of welded joints and structures*. Moscow: Mashinostroyeniye.
2. Gedrovich, A.I. (1998) *Plastic deformation in welding*. Lugansk: EUSU.
3. Kostin, P.P. (1990) *Physico-mechanical testing of materials and alloys and non-metallic materials*. Moscow: Mashinostroyeniye.
4. Papsuev, N.N. (1988) *Deformation in welding ship structures*. Leningrad: Sudostroyeniye.
5. Goldshtein, M.I., Grachev, S.V., Veksler, Yu.G. (1985) *Special steels*. Manual for higher educational establishments. Moscow: Metallurgia.

THEORETICAL ESTIMATION OF EFFECT OF ELECTRON BEAM PARAMETERS ON THE FORMATION OF ROOT DEFECTS IN EBW

Yu.I. STATYVKA and **V.A. SHEVCHENKO**
East-Ukrainian National University, Lugansk, Ukraine

ABSTRACT

The effect of electron beam geometric parameters on non-uniformity of penetration depth in case of welding at external disturbance and without it is considered. Theoretical results have a good correlation with experimental data.

Key words: *electron beam welding, vapour-gas channel, non-uniformity of penetration depth, probability model, beam focusing, beam scanning*

EBW is the promising method of joining materials [1, 2] owing to its unique property of a single-pass deep penetration in spite of the problems of providing stability of the weld formation, in particular depth of penetration.

In the EBW theory the mathematical models of a deep penetration of metal and a formation of the vapour-gas channel have been developed [3 – 8]. At the same time, when the processes of formation of root defects are described in the up-to-date publications, a number of the important factors are not taken into consideration. Usually, the stability of the vapour-gas channel to different disturbances is studied and the problem of estimation of the amplitude of variation in the penetration depth (root defects) depending on the parameters of the technological process is not put forward. Thus, the authors of [9 – 12] give the relations, coming from the theoretical consideration of the problem, that makes it possible to select the optimum frequency of a circular beam scanning. However, the relations for estimation of the amplitude of variation of the penetration depth, frequency and probability of formation of root and other typical defects of deep penetration are determined from the experimental results. The authors of [13] suggest a mathematical model for the estimation of the amplitude of variation of the penetration depth in case of welding with an vibrating action on the weld pool, but only at the condition that the optimum frequency of this action was selected.

Therefore, the problem of development of the mathematical models of the process of formation of root defects remains actual.

In [14] the problem of screening a conical electron beam with the melt disturbances, uniformly distributed along its axis, was investigated. The relations

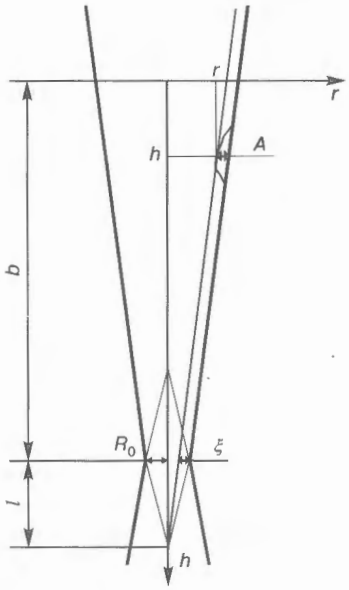

Figure 1. Scheme of electron beam screening by the melt in a gas-vapour channel

were obtained for the density of distribution and mathematical expectation of the amplitude of the disturbances projections on the plane of the minimum section of the beam depending on its geometry and depth of penetration.

Let us consider the problem about the non-uniformity of the penetration depth at screening of the conical electron beam (Figure 1). In Figure R_0 denotes a minimum radius of the electron beam; A is the amplitude of a screening element; ξ is the projection of the screening element on the plane of the beam minimum section; b is the depth of a minimum beam section; l is the distance from the beam minimum section to its focal plane; h and r are the coordinates of the screening element.

Let us find the projection of the amplitude of the screening element A on the plane of the beam minimum section. It is evident from the geometric relations that

$$\xi = \frac{Al}{l + |b - h|}. \tag{1}$$

To model the wider class of situations, it was assumed that the melt disturbances, screening the electron beam, are distributed in the depth with a density of a beta-distribution $H(h)$ [15]:

$$H(h) = \frac{\Gamma(\alpha + \beta)}{\Gamma(\alpha)\,\Gamma(\beta)} \left(\frac{h - h_1}{h_2 - h_1}\right)^{(\alpha - 1)} \left(1 - \frac{h - h_1}{h_2 - h_1}\right)^{(\beta - 1)}, \tag{2}$$

where Γ is the gamma-function; α, β are the parameters of beta-distribution; h_1, h_2 are the intervals of depths where the screening occurs. Using expression (2) at $\alpha \geq 1$, $\beta \geq 1$ it is convenient to model the distribution of the screening elements at the length $[h_1, h_2]$ in the depth of the vapour-gas channel: uniform at $\alpha = \beta = 1$, concentrated largely in root, upper or middle part of the channel at $\alpha < \beta$, $\alpha > \beta$ and $\alpha = \beta$.

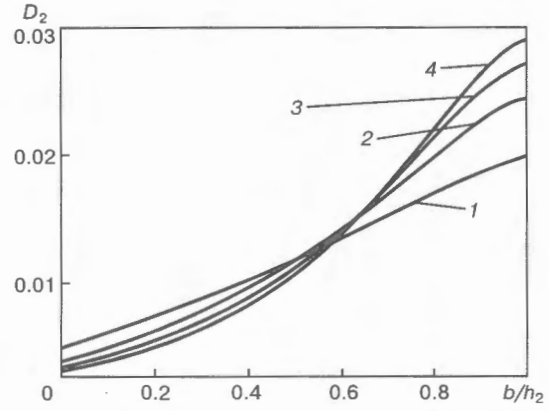

Figure 2. Dependence $D_2(b, h_2)$ at $\gamma = 0.01$ rad and different α and β: *1* — $\alpha = 1, \beta = 1$; *2* — $\alpha = 2, \beta = 1$; *3* — $\alpha = 3, \beta = 1$; *4* — $\alpha = 1, \beta = 1$

If the disturbances of amplitude A = const are distributed in height with density $H(h)$, then the mathematical expectation m_2 of the square of the beam minimum section, proportional to the energy being screened, can be found as

$$m_2 = \int_{h_1}^{h_2} \xi^2 H(h)\,dh. \tag{3}$$

At $h_1 = 0$ taking into account of equations (1) and (2) we shall find

$$m_2 = \frac{lA^2(lh_2 + 2h_2b - 2b^2)}{(l + b)\,(l + h_2 - b)h_2}.$$

It can be expected that in one act of the screening the electron beam is overlapped by a disc of radius $\sqrt{m_2}$ in the plane of the minimum section.

The screening of the beam with the melt disturbances occurs at different depth [3, 5, 6], however, the significant changes in the front of melting take place only in the root part of the vapour-gas channel. Let us find the ratio m_2, proportional to the screening beam power with disturbances, to the square of radius of a perfect electron beam R_n in the depth h_2. It follows from Figure 1 that

$$R_n = R_0\,(l + |h_2 - b|)/l.$$

Figure 2 shows relationship

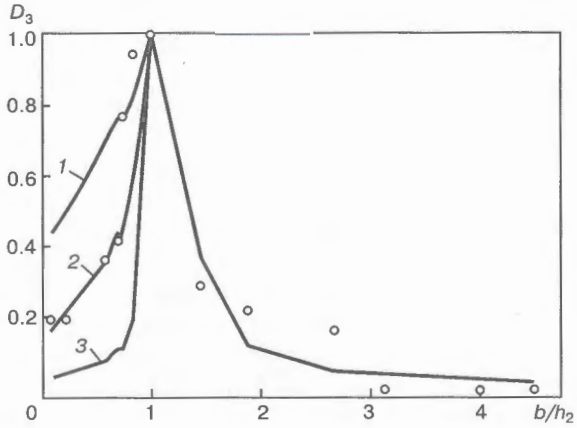

Figure 3. Comparison of estimated and experimental data [16]

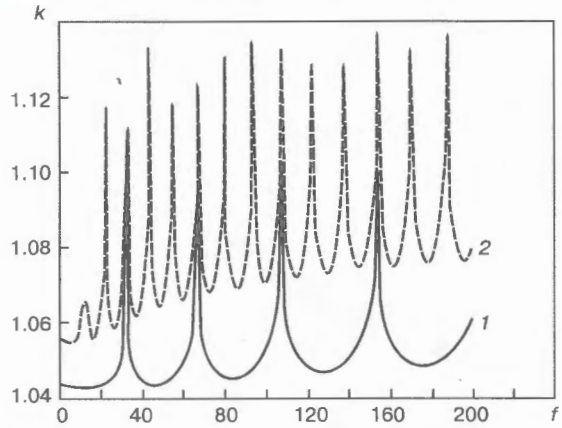

Figure 4. Dependence of a stability factor on the frequency of scanning f for h_2 = 10 (*1*) and 30 (*2*) mm at R_{scan} = 0.5 mm

$$D_2 = \frac{m_2}{R_n^2} \quad \text{on} \quad b/h_2.$$

The value D_2 can be interpreted as a fraction of the beam area in the root part of the vapour-gas channel, proportional to its energy which is screened by the melt disturbances. At all the $b \le h_2$ the value D_2 reaches the highest value at $b/h_2 = 1$ independently of the parameters of distribution of disturbances in the depth of penetration.

Thus, the obtained theoretical relations describe appropriately the fact, well-known from experimental investigations, about the highest variations of the penetration depth at a spike shape of penetration which is produced, as a rule, when the plane of the minimum section of the electron beam is located in the weld root part [3, 6, 16].

To compare with experimental data of [3, 16] the value D_3 was used:

$$D_3 = \frac{D_2(b,\ h_2)}{D_2(b = h_2,\ h_2)}.$$

The Figure 3 presents the dependence of D_3 on b/h_2 at a uniform distribution of screening elements of the melt in the depth of the vapour-gas channel ($\alpha = \beta = 1$) for values of the angle of convergence γ of beam being equal to 0.01, 0.03 and 0.05 rad (curves *1* – *3*, respectively). Points are the experimental data for titanium alloy VT6 [3, 16] plotted as a dependence of $\Delta h_1/\Delta h_{b=h_2}$ on b/h_2. The values D_3 were calculated for the experimental data b and h_2 at R_0 = 0.7 mm and unchanged amplitudes A of disturbances in all the experiments. The given data illustrate the quality coincidence of estimated and experimental values.

Value m_2, determined from formula (3), can be also used in modelling of root defect formation in case of welding at an external action on the weld pool.

Let q be the mean specific power of the beam. Then, the value $q\pi m_2$ can be used as m_Δ, i.e. mathematical expectation in decrease of beam power in the root of the vapour-gas channel in one event of screening within the scope of the probability model of formation of the weld root [17] based on the scheme of the fractional process. Figures 4 and 5 show the results

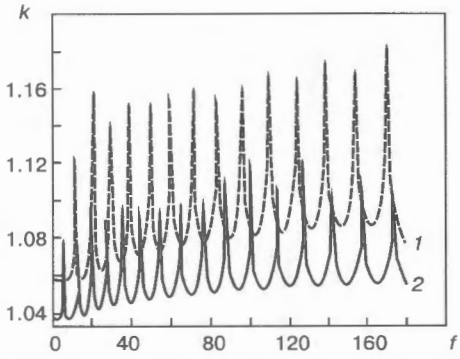

Figure 5. Dependence of a stability factor on the frequency of scanning f for R_{scan} = 0.3 (*1*) and 0.7 (*2*) mm at h_2 = 30 mm

typical of this model in case of use of $m_\Delta = q\pi m_2$ in welding with a circular scanning of the electron beam of radius R_{scan}. Weld stability factor $k = \dfrac{h_{max}}{h_{max} - \Delta h}$, where h_{max} is the largest depth of penetration in root defects and Δh is the height of the root defect, is taken as a value, characterizing the non-uniformity of the penetration depth. The calculations were made for aluminium. It is seen that the increase in the penetration depth or decrease in amplitude of the beam scanning leads to the increase in amplitude of the root defects and more dense location of natural frequencies of vibration of the molten metal in the weld pool. The calculations were made at $A = 0.1R_0$, $b = 0.3h_2$, R_0 = 1 mm, γ = 0.01 rad at the mentioned radius of beam scanning R_{scan} and maximum depth of penetration h_2. The thickness of the melt at the front wall of the weld pool was taken equal to 0.5 mm.

CONCLUSIONS

1. Method of analytical estimation of a fraction of the electron beam energy being screened by the disturbances of the melt in the gas-vapour channel has been developed, that makes it possible to estimate the non-uniformity of the penetration depth.

2. The relationships were obtained within the scope of the probability model of formation of root defects using the schemes of the fractional process for determination of the non-uniformity of the depth of penetration, taking into account the focusing, radius and frequency of the circular scanning of the electron beam.

REFERENCES

1. Paton, B.E. (1999) Problems of welding at the transition of centuries. *Avtomaticheskaya Svarka*, **1**, 4 – 14.
2. Paton, B.E. (2001) Modern electron beam technologies of the E.O. Paton Electric Welding Institute of NAS of Ukraine. *The Paton Welding Journal*, **2**, 2 – 7.
3. Nazarenko, O.K., Kajdalov, A.A., Kovbasenko, S.N. *et al.* (1987) *Electron beam welding*. Kyiv: Naukova Dumka.
4. Rykalin, N.N., Uglov, A.A., Zuev, I.V. *et al.* (1985) *Laser and electron beam treatment of materials*. Handbook. Moscow: Mashinostroyeniye.
5. Leskov, G.I., Trunov, E.N., Zhivaga, L.I. (1976) Shape, sizes and stability of vapour-dynamic channels in metal during electron beam welding. *Avtomaticheskaya Svarka*, **6**, 13 – 17.
6. Leskov, G.I., Zhivaga, L.I. (1978) Melting of thick metals in welding with a conical electron beam. *Ibid.*, **4**, 11 – 14.

7. Olshansky, N.A., Gururadzha, G.D. (1972) Determination of depth of penetration in electron beam welding. *Ibid.*, **8**, 11 – 12.
8. Tochilkin, V.A. (1983) About the model of vapour-gas channel in beam welding. In: *Proc. of VIII All-Union Conf. on Electron Beam Welding*. Moscow: MEI.
9. Shilov, G.A., Akopiantz, K.S., Kasatkin, O.G. (1983) Effect of frequency and diameter of circular scanning of electron beam on metal penetration in EBW. *Avtomaticheskaya Svarka*, **8**, 25 – 28.
10. Akopiantz, K.S. (1984) Prevention of formation of root defects in electron beam welding. *Ibid.*, **6**, 59 – 61.
11. Akopiantz, K.S., Shilov, G.A. (1985) Effect of circular scanning of electron beam on the prevention of root defects in welding. In: *Proc. of Int. Conf. on Electron Beam Technologies*, Varna, 26 May – 2 June. Sofia: Inst. for Electronics.
12. Shilov, G.A., Akopiantz, K.S., Kovbasenko, S.N. (1983) Selection of optimum of focusing and beam scanning in EBW of steels of up to 130 mm thickness. In: *Proc. of VIII All-Union Conf. on Electron Beam Welding*. Moscow: MEI.
13. Shevchenko, A.V., Naser, M. (1992) *Model of process of weld formation in EBW with a deep penetration*. Lugansk: LMSI.
14. Statyvka, Yu.I., Shevchenko, V.O. (2000) Screening of conical beam by melt disturbance in EBW. *Visnyk SUDU*, **5**, 224 – 229.
15. Korolyuk, V.S., Petrenko, N.I., Skorokhod, A.V. *et al.* (1985) *Handbook on theory of probability and mathematical statistics*. Moscow: Nauka.
16. Nazarenko, O.K., Kajdalov, A.A., Lokshin, V.E. *et al.* (1975) Effect of electron beam focusing on stability of weld depth in welding alloys AMg6 and VT6. *Avtomaticheskaya Svarka*, **2**, 72 – 73.
17. Statyvka, Yu.I., Shevchenko, V.O. (2000) Mathematical modelling of process of weld formation in EBW. *Visnyk SUDU*, **9**, 202 – 208.

FORECASTING RESIDUAL DEFORMATIONS IN WELDING WITH FORCED COOLING

A.I. GEDROVICH and **A.B. ZHIDKOV**
East-Ukrainian National University, Lugansk, Ukraine

ABSTRACT

Approach is described for determination of sizes of active zone and residual deformations and also their maximum possible reduction in welding with cooling of different types of welded joints.

Key words: *welded joints, welding with forced cooling, deformation, residual stresses, yield strength, plastic deformation zone*

Considering the current level of welding fabrication, production of welded structures, with distortions not exceeding the tolerances, involves certain difficulties. Postweld straightening often does not allow complete elimination of residual deformations, and for complicated three-dimensional structures, it is practically not applicable. Other known methods of residual deformation elimination also involve considerable expenses, or can be used just for limited classes of structures. Therefore, the most promising is the use of distortion-free welding and one of its variants, namely welding with forced cooling, as the processes, allowing achievement of minimal residual deformations within the tolerance limits, after post-weld treatment [1].

The process of welding with forced cooling was studied by many foreign and local researchers, including the staff of E.O. Paton Electric Welding Institute, NTUU «Kiev Polytechnic Institute», etc. [2, 3]. This process, however, did not become widely accepted in industry, as many of its aspects remained unstudied.

It is known [4 – 6], that the level of residual stresses and deformations in welded structures depends on the dimensions of the plastic deformation zone (active zone). One of the methods of controlling them is forced cooling during welding. There exist a great number of various methods of cooling during welding, that lead to reduction of the above dimensions and have, based on the published data, different adaptability to fabrication and effectiveness. Application of a particular kind of cooling is governed by the welding process (automatic, manual, submerged-arc, etc.), properties of the material being welded, item cost, batch size and production conditions, etc. Study [7] reports an up to 70 % reduction of the active zone dimensions. In this case, investigations were conducted for low-carbon steels 1 – 3 mm thick, as thin sheets are the most prone to deformation. For butt joints of up to 3 mm thick metal, residual stresses and deformations for the main cooling processes are calculated by the known dependencies [5] through the shrinkage force, found from the nomogram (Figure) with different degrees of the active zone reduction. Up to now, however, limit dimensions of the active zone, with regard to the concrete types of

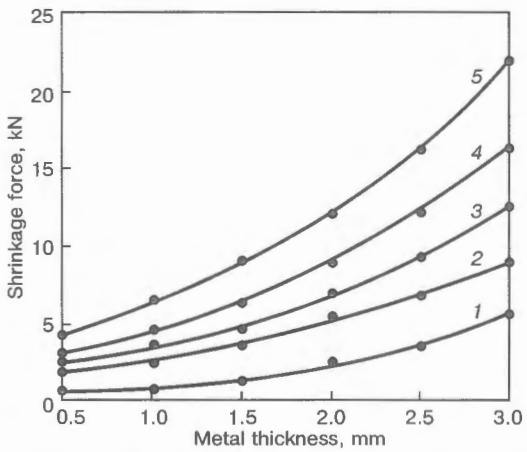

Nomogram for determination of shrinkage force in the case of butt- and zero-gap welding with cooling at different degrees of reduction of the active zone dimensions: *1* — minimum; *2* — 30; *3* — 50; *4* — 70 %; *5* — maximum

Table 1. Cross-sectional area of welds

Joint type							
Butt		*Fillet*		*Tee*		*Overlap*	
Designation	*Area, mm²*	*Designation*	*Area, mm²*	*Designation*	*Area, mm²*	*Designation*	*Area, mm²*
B1	13.3	F1	8.3	T1	7.8	O1	7.8
B2	11.4	F2	14.0	T3	2.0 × 7.8	O2	2.0 × 7.8
B4	20.5	F4	12.1	T6	7.5		
B5	13.6	F5	6.0 + 4.0	T7	7.5 + 4.0		
B7	2.0 × 9.0	F6	8.8				
B8	8.3	F9	8.6				
B9	12.2	F10	8.4 + 4.0				
B10	8.8						
B12	8.8 + 4.0						

welded joints, have not been determined in welding with cooling. This paper fills up the gap.

In the general case, it can be assumed, that residual stresses inside the active zone, are equal to the yield strength, then the shrinkage force can be determined from the specimen cross-sectional area that is inside the active zone. This area consists of two parts: area occupied by the weld and the HAZ, where the stresses are equal to the yield strength. The first can be regarded as constant, since the geometrical dimensions of the weld are determined from appropriate State Standards of Ukraine, and the area of the HAZ zone, in which the stresses are equal to the yield strength, depends on heat propagation into the base metal and restraint conditions. It is interesting to find out by what maximal value can the dimensions of the active zone be reduced, irrespective of the cooling method. For low-carbon steels in bead deposition on the edge, the width of the active zone is determined by the width of the isotherm, corresponding to 300 °C, and for the bead-on-plate deposition — to 200 °C.

When welding with cooling is used, the active zone width is reduced. Let us consider the limit cases, when the active zone width is maximal (welding without cooling) and minimal (heat removal completely blocks heat propagation into the base metal, and the active zone exists only in the weld). Other cases are intermediate.

CO_2 consumable-arc welding can be selected as the main welding process to produce welded joints of low-carbon and low-alloy steel sheets. For comparison, let us analyse limit sizes of the active zone of welded joints on St.3 steel 3 mm thick (in this case the largest range of typical welded joints can be analysed).

Let us determine the maximal half-width of the isotherm, corresponding to 300 and 200 °C, for the case of complete penetration of the studied joints, applying a mathematical model for determination of the temperature field [8]. Then, let us calculate the cross-sectional area of the weld, using its average geometrical dimensions for each type of welded joint (Table 1), as the initial data. Welded joints of types B7, B12, F5, F10, T3, T7, O2 have two welds. For joints of types T3 and O2, let us consider the combined influence of these two welds, as the influence of one

Table 2. Maximal and minimal cross-sectional area of the active zone for different types of joints

Joint type	F_{max}, *mm²*	F_{min}, *mm²*	$K_{max\ red}$, %	*Joint type*	F_{max}, *mm²*	F_{min}, *mm²*	$K_{max\ red}$, %
Butt joints				*Fillet joints*			
B1	51.1	13.3	74	F1	48.9	8.3	83
B2	53.1	11.4	79	F2	40.8	14.0	66
B4	57.7	20.5	64	F4	53.5	12.1	77
B5	51.5	13.6	74	F5	52.4	10.0	81
B7	64.3	18.0	72	F6	51.8	8.8	83
B8	51.6	8.3	84	F9	51.7	8.6	83
B9	53.5	12.2	77	F10	53.6	12.4	77
B10	49.2	8.8	82	*Tee joints*			
B12	53.8	12.8	76	T1	62.7	7.8	88
B19	49.6	9.6	80	T3	76.7	15.6	80
B28	46.7	15.0	68	T6	62.4	7.5	88
Overlap joints				T7	66.4	11.5	83
O1	62.7	7.8	88				
O2	76.7	15.6	80				

weld with the coefficient of 1.15, and for B7 let us perform the calculation for one weld [9]. For welds with a back bead, the main weld area is larger, than that of the back weld, by approximately 2 times. Heat input for the main weld (the second one applied), is also much higher, than the heat input for the back weld. Therefore, the active zone of the main weld [9], will prevail, so we will use it to perform calculations for joints of B12, F5, F10 and T7 type.

For the majority of butt and fillet joints, made by deposition on the edges, we derive the maximal and minimal areas of the active zone cross-section $F_{max} = (L_{is} - b_w)\delta + F_w$, $F_{min} = F_w$, where L_{is} is the maximal width of the isotherm, corresponding to 300 °C, mm; b_w is the weld width, mm; δ is the welded metal thickness, mm; F_w is the weld area, mm. For tee and overlap joints of the lower sheet, bead-on-plate deposition is used, and for the upper sheet – deposition on the edge. Heating source power when joining the edges of equal thickness is uniformly distributed: 1/3 of its power is applied to the vertical sheet (upper sheet for the overlap joint) and 2/3 – to the lower sheet. At the temperature of 200 °C, the maximal half-width of the isotherm is 15.3 mm, and at 300 °C it is 12.5 mm.

For joints of types B5, B10, B19 and B28, made on a backing or having a complex geometry, calculation of the cross-sectional area of a zone, heated above 300 °C, is more complicated, as the heat is applied to the backing or in a non-uniform fashion to one of the edges. The maximal half-width of the isotherm depends on the joint type.

Maximal degree of reduction of the active zone cross-sectional area was determined by coefficient $K_{max\ red} = 100 - 100F_{min}/F_{max}$, %. The results of the performed calculations are given in Table 2.

The conducted experiments confirmed the fact, that in welding with cooling, the dimensions of the active zone can be reduced by 70 % and more. Thus, it can be stated, that $K_{max\ red}$ values will be different for different types of welded joints. Shrinkage force and residual stress level are directly proportional to the dimensions of the active zone cross-sectional area.

Direct dependence of residual deformations, dependent on residual stresses, on the active zone dimensions, is preserved only at the values of compressive stresses that are smaller, than a certain critical value at which the stability is lost, and depend on weldment geometry [5]. In the case of the loss of stability deformations are increased many times.

CONCLUSIONS

1. Cross-sectional area of the active zone for standard welds, made in the optimal modes, can vary between the maximal and minimal value.

2. The extent of reduction of the active zone cross-sectional area, depends on the type of the welded joint: it is maximal (88 %) for joints of types T1, T6, O1 and minimal (64 %) for butt joint B4.

3. Lowering of residual deformations at compressive residual stresses below the critical values, is directly proportional to reduction of the active zone cross-sectional area in welding.

REFERENCES

1. Lobanov, L.M. (1983) *Technological procedures for reducing strains and stresses* Kyiv: Znanie.
2. Lobanov, L.M., Pavlovsky, V.I., Loginov, V.P. *et al.* (1990) Regulation of thermodeformational cycles in welding sheet structures, using heat absorbers. *Avtomaticheskaya Svarka*, **9**, 30 – 42.
3. Wells, M.E., Lulens, W.E. (1986) Effect of forced gas cooling on GTA weld pools. *Welding J.*, **12**, 314 – 321.
4. Gedrovich, A.I. (1998) *Plastic deformation in welding*. Lugansk: EUSU.
5. Gedrovich, A.I., Zhidkov, A.B. (2000) *Features of sheet structure deformation in welding with cooling*. Lugansk: EUSU.
6. Kasatkin, B.S., Prokhorenko, V.M., Chertov, I.M. (1987) *Welding stresses and strains*. Kyiv: Vyshcha Shkola.
7. Gedrovich, A.I., Zhidkov, A.B. (2000) Influence of different methods of heat removal on the active zone in welding. *The Paton Welding Journal*, **3**, 37 – 40.
8. Zhidkov, A.B. (1999) Mathematical simulation of the temperature field in welding with forced cooling. *Visnyk SUDU*, **1**, 69 – 75.
9. Nikolaev, G.A., Prokhorov, N.N. (1978) *Stresses in welding*. Moscow-Leningrad: AN SSSR.

BARRELS OF UNITS FOR DETONATION SPRAYING OF COATINGS

Yu.A. KHARLAMOV
East-Ukrainian National University, Lugansk, Ukraine

ABSTRACT

The paper deals with the advantages of technological application of detonation modes of gas mixture combustion, chiefly for thermal spraying of coatings, as well as various design features of combustion chambers of the coating units. Feasibility of developing the processes of spraying of coatings, using cylindrical detonation waves, and also using continuous gas detonation, is noted.

Key words: *thermal spraying, detonation in gases, detonation-gas spraying, barrels, detonation guns*

Detonation spraying of coatings (DSC) was first patented in the USA (1952), and later independently developed in the USSR [1 – 5]. The high quality of the coatings produced by the above process, ensured its successful application and development for more than 40 years. DSC is one of the most effective thermal spraying (TS) processes [6, 7]. DSC development allowed for the first time achieving a higher velocity of the sprayed particles. High-speed plasmatrons, as well as devices, using the mode of continuous high-speed gas combustion (rocket combustion chambers) were introduced much later [8]. Units for high-speed flame spraying (HSFS) consume up to 10 m^3 of gases for deposition of 1 kg of a tungsten-carbide based coating. Gas consumption in such units can be up to 30 – 150 m^3/h. This method has lately become widely accepted in the developed countries. However, this system requires a higher consumption of gases to achieve equivalent pressure, comparable with the detonation process. The main disadvantages of HSFS (high specific flow rate of gases, overheating of the base–coating system, need for intensive cooling) are associated with this feature. Modern detonation guns (DG) for coating application, for instance, Super D-Gun [1, 2, 9], provide acceleration of the powder particles movement up to 1000 m/s with simultaneous heating up to the melting temperature. Moreover, they consume a much smaller amount of the combustible mixture at the same efficiency, as that of HSFS.

Detonation modes of gas combustion have a number of useful features (in terms of practical application). This primarily is achievement of higher temperatures, compared to usual combustion (up to 4000 °C and more at normal pressure). An important thermodynamic feature of detonation is the fact that at the same heat evolution the increase of entropy is smaller, and, as a result, the greater part of chemical energy of the fuel can be used for mechanical work. This allows application of spraying modes with more intensive acceleration of the sprayed particle movement. In order to carry out combustion, it is necessary to spend a negligible amount of energy, just to initiate the process, as it proceeds entirely at the expense of the inherent energy capabilities of the system. In the case of plasma processes, the power consumption to achieve high temperatures, is extremely high. Detonation units, similar to other combustion units, are reliable and have a long operational life. These features of detonation-gas processes allow them to compete with electric-plasma processes. Energy concentration in ten times compressed oxygen-hydrocarbon mixtures reaches 1.10^8 J/m^3, this being two orders of magnitude higher, than in the oxyacethylene flame.

Despite a quite long history of development, DSC still remains to be the least studied of the modern TS processes. This primarily concerns detonation-gas equipment for spraying of coatings. There are practically no publications, devoted to designing DG components and assemblies, calculation and selection of its main characteristics and parameters. Considering the broad range of physico-chemical properties of the deposited materials, appropriate hardware is required for flexible control of the parameters of pulsed heterogeneous flow, in order to form coatings with the required characteristics. The structure and main requirements to DG assemblies were considered in [10, 11].

This paper outlines the main ways to implement the above requirements for the major assembly of any DG – the barrel of detonation combustion chamber. The processes proceeding in the barrel primarily determine the parameters of the heterogeneous flow, that forms the sprayed coating. In the most general case, self-sustaining detonation in gases can be achieved, using plane, cylindrical and spherical waves [12]. The latter two can be both diverging and converging.

Traditionally, modern DG mostly incorporate cylindrically-shaped barrels, in which the detonation phenomenon with plane detonation waves takes place. Adjustment of the sprayed particle flow parameters is performed by varying the barrel dimensions (diameter, length), combustible mixture composition, degree of the barrel filling with the combustible mixture and location of the initial dose of powder in the barrel. However, other barrel geometries can be also

used, allowing control of the parameters of the pulsed heterogeneous flow, forming the coating. As the main indices of barrel classification, let us consider the shape of the transverse and longitudinal sections, geometry of inner surfaces, cooling system, etc.

Cross-sectional shape. In principle, barrels of a square, rectangular, oval and other cross-sectional shapes can be applied, if it is justified by a more rational use of the sprayed powder, when processing small parts or local areas of the surfaces being treated. Application of longitudinal partitions allows creating barrels with greater cross-sectional dimensions. The formed longitudinal cells stabilize the initiation and propagation of detonation, yet increase the energy losses. To coat circular surfaces of a relative small size, the barrel can be made to have a circular cross-section. Use of this principle allows coating also other kinds of narrow, perimetrally located surface sections.

Change of the cross-section along the barrel length. Distinction is made between barrels with the cross-section constant along the length, cross-sectional area or shape changing (smoothly or abruptly) along its length, as well as those with the cross-sectional shape and area changing simultaneously. One of such designs is a stepped barrel (Figure 1, *a*) with the cross-section decreasing in the direction of the detonation product outflow [13]. The specific energy of detonation product flow is increased at the expense of initiation of the reflected waves at transition from one step to another. In order to create better conditions for the detonation product flow with suspended powder particles, it is recommended to use barrels with a smoothly decreasing cross-section, including conical cross-section (Figure 1, *b*). Such barrels allow producing overcompressed detonation waves and an enhanced energy impact on the sprayed powder particles [14]. The outlet section of the barrel can be made to have a constant cross-section, as well as a cross-section, shaped as a nozzle (Figure 1, *c, d*), ensuring additional capability of controlling the velocity, heat and chemical relaxation of the powder particles. As shown in [15], use of an expanding nozzle can provide up to 40 % acceleration of the particles. Application of narrowing nozzles reduces their velocity. At a high gradient of the step diameters, the barrel can have a bow shape [4]. Such barrels are especially advantageous, when using combustible gases — acetylene substitutes. However, it is more difficult to ensure detonation initiation and localizing of the initial powder cloud in the specified zone.

This problem is partially solved in the barrel design, shown in Figure 1, *e*. Here, initial section *1*, going over smoothly or abruptly into expanded section *2*, is made to have a small cross-sectional area. The nozzle for powder feeding *3* and igniter *4* are mounted in the inlet section at the blind end face. This facilitates detonation initiation in the expanded outlet part of the barrel, and also promotes compacting the powder cloud at the beginning of the expanded outlet

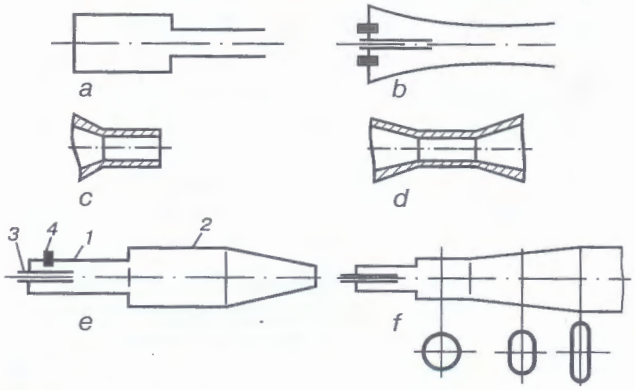

Figure 1. Barrels with the cross-section, variable along its length (for designations here and in Figures 2, 3 see the text)

section. Barrel designs with the cross-section, smoothly expanding towards the direction of the detonation product outflow, can be used. The schematic of the barrel with the cross-sectional shape, changing along its length, is shown in Figure 1, *f*. Transition from axially symmetrical section to a section symmetrical, relative to one of the axial planes, provides not only formation of the coating layer of an appropriate shape, but also additional turbulisation of the gaseous suspension flow, as well as its better mixing with the combustion products, and a certain extension of the time of the powder being in contact with the combustion product flow and improved energy exchange between them.

Barrels with an adjustable open flow area are used to control the movement velocity and temperature of powder particles. A design is developed, in which the barrel outlet section incorporates regulation elements, mobile in the lateral direction. However, lateral powder feed through the regulation elements, hinders its uniform spraying over the cross-section. More suitable is a stepped barrel with a conical transition between the steps. A nozzle for feeding power and a conical head are mounted from the side of the blind end face, coaxially with the barrel. Axial displacement of the nozzle is used to adjust the open flow area between the conical head and the barrel section. Varying the barrel cross-sectional area along its length, provides a uniform filling of the barrels, operated with cylindrical detonation, with the combustible mixture and powder, as well as formation of a cylindrical detonation front.

Some possible variants of barrel designs to process parts of the type of shafts with cylindrical waves, are shown in Figure 2, *a* – *c*. Individual barrel sections can be conical or of some other shape. Therefore, detonation can develop and propagate as unidimensional, with subsequent transition (conversion) into cylindrical (Figure 2, *c*). Figure 2, *d* shows a schematic of a barrel for spraying of coatings. Inlet part *1* is made as a cylindrical tube, changing into outlet section *2* in the form of a round hollow disc. Nozzle *3* for powder feeding with sprayer *4* is introduced into the barrel through the blind end face. Barrels for spraying with cylindrical detonation waves, can be made with the axial section height, variable in the

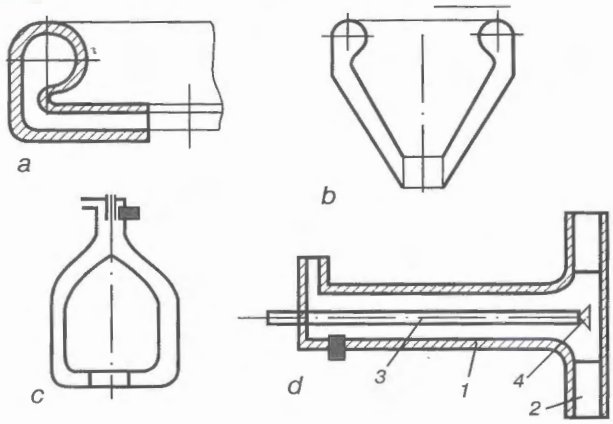

Figure 2. Barrels for spraying of coatings with cylindrical detonation waves

radial direction. Barrel separation into individual sections can be applied also in the case of spraying with cylindrical detonation waves. This greatly simplifies the powder cloud localization and provides the detonation mode of the combustible mixture burning.

Geometry of barrel inner surfaces. Barrel inner surfaces can be smooth or rough. In a rough tube, the detonation rate looses the property of the mixture physico-chemical constant and depends on the hardware condition (degree of roughness — the higher it is, the greater is the velocity decrease) [16]. This phenomenon can be used to adjust the dynamic and thermal interaction of the powder particles with detonation products. Intensive turbulence, caused by roughness, can promote not only intensification of heat exchange, but also more uniform mixing of the powder with the combustion products. Instead of the regular wire spirals, it is better to use in the barrel walls threaded grooves of various profile, made along the entire length of the barrel, or in its individual sections. The grooves can be circular or helical. When the grooves are located in the barrel inlet section, the pre-detonation distance is shortened, whereas their location at its outlet improves powder mixing and intensifies heat exchange.

Shape of the barrel longitudinal section. By the shape of the longitudinal section the barrels are distinguished into straight, bent, branching, straight

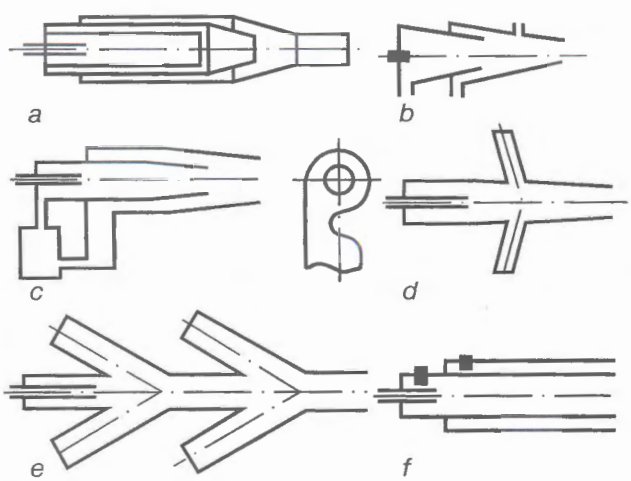

Figure 3. Multi-section barrels for spraying of coatings

with both end faces open, loop- and U-shaped, multichamber with the common ignition chamber, circular, spiral [3] and multi-section.

Analysis of the schematics of some of these designs, is given in [14]. Various shields can be incorporated into the barrel. Varying their shape, allows controlling the shape and dimensions of the initial powder cloud in the barrel, conditions of gas exchange, when the barrel is filled with fresh combustible mixture, as well as conditions of formation and outflow of the pulsed two-phase jet. Thus, during exhaust of the pulsed two-phase jet, its shielding from the environment by a circular flow of the detonation products is provided, as well as a more uniform particle temperature and higher velocity of their movement over the flow cross-section.

Multi-section barrels can be used to produce overcompressed detonation waves and extend the time of the powder contact with the detonation products, in order to provide the appropriate energy exchange and degree of the required transformations in the initial material. The diagram of one of the designs of multisectioned barrels is shown in Figure 3, *a*. The barrel is made of three co-centric sections, with the outlet of the enclosing section being shifted in the direction of the movement of the detonation product flow, with respect to the outlet of the enclosed section. Enclosing sections are, as a rule, made with the cross-section, becoming smaller in the direction of the detonation product outflow. Powder is fed into the central (starting) section, in which combustion and detonation of the combustible mixture are initiated. When combustion reaches the section edge, two combustion (or detonation) fronts are formed in the enclosing section, one of them continuing its movement towards the open end face of the barrel, and the second moving through the circular part of the section in the reverse direction. Similar phenomena are also observed in combustion transition to the next section.

Use of such barrel designs with two or more sections, ensures the time of the powder contact with the detonation products, required for the necessary transformations to proceed, and also provides overcompressed detonation waves, at the expense of the main flow enhancement by the detonation products, flowing out of the enclosing sections. In order to adjust the degree of transformations in the sprayed powders, the barrel sections can be filled with different kinds of combustible mixtures, and the powder can be fed directly into the outlet section. One of such variants is shown in Figure 3, *b*. To ensure the turbulence of the two-phase flow, in order to intensify energy exchange between the powder and the detonation products, it is possible to apply tangential joining of the sections (Figure 3, *c*). In order to produce overcompressed detonation waves, it is possible to use additional sections in the form of channels, connected to the side walls of the main barrel (Figure 3, *e*), as well as additional circular sections, enclosing the barrel, in which the powder material is processed (Fi-

gure 3, *f*). Additional sections promote generation of overcompressed detonation waves, extension of the time of the combustion products outflow from the barrel and appropriate intensification of the processes of their interaction with the powder particles. In the barrel with two co-centric combustion chambers (see Figure 3, *f*) a pulsed two-phase jet is formed, that is divided into the central jet, carrying suspended particles of the powder, and a circular jet of combustion products, that encloses it.

Gas-dynamics of gas mixture combustion in barrels, fitted with different compartments and partitions, has not been studied, either theoretically, or experimentally. On the other hand, availability of an adjacent, not gassy chamber, communicating with the main chamber through a pass hole, has a decisive influence on the nature of gas-air mixture combustion in both the chambers: it becomes highly turbulent. Pressure gradient is achieved between the chambers, that leads to alternate flowing of the mixture from one chamber into another. The pressure in the chambers is 4 – 15 times higher, than in the absence of an adjacent chamber and the main chamber connection to the atmosphere through a hole of the summary area. The nature of the process of pressure variation in the chambers, is dependent on the ratio of the hole areas, their location and ignition, as well as fuel concentration [17]. All this is indicative of the need to widen the experimental investigations on optimizing the processes of heating and increasing the powder movement velocities by selection of the barrel geometrical dimensions.

Barrel cooling. Stabilisation of the barrel wall temperature has an important role in provision of reliable operation of DG. Water cooling is usually used and the barrel is enclosed completely to provide a forced flow of the coolant. Design of water-cooled barrels is described in sufficient detail in [3, 4]. Promising is the application of evaporation cooling systems, not requiring the use of forced water circulation and allowing its consumption to the reduced. With air cooling, special cooling fins are made on the barrel outer surfaces. Forced air flows can be used to cool the barrel walls. Thus, the functions of contamination removal and barrel cooling are combined. Combined barrel cooling (air and water) can be also used. Self-sufficient water cooling systems are being developed for normal functioning of DG.

An important task is utilization of heat removed through the barrel walls. One of the methods of such recovery consists in using it for preheating the combustible mixture before its feeding into the barrel, as well as regasification of liquefied gases. However, application of heat pipes, allowing the most precise maintenance of the required thermal mode of the barrel walls and utilization of heat (for preheating the gases – the detonating mixture components, sprayed powder, etc.) should be regarded as the most promising.

It is also possible to use porous cooling, when the barrel is made to have gas-permeable walls and is completely enclosed by the cooling cavity, connected to the cooling gas feeding system. Under the impact of the pressure gradient, the cooling gas (nitrogen, CO_2, etc.) comes from the cooling cavity to the barrel inner surface and creates a near-wall zone of lower temperature. The porous wall temperature turns out to be lower, than the temperature of an impermeable wall, operating under similar conditions, for two reasons: the heat flow from the working body to the wall is reduced due to lowering of gas temperature in the near-wall zone (outer thermal protection); part of the heat, coming to the porous wall, is absorbed by the cooling gas during its movement through the wall pores (inner thermal protection). In addition, during the barrel filling with fresh combustible mixture and the powder, the cooling gas, evolving through the porous walls into the barrel cavity, prevents the powder particles deposition.

Spatial position of the barrel. DG with the horizontal, vertical and inclined position of the barrel are distinguished. When complex-shaped (not-rectilinear) barrels are used, the spatial feature should refer to the outlet section, that is used directly for heating and acceleration of the powder movement by the combustion product flow and should be rectilinear. The barrel position in space influences DG configuration and the processes of its filling with the fresh combustible mixture, especially powder. In the case of a vertical position, the conditions of gas exchange during the barrel filling are improved, gravitation-induced deposition of powder on the vertical walls is eliminated, although it can be used during the barrel filling. DG are made to have an adjustable barrel inclination capability for a more convenient setting up of the DG–part system. Change of the barrel position in space is also used for transition from the modes of DG adjustment and reaching a stabilized condition, to the operating (steady-state) mode.

Increase of shooting rate. Work is being currently performed to develop DG with an improved shooting rate. Gas-dynamic control systems are used for this purpose [9]. A process of spraying of coatings by high-frequency pulsed detonation has been developed, that is performed by a unit, incorporating no mechanically moving parts and using special aerodynamic valves for backfire protection [18]. This essentially simplifies the system design and enables DG operation in the broadest range of frequencies (shooting rates) of up to 100 Hz and higher, without applying any cyclically operating valves. It should be noted that development of such pulsed equipment has been going on since the start of XX century. When such equipment is being developed and used, however, its real efficiency should be taken into account, as well as the change of the thermophysical and time conditions of the sprayed coating formation. Development of such equipment is rational for spraying very large parts and large enough production output.

The tendency of improving DG efficiency through increasing their shooting rate, can be represented as

trying to provide a continuous process of the combustible mixture burning in the detonation mode. The so-called standing detonation waves [19], implemented as a jet variant, can be of a certain interest for TS and other technologies. This paper demonstrates such a possibility and reveals the main physical regularities of continuous gas detonation in circular barrels. A continuous process is understood to be such a process, that is not interrupted, as long as the initial parameters of the combustible mixture, condition of the walls and of the detonation products outflow are maintained within certain limits in the barrel. In a circular barrel, continuous detonation combustion is achieved through multiple running of one or several detonation waves along a closed path, in which the reaction products behind the next wave, are driven back and replaced by fresh mixture, capable of detonation combustion in the same wave during the next turn or in the next wave (if there are several of them). The direction of wave propagation is lateral with respect to the general direction of the reagent flow through the barrel [20].

CONCLUSIONS

1. Further improvement of the processes and equipment for detonation spraying of coatings, requires optimizing barrel designs, based on a more profound study of the pulsed processes of combustible mixture burning and formation of pulsed heterogeneous flows.

2. Change of barrel geometry in the units for spraying of coatings, allows controlling the modes of burning-out of the combustible mixture of gases, formation and parameters of pulsed heterogeneous flow with the sprayed powder particles suspended in it, and, thus formation of the structure and properties of detonation coatings.

3. To achieve a more effective use of pulsed combustion energy and control the processes of structure formation and properties of detonation coatings, it is necessary to study the laws and modes of pulsed combustion of gas mixtures in non-cylindrical barrels and two-dimensional movement of the combustion products with suspended powder particles through them.

4. It appears rational to conduct fundamental and applied work to develop detonation guns, using the principles of continuous and cylindrical gas detonation.

REFERENCES

1. (1990) D-Gun for spraying wear resistant coats. *Finishing*, **5**, 24.
2. (1990) Un nouveau canon a detonation: Le super D-GUN d'Union Carbide. *Industrie*, **4**, 34 – 38.
3. Shorshorov, M.Kh., Kharlamov, Yu.A. (1978) *Physico-chemical principles of detonation spraying of coatings*. Moscow: Nauka.
4. Zverev, A.I., Sharivker, S.Yu., Astakhov, E.A. (1979) *Detonation spraying of coatings*. Leningrad: Sudostroyeniye.
5. Bartenev, S.S., Fedko, Yu.P., Grigorov, A.I. (1982) *Detonation coatings in machine-building*. Leningrad: Mashinostroyeniye.
6. Movshovich, I.Ya., Dolmatov, A.I., Podolsky, B.A. (1999) Technology and equipment for detonation spraying of coatings with preset properties. *Suchasne Mashinobuduvannya*, **1**, 111 – 115.
7. Garanin, V.M., Ivanenko, A.A., Klimenko, S.A. (1999) Detonation spraying of coatings — new possibilities in restoration of parts. *Ibid.*, **2**, 96 – 99.
8. (1991) High-velocity spray gun produces touch-hard metal coatings. *Adv. Mater.*, **18**, 54 – 68.
9. Tyurin, Yu.N. (1999) Improvement of equipment and technologies for detonation spraying of coatings. *Avtomaticheskaya Svarka*, **5**, 13 – 18.
10. Kharlamov, Yu.A. (1986) Schematic designs of detonation guns for treatment of powder materials. *Poroshkovaya Metallurgia*, **12**, 89 – 95.
11. Kharlamov, Yu.A. (1986) Technology requirements to automation of detonation spraying process. *Avtomaticheskaya Svarka*, **1**, 62 – 67.
12. Vasiliev, A.A., Mitrofanov, V.V., Topchiyan, M.E. (1987) Detonation waves in gases. *Fizika Goreniya i Vzryva*, **5**, 109 – 131.
13. Samsonov, G.V., Dvukraev, B.N., Sharivker, S.Yu. *et al. Unit for detonation spraying*. USSR author's certificate **513728**, Int. Cl. B 05 B 7/20; C 23 C 7/00. Publ. 05.07.76.
14. Kharlamov, Yu.A., Shorshorov, M.Kh., Pisklov, Yu.I. *et al.* (1980) *Detonation guns for spraying of coatings*. Moscow: IMET AN SSSR.
15. Grigoriev, V.V. (1996) Use of the nozzle in acceleration of particles by flows of detonanion products in tubes. *Fizika Goreniya i Vzryva*, **5**, 21 – 29.
16. Rybanin, S.S. (1969) On the theory of detonation in tubes with a rough inner surface. *Ibid.*, **3**, 395 – 403.
17. Strelchuk, N.A., Mishuev, A.V., Nikitin, A.G. *et al.* (1984) Gas dynamics of combustion of gas-air mixture in a semi-closed volume at the pressure release into a non-gassy communicating volume. *Ibid.*, **1**, 65 – 69.
18. Fagoaga, I., Barykin, G., de Juan, J. *et al.* (1999) High-frequency pulse detonation (HFPD) spray process. In: *Proc. of UTSC*, Dusseldorf.
19. Bartlme, F. (1981) *Gas dynamics of combustion*. Moscow: Energoizdat.
20. Bykovsky, F.A., Mitrofanov, V.V., Vedernikov, E.F. (1997) Continuous detonation combustion of air-fuel mixtures. *Fizika Goreniya i Vzryva*, **3**, 120 – 131.

CALCULATION OF PLASMATRONS WITH A HIGH-CURRENT CATHODE FOR HEATING DISPERSED PARTICLES

V.L. DZYUBA and **K.A. KORSUNOV**
East-Ukrainian National University, Lugansk, Ukraine

ABSTRACT

Engineering method for calculation of electric, thermal and service characteristics of electric-arc plasmatrons with a high-performance high-current cathode for heating of dispersed particles is presented.

Key words: *calculation method, plasmatron, similarity criteria, characteristic, high-current cathode, dispersed particles*

Commercial plasmatrons for spraying are characterized by substantial drawbacks, such as insufficient length of the zone of interaction of the plasma jet with particles heated, low efficiency and productivity of spraying and a short service life of the cathode. In view of the demand of metallurgical and chemical industries for high-power plasmatrons for deposition of protective coatings, we developed a plasmatron with a high-performance cathode (Figure 1). The plasmatron passed industrial tests by depositing protective coatings on refractory surfaces of steel casting ladles with a capacity of 300 t. It consists of a high-current cathode unit, main anode *4* and reaction chamber *5*.

Specifications of the plasmatron

Power, kW	560
Arc current, A	800
Working gas (air) flow rate, kg/s	0.061
Auxiliary gas (argon) flow rate, kg/s	$(2.0 - 2.4)\cdot10^{-5}$
Thermal efficiency	0.75 – 0.80
Productivity of heating and spraying of powders (zirconia, tungsten, molybdenum, grog-type, magnesite, etc.), kg/h	120 – 150
Service life, h	300 – 500
Erosion of cathode, kg/C	$1\cdot10^{-9} - 1\cdot10^{-10}$

Principle of operation of the high-current cathode is similar to that of the plasma cathode. It is an independent plasmatron which consists of additional anode *1*, inter-electrode inserts *2* and cylindrical copper cathode *3*. Argon is fed through vortex rings *6* of the high-current cathode, and the working gas (air) is fed to the gap between the cathode unit and main anode *4*. The main air arc is fixed to the pilot argon arc during operation of the plasmatron. Thus, the positive arc column has two characteristic regions in the discharge channel of the plasmatron with a high-current cathode (Figure 2): laminar (in the high-current cathode at a current of up to 250 A) and turbulent (in the main anode channel at a current of above 250 A). Therefore, calculation of the electric arc in the channel of such a plasmatron is reduced to calculation of its laminar and turbulent regions.

Extremely differing and complicated phenomena occur in the discharge channel of the plasmatron. However, no comprehensive data on them are available so far. Therefore, the main role in investigation of the arc and evaluation of characteristics of the plasmatrons is given to experimental studies involving the similarity and dimensional theory methods.

Dimensionless complexes, i.e. criteria, which can be used to generalize experimental results and derive empirical formulae, convenient for calculations, were developed in [1, 2] on the basis of parameters determining the arc burning process. For example, characteristics of the arc discharge in a plasmatron are described by dimensionless values Π, which are functions of the similarity criteria:

$$\Pi = f\left(\frac{Ge}{Im}, \text{Re}, \text{Kn}, K_1', K_2', K_3', K, K_n'\right), \quad (1)$$

where G is the gas flow rate; e — is the elementary electric charge; I — is the current; m is the mass of a particle; Re and Kn are the Reinolds and Knudsen numbers, respectively; K_1', K_2', K_3', K and K_n' are the geometrical similarity criteria.

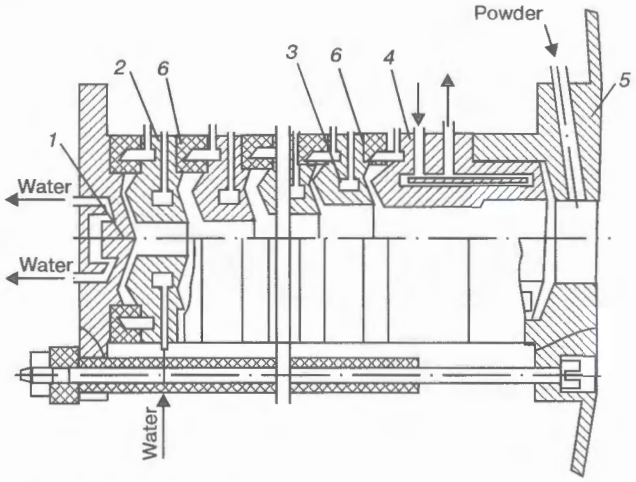

Figure 1. Plasmatron for heating dispersed particles (see designations in the text)

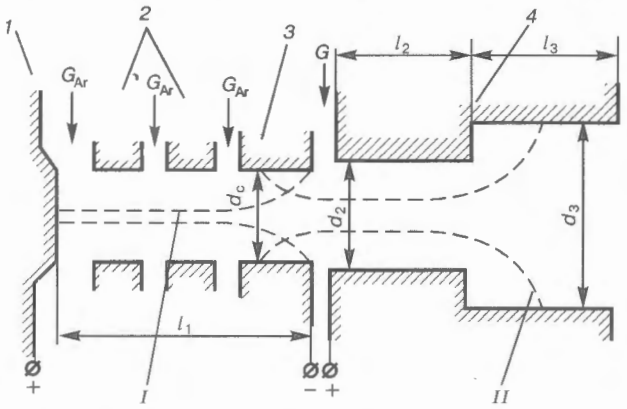

Figure 2. Schematic of the plasmatron with a high-current cathode: *I* and *II* — laminar and turbulent regions of the arc; *1* — additional anode; *2* — inter-electrode sections; *3* — cathode; *4* — main anode (see the rest of the designations in the text)

Here the values of Π can be local or integral dimensionless characteristics of the arc. If the arc in plasmatrons burns in gas of the same chemical composition, and its temperature at the entrance to the discharge channel is constant, equation (1) can be simplified by omitting dimensional constants and written down as follows [1]:

$$\Pi = A\left(\frac{I}{G}\right)^{\alpha}\left(\frac{G}{d}\right)^{\beta}(pd)^{\gamma}, \qquad (2)$$

where d is the diameter of the discharge channel; p is the pressure of the plasma jet at the plasmatron exit section; A, α, β and γ are the constant dimensional values determined in processing of the investigation results.

Turbulent region. Arc voltage in the plasmatrons with a step-type anode can be approximated by the following equation within the following ranges of variations of parameters: $I/d_2 = (0.5 - 4.0)\cdot10^4$ A/m; $l_2/d_2 = 5.25 - 14.50$; $l_3/d_3 = 2.6 - 4.4$; $G/d_2 = 0.45 - 6.50$ kg/(s·m); $p(d_2 + d_3) = (5.8 - 18.3)\cdot10^3$ Pa·m [2]:

$$U_a = 4.55\left(1 + 4.6\cdot10^{-5}\frac{I}{d_2 + d_3}\right)\left(\frac{G}{d_2 + d_3}\right)^{0.22} \times \qquad (3)$$

$$\times\left(\frac{l_2}{d_2} + \frac{l_3}{d_3}\right)^{0.95}[p\,(d_2 + d_3)]^{0.23},$$

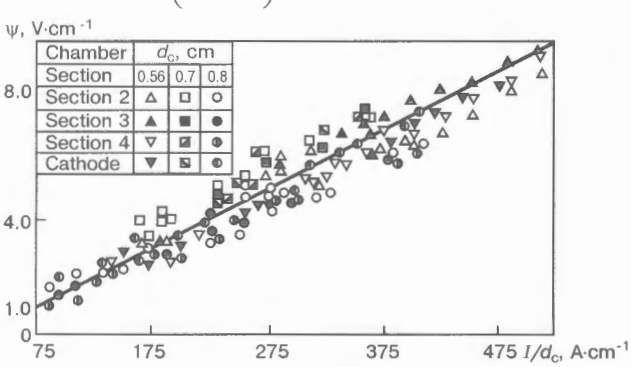

Figure 3. Generalized dependence of ψ upon I/d_c

where d_2, d_3 and l_2, l_3 are the diameters and lengths of the discharge channel before and after a shoulder, respectively.

The following formula was suggested in [2] for the arc of the high-power plasmatrons within the following ranges of parameters: $I = 300 - 1000$ A, $G = (24 - 15)\cdot10^{-3}$ kg/s and $d_2 = (2 - 4)\cdot10^{-2}$ m:

$$\frac{U_a d_2^{0.77}}{G^{0.78}} = 4.55\cdot10^{-2}\frac{I}{G}. \qquad (4)$$

Thermal efficiency (η) of such plasmatrons can be estimated from the following formula:

$$\frac{1-\eta}{\eta} = 5.85\cdot10^{-5}\left(\frac{I^2}{Gd_2}\right)^{0.27}\left(\frac{G}{d_2}\right)^{-0.27} \times \qquad (5)$$

$$\times\,(pd_2)^{0.3}\left(\frac{l_2}{d_2} + \frac{l_3}{d_3}\right)^{0.5}.$$

Laminar region. Potentials of the sections were experimentally determined to evaluate voltage of the arc of the high-current cathode. The generalized dependence of arc voltage and current U_s upon I, d_c and z is shown in Figure 3, where the $\psi = \frac{U_s}{z} - \frac{3}{d_c^{1.43}}$ value is plotted on the axis of ordinates and I/d_c is plotted on the axis of abscissas. As it can be seen from the Figure, experimental points of the plot are approximated by a straight line that rises with an increase in I/d_c. Experimental data within a range of $I = 100 - 575$ A, $d_c = (5.5 - 9.5)\cdot10^{-3}$ m and $z = (10 - 50)\cdot10^{-3}$ m are satisfactorily described with an error of 11 % by our formula

$$\frac{U_s}{z} - \frac{M_1}{d_c^{1.43}} = M_2\frac{I}{d_c}, \qquad (6)$$

where $M_1 = 3$ V·cm$^{0.43}$ and $M_2 = 0.019$ V·A^{-1}.

Potentials of the sections of the high-current cathode can be calculated from formula (6) over the above range of the d_c, I and z values. Voltage of the cathode region of the high-current cathode is determined as follows:

$$U_{h.c} = \int_{L'}^{l_1} E dz + (U_c + U_{a.a}), \qquad (7)$$

where l_1 is the length of the high-current cathode channel; L' is the length of the anode voltage drop region; E is the intensity of the electric field in the high-current cathode channel and U_c and $U_{a.a}$ are the cathode and additional anode potential drops, respectively.

To make use of (7), it is necessary to find dependence of E upon the d_c and z values. Analysis of the experimental data shows that the z dependence of E can be ignored. This is indicative of the fact that the

arc is rapidly developing in the high-current cathode channel, and its properties are determined mostly by ultimate characteristics. The following formula was derived to calculate intensity of the electric field, E, in the high-current cathode channel:

$$E = M_2 \frac{I}{d_c} + \frac{M_1}{d_c^{1.43}} \text{ [V/cm]}. \quad (8)$$

It is valid for the same ranges of the of d_c, I and z values as in (6).

Figure 4 shows the curves of losses of the energy through the additional anode $Q_{a.a}$, section Q_s and cathode Q_c of the high-current cathode unit for three values of d_c, plotted on the basis of dependence $Q = f(I/d_c)$. Experimental data are described by formulae (9) and (10) with an error of not more than 14 %. Heat losses through the cathode can be determined using a formula similar to that used for Q_s

$$Q_{a.a} = N_1 \left(\frac{I}{d_c^{1.95}} \right) \text{[W]}, \quad (9)$$

$$Q_c = Q_s = N_2 z^{0.15} \left(\frac{I}{d_c^{1.95}} \right) \text{[W]}, \quad (10)$$

where $N_1 = 1.09$ V·cm$^{1.95}$; $N_2 = 0.3$ V·A$^{-0.57}$·cm$^{1.42}$ and $z = 0.5 - 5.5$ cm.

Consider calculation of working parameters and geometry of the flow section of the plasmatron with a high-current cathode in accordance with the diagram shown in Figure 2. The mean mass enthalpy of gas at the exit section of the plasmatron is related to the values of U_a, η and T through the equation of conservation of energy

$$U_a I \eta = G(\bar{i}_b - \bar{i}_{bx}), \quad (11)$$

where $\bar{i}_b$ and $\bar{i}_{bx}$ are the enthalpies of gas at the exit and entrance sections of the plasmatrons, respectively, determined from tables of thermodynamic properties of materials.

The simplest calculation method is based on a unidimensional approximation. In this case the gas flow rate is determined as

$$G = \frac{\pi d_2^2}{4} \rho_b v_b, \quad (12)$$

where ρ_b is the plasma jet density and v_b is the velocity of the plasma jet flowing from the nozzle.

Pressure and density of the plasma jet are related to temperature through the equation of state

$$p_b = \rho_b \text{Re}_b. \quad (13)$$

Values of G, T_b and p_b depend upon the technological application of the plasmatron. Re is determined from the tables of thermodynamic functions by the preset value of T_b and p_b, and ρ_b is determined using (13). The optimal values of v_b depend upon the

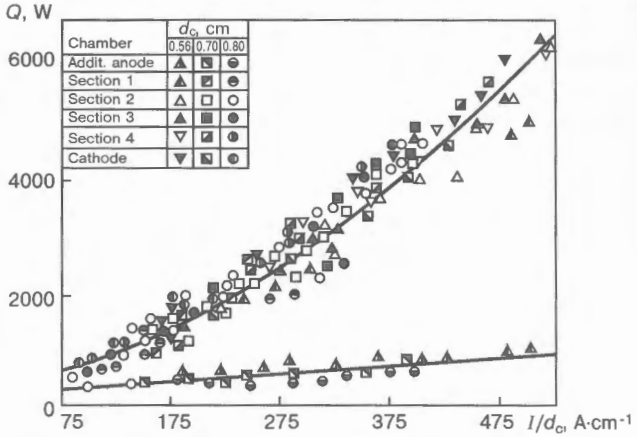

Figure 4. Generalized losses of heat through the high-current cathode

purpose of the plasmatrons. For commercial plasmatrons, the v_b values should be lower than the velocity of sound, v_s; otherwise a considerable part of the heat input to the gas would be spent for acceleration of the flow, and a high pressure gradient would be required at the entrance and exit sections of the plasmatron, which is highly undesirable. Based on these considerations, we can recommend that $v_b = (0.3 - 0.8)v_s$. If a plasmatron is simultaneously used as a reactor, in selection of values of v_b it is necessary to allow for an optimal time of dwelling of reagents within the reaction zone. Upon selecting the v_b values from (12), it is necessary to determine values of the diameter of the discharge channel, d_2, which range from 0.001 to 0.080 m for the most common plasmatrons. Low (about 0.001 m) values of d_2 are characteristic of low-power plasmatrons employed for microwelding, spraying, etc., whereas high (about 0.05 m) values are characteristic of the plasmatrons with a power of more than 500 kW. The following dependence [1] is recommended for calculation of d_2:

$$d_2 = K_2 d_{cr},$$

where $K_2 = 1.2 - 2.0$ and d_{cr} is the critical diameter of the discharge channel equal to

$$d_{cr} = 2[G/(\pi \rho_{cr} v_s)]^{0.5}.$$

In a case of operation in air within a pressure range of 0.1 – 0.5 MPa at a mean mass temperature of the plasma jet equal to 3000 – 4000 K, it is advisable that the length of the discharge channel, l_2, be equal to about $(5.5 - 14.5)d_2$.

The following relationship between the internal diameter and length of the electrode after the shoulder is indicated:

$$l_3 = (2.6 - 8.0)d_3, \quad (14)$$

where the ratio of the internal diameter of electrode after the shoulder to the diameter of the shoulder is

$$d_3 = (1.5 - 1.7)d_2. \quad (15)$$

The rest of the unknown values, i.e. I, U_a and η, are determined on the basis of technological requirements and the selected design of the plasmatron using equations (3) to (5).

We recommend that geometry of the high-current cathode be calculated using our experimental dependencies, allowing for formulae (6) to (10). The maximum diameter of the discharge channel of the high-current cathode to provide diffusion fixation of the arc is determined by the following relationship:

$$d_c \le c_2 d_2 G^{-0.05}, \qquad (16)$$

where $c_2 = 0.42$ kg$^{0.05}$·s$^{-0.05}$. As shown by the experimental results, variations in values of the cathode diameter along axis z within the limits of d_c have no effect on diffusion fixation of the arc to the cathode.

Length of the discharge channel of the high-current cathode, l_1, is determined by the quantity and sizes of its intermediate sections, length of the cathode channel and geometry of an additional anode, which depend upon the values of d_c:

$$l_1 = (2 - 10)d_c. \qquad (17)$$

Experimental studies of the high-current cathode within a range of variations of the current from 100 to 500 A show that flow rate of the auxiliary gas (argon) is not higher than 0.1 % of that of the main working gas and amounts to $(13 - 26)\cdot 10^{-6}$ kg/s.

Therefore, the method described above can be employed to calculate geometrical, electric and thermal characteristics of the plasmatron for heating dispersed particles over a wide range of variations in its parameters.

REFERENCES

1. Zhukov, M.F., Koroteev, A.S., Uryukov, V.A. (1975) *Applied dynamics of thermal plasma*. Novosibirsk: Nauka.
2. Dzyuba, V.L., Dautov, G.Yu., Abdullin, I.Sh. (1991) *Electric-arc and high-frequency plasmatrons in chemical-metallurgical processes*. Kyiv: Vyshcha Shkola.

POWDERS FOR THERMAL SPRAYING MADE FROM WASTES OF MILL ROLL PRODUCTION

Yu.A. KHARLAMOV, N.A. BUDAGIANTS, A.V. SHEVCHENKO and **S.A. YUDITSKY**
East-Ukrainian National University, Lugansk, Ukraine

ABSTRACT

The prospects of use of wastes after machining of mill rolls for commercial manufacture of inexpensive powders for thermal spraying are shown. Peculiarities of the effect of plasma spraying on adhesion strength of coatings have been investigated. It is shown that plasma coatings produced from mixtures of cast iron powders and self-fluxing nickel alloys possess high tribological properties.

Key words: *fine-dispersed wastes, mechanical mixtures of powders, plasma spraying, coatings, adhesion strength, chips, slime, cast iron powders*

One of the factors that limit application of thermal spraying (TS) under current conditions is a high cost of special materials, and powders in particular. Use of fine-dispersed wastes of various productions as TS powders is a promising way of raising the efficiency of the TS processes and extension of their application fields [1]. Reference [2] describes technologies for the manufacture of powders from chips of gray cast iron for air-plasma spraying. High tribological and strength properties of thermal spray coatings (TSC) of such materials are achieved by reinforcing the microcrystalline ε-phase, having an increased (10,000 MPa) hardness. Wear resistance and adhesion strength σ_{ad} of the coatings are not inferior (and in some cases are even superior) to those of the extensively used TSC based on eutectic nickel alloys.

Slimes are candidate raw materials for the manufacture of powders and powder compositions for TS [3, 4]. In this study the raw materials for the manufacture of cast iron powders and compositions on their base were products of rough grinding of cast iron two-layer mill rolls produced by centrifugal casting (LPKhNM-76, LPKhNM-73, LPKhNM-71, LPKh17NM-71) and chips of rolls (SPKhN-49, SShKhNMD-63, LPKhN-63, LPKh17NM-58).

Chips and slimes resulted from treatment of different structural grades of cast iron. Chips are formed after turning, using no lubricating-cooling fluid (LCF), of roll barrels with hardness of *HRC* 36 – 54, having the metal matrix with a pearlite and troostite-pearlite structure (Table 1) [5, 6]. Slimes are based on products of grinding of the bleached layer of high-alloy cast irons with hardness of *HRC* 55 – 64, having a dispersed martensite and troostite-martensite metal base (Table 1) [5, 6].

Microstructure of cast irons was investigated using the MIM-8 microscope on chips of the SPKhN-49, SShKhNMD-63, LPKhN-63 and LPKh17NM-58 types and specimens cut out from working surfaces of mill

Table 1. Chemical composition of cast iron mill rolls

Cast iron grade	Content of elements, wt.%										
	C	*Si*	*Mn*	*Cr*	*Ni*	*Mo*	*V*	*Cu*	*Ti*	*S*	*P*
LPKhN-71	2.9	0.5	0.6	1.0	3.10	—	—	—	—	0.08	0.20
LPKhNM-73	3.0	0.6	0.7	1.1	3.72	0.30	—	—	—	0.05	0.21
LPKhNM-76	3.0	0.6	0.7	1.4	4.20	0.34	—	—	—	0.05	0.12
LPKh17NM-71	2.8	0.6	1.1	16.2	2.10	0.40	0.20	0.8	0.50	0.03	0.07
SPKhN-49	3.0	0.7	0.6	0.7	1.20	—	—	—	—	0.08	0.29
SShKhNMD-63	3.1	1.3	0.6	0.8	3.00	0.30	—	0.4	—	—	—
LPKhN-63	2.8	0.5	0.6	0.8	2.80	—	—	—	—	0.07	0.40
LPKh17NM-58	2.9	0.5	1.0	15.4	1.70	0.52	0.22	—	0.45	0.04	0.07

rolls of the LGKhN-63 and LPKhNM-73 type. The sections were etched in 4 % HNO_3 solution of ethyl alcohol. Microhardness was measured using the PMT-3 microhardness meter. Individual structural components were identified on the basis of the available data [5, 6]. Characteristics of microstructure of the LPKhNM-76, LPKhNM-71 and LPKh17NM-71 rolls were taken from the results of studies [5, 6]. Morphology of particles was studied using the MBS-9 measurement microscope (×63). The objects of investigations were samples of powders (four samples of each particle size) about 1 g in weight.

Chips formed by turning the rolls using the VK2 alloy cutters without LCF had the form of plates from 36 × 15 × 2 to 38 × 16 × 2 mm in size with multiple spalls and cracks. No significant differences were noted between microstructure of the chips and that of treated cast iron. Microhardness of individual structural components and degree of dispersion of the reinforcing phases in a bleached layer of the LPKhN-63 roll and chips formed after its turning were almost identical. Investigation of sections of the SPKhN-49, SShKhNMD-63 and LPKh17NM-58 chips and comparison of the results obtained in [5, 6] showed no substantial differences in microstructure of the chips and rolls (Table 2). The content of the carbide phase in chrome-nickel cast irons was 25 – 35 vol.%, microhardness of alloyed carbides of iron was 9,000 – 11,000 MPa and that of chromium was 14,000 – 17,000 MPa [5, 6] (Table 2).

Chips were milled in a two-section ball mill (BM), comprising a 600 mm diameter drum, at a frequency of 28, 33 and 42 rpm (the ratio of rotation frequency n of the work chamber to critical frequency n_{cr} was 0.51, 0.60 and 0.76, respectively [7], the volume loading factor was about 0.3 and the ratio of the mass of balls (30 kg) to the mass of chips (6 kg) was 5:1). The chips were milled gradually: roughly — in BM with a diameter of 250 mm and finally — in disintegrator. To compare the efficiency of milling of materials of different structural grades, extra investigations were conducted to study technological feasibility of processing the chips of gray cast iron SCh-20 (plates 8.0 × 4.0 × 0.2 mm) formed after turning of casing parts into the powder for TS.

Analysis of the dependence of yield of powders with a particle size of 63 – 100 μm upon the time of milling of the chips (Figures 1 and 2) allows a pre-

Table 2. Structure of the working layer of mill rolls after heat treatment

*Cast iron grade**	*Metal base*	*Carbides and graphite*	*Cast iron hardness, HRC*
LPKhN-71	Troostite, acicular martensite (*HV* 7,500 – 8,200 MPa)	Eutectic (*HV* 10,000 – 10,900 MPa) and secondary (*HV* 9,000 – 9,800 MPa) carbides Fe_3C	55 – 60
LPKhNM-76	Acicular martensite (*HV* 8,400 – 8,900 MPa)	Eutectic (*HV* 10,500 – 11,400 MPa) and secondary (*HV* 9,500 – 10,000 MPa) carbides Fe_3C	55 – 63
LPKhNM-73 (section taken from the roll barrel)	Same	Same	56 – 63
LPKh17NM-71	Acicular martensite (*HV* 8,600 – 9,000 MPa)	Eutectic (*HV* 16,000 – 17,200 MPa) and secondary (*HV* 13,700 – 14,200 MPa) carbides Ch_7C_3 and Fe_3C (*HV* 10,000 MPa)	60 – 64
LPKh17NM-58 (section taken from chips)	Sorbite-type pearlite		52 – 54
SShKhNMD-63 (section taken from chips)	Troostite	Cementite (*HV* 9,100 – 9,800 MPa), globular graphite	47 – 51
SPKhN-49 (section taken from chips)	Lamellar pearlite	Cementite (*HV* 9,100 – 9,800 MPa), graphite	36 – 40
LPKhN-63 (section taken from chips)	Granular pearlite, troostite	Eutectic (*HV* 10,100 – 10,800 MPa) and secondary (*HV* 9,200 – 10,000 MPa) carbides of the cementite type	50 – 53

*Data are taken from [6, 7].

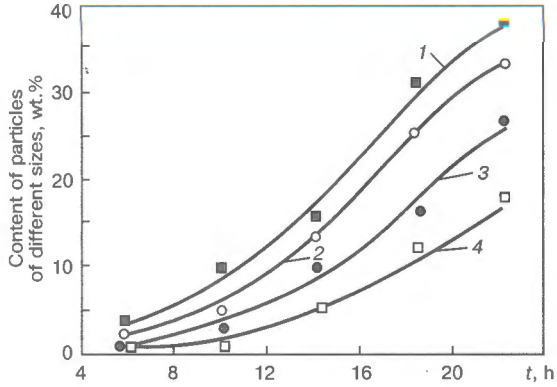

Figure 1. Dependence of yield Q of powder with a particle size of 63 – 100 μm upon time t of milling in BM of chips of gray cast iron SCh-20: *1* – *3* — diameter 600 mm at n/n_{cr} = 0.76, 0.60 and 0.51, respectively; *4* — diameter 250 mm at n/n_{cr} = 0.76

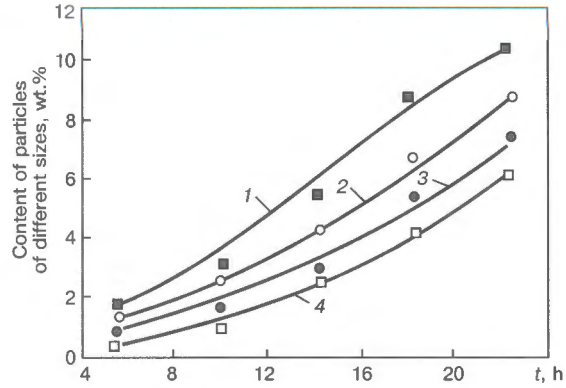

Figure 2. Dependence of yield Q of powder with a particle size of 63 – 100 μm upon time t of milling in BM of chips of rolls with a diameter of 600 mm at n/n_{cr} = 0.76: *1* — SPKhN-49; *2* — SShKhNMD-63; *3* — LPKhN-63; *4* — LPKh17NM-58

liminary proof of the efficiency of using BM for milling of materials of different structural grades. The gray cast iron chips are the easiest to mill. Productivity of the process depends upon the frequency of rotation of the mill drum and reaches a maximum value at n = 42 rpm and n/n_{cr} = 0.76 (see Figure 1). In milling materials with an increased hardness of the metal base, containing a considerable amount of the carbide phase, the productivity of milling decreases to a considerable extent. Dramatic decrease in the productivity of milling the chips of gray cast iron with a bleached working layer is caused by an increase in the energy of their fracture. Chrome-nickel cast irons LPKh17NM-58 and LPKhN-63 are characterized by the highest fracture energy under impact loading conditions. Milling of the chips of high-chromium cast iron LPKh17NM-58 (see Figure 2) yields the smallest amount of powder with particles 63 – 100 μm in size. This is indicative of the fact that energy parameters of milling of hard materials depend not only upon the structure of a metal base, but also upon the content, composition and morphology of carbides. The low yield of the TS powders of harder cast irons and dependence of the productivity of milling upon the structure and sizes of the chips make it possible to recommend milling in BM as a preliminary operation of the technological process of recycling of the chips.

Candidate dispersing devices are vibrating mills and disintegrators. Chips with a diameter of 250 mm, preliminarily milled in BM to a particle size of 1500 μm, were used as the source material for milling in disintegrator. Milling conditions and particle size composition of the products of milling are given in Table 3. Comparatively large yield of the dispersed particles (about 100 μm) is achieved only by high-cycle dispersion (4 – 5 cycles). The investigations conducted revealed a substantial growth of power consumption when changing from milling of the cast iron chips to milling of the roll chips (Table 3). This shows that use of the disintegrating devices for commercial manufacture of powders with a particle size of less than 100 μm is not cost effective. In this connection, it seems more promising to manufacture powders from wastes of mill roll grinding.

Grinding of mill rolls is done using abrasive disks 25AS2K7 and LCF in the form of 1 % solution of soda ash. The resulting grinding slime is a moist paste-like mixture consisting of fine-dispersed cast iron chips, abrasive grains and abrasive disk binding material with a particle size of 0.005 – 2.500 mm. The high degree of dispersion of slimes is attributable mostly to grinding conditions and, first of all, to a small (0.05 mm) cutting depth.

Processing of slimes into powders included the following operations: drying of slimes in a drying cabinet at a temperature of 423 K for 3 h, short-time (10 min) milling of the dried material in BM, cyclone cleaning of slimes from dust-like fractions, and screening followed by magnetic separation to remove abrasive inclusions.

Table 3. Conditions of milling of chips in disintegrator

Cast iron grade	*Circumferential speed of rotors (m/s) in milling cycles**			*Composition of powders, wt.%*					*Energy consumption of milling, kW·h/kg*		
				Particle size, μm							
	1	*2*	*3*	*–50*	*+50 – –63*	*+63 – –100*	*+100 – –200*	*+200 – –400*	*–50*	*+50 – –63*	*+63 – –100*
SCh-21	220	260	300	11	35	45	9	—	0.8	0.51	0.40
SPKhN-49	170	200	280	6	20	35	30	9	1.4	0.72	0.54
SShKhNMD-63	140	180	260	5	17	28	40	10	1.7	0.90	0.62
LPKhN-63	130	150	240	5	15	20	45	15	2.1	1.60	1.00
LPKh17NM-58	120	150	240	5	12	19	44	20	2.4	1.80	1.20

*In milling cycles 4 and 5 the circumferential speed of rotors was 300 m/s.

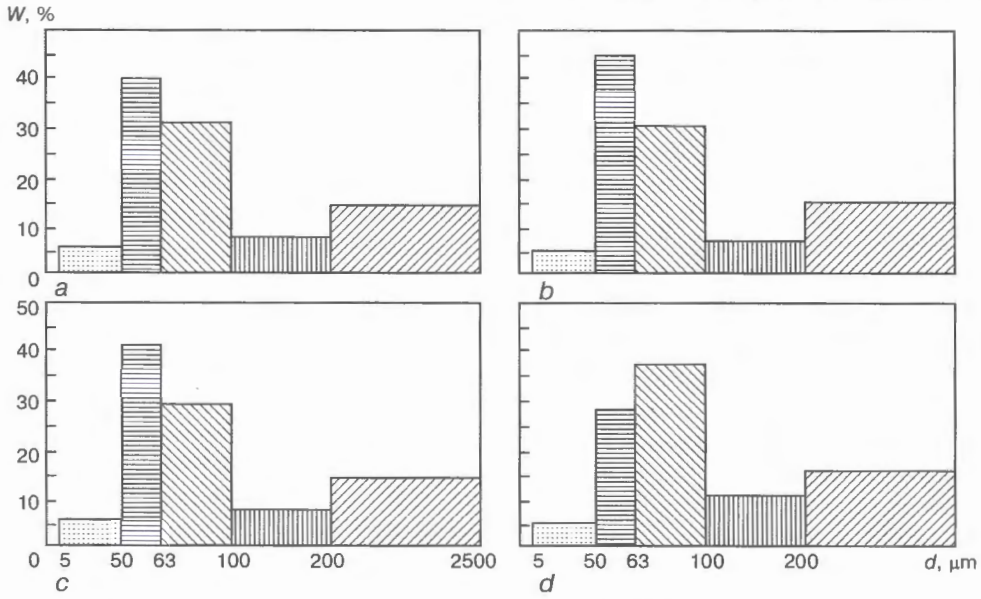

Figure 3. Particle size composition W of slime after cyclone cleaning: *a* — LPKhNM-76; *b* — LPKhNM-71; *c* — LPKhNM-73; *d* — LPKh17NM-71 (d is the size of slime particles, μm)

The content of particles 50 – 63 and 63 – 100 μm in size in ten batches of slime after cyclone cleaning (weight of each batch — 5 kg) was about 60 – 70 wt.% (Figure 3). The content of an abrasive in slime with a particle size of 50 – 63 μm was at a level of 10 – 12 wt.% and that with a particle size of 63 – 100 μm was at a level of 22 – 26 wt.% (Table 4). Concentration of the abrasive grains was determined from the ratio of mass of a separated corundum to that of the investigated batch of slime. The amount of a residual abrasive after magnetic separation was estimated by standard microscopic analysis of powders. In slimes with particles less than 50 μm in size, because of inefficiency of their magnetic cleaning, the weight content of an abrasive was determined by microscopic analysis of samples.

Results of chemical analysis of powders after cyclone cleaning and magnetic separation are given in Table 5. A non-cleaned slime contains a substantial amount (19.2 – 22.0 %) of silicon from the abrasive disk binder. In a finished product, the content of silicon is lower, i.e. 2.1 – 3.2 wt.% (Table 5). A decrease in the weight content of carbon, nickel, chromium and other alloying elements is attributable to the presence of the abrasive disk particles in powders. A decrease in the content of carbon from 3.0 to 2.6 – 2.8 wt.% and chromium from 1.10 to 0.76 – 0.81 wt.% can also be caused by spalling of graphite globules and carbides in grinding of the rolls [6, 7].

Results of investigations of technological properties of powders produced from the grinding slimes (Table 6) show that they are characterized by sufficient flowability and can be transported using standard feeding devices.

The processes of heat exchange between a spray material and the plasma jet are greatly affected by the morphology of particles. This factor determines to a considerable degree the difficulties which arise in transportation of powders. Powder particles up to 63 and 100 μm in size have mostly spherical or oval shape, torn edges and scores. In addition, these powders also contain needle-shaped particles 5 – 15 μm thick and 70 – 120 μm long.

Coatings of mechanical mixture of powders of LPKhNM-73 and self-fluxing nickel alloy PG-SR3 with a particle size of 63 – 100 μm were deposited by plasma spraying to determine the possibility of utilizing these powders for TS as components of powder mixtures or as an independent spray material.

Prior to spraying, the surface of samples of normalized steel 45 was subjected to abrasive-jet blasting

Table 4. Content of abrasive in powders, wt.%

Cast iron grade	*Particle size, μm*						
	–50	*+50 – –63*	*+63 – –100*	*+100 – –200*	*+200 – –400*	*+400 – –800*	*+800 – –2500*
LPKhN-71	23.8	12.2 / 2.7	24.4 / 2.1	40	50 – 55	~60	70 – 80
LPKhNM-76	26.4	12.0 / 2.8	27.8 / 2.2	48	54 – 60		
LPKhNM-73	26.0	14.4 / 3.0	26.0 / 2.3	48	54 – 60	~60	70 – 80
LPKh17NM-71	25.2	14.7 / 3.1	26.1 / 2.6	50	52 – 57		

Note. Here and in Table 6 the numerator gives data after cyclone cleaning and denominator — after magnetic separation of slime.

Table 5. Chemical composition of powders of chips LPKhNM-73 after cyclone cleaning and magnetic separation of slime

Particle size composition, μm	Content of elements, wt.%*					
	C	Si	Mn	Cr	Ni	P
50 – 63	2.60	3.2	0.61	0.76	3.05	0.32
63 – 100	2.76	2.1	0.63	0.79	3.45	0.37

*In different particle size compositions, the content of molybdenum was 24.0 and that of sulphur is 0.06 wt.%.

using corundum with a particle size of 0.4 – 0.8 mm. The standard machine UPU-3D with the PP-25 plasmatron (arc current I_a = 300 A, arc voltage U_a = 35 – 50 V) was used for spraying of the samples. A mixture of argon and nitrogen was used as the plasma gas. Strength of adhesion of the coatings was determined by the method of pulling out of a conical pin. Composition of the plasma gas mixture was selected on the basis of the following considerations. The quality of the plasma coatings (PC) is determined by temperature and velocity of particles at the moment of their collision with the substrate. A considerable increase in the efficiency of heat transfer from plasma to powder is achieved in the case of using high-enthalpy gas jets characterized by a high heat capacity and large length at relatively low temperatures.

However, in the case of an increased voltage of the constricted arc in molecular gases, it is necessary to use special power supplies with high operating and open-circuit voltages. Only the use of monoatomic plasma gases (e.g. argon) allows the use of conventional sources of electric current with an open-circuit voltage of 90 – 120 V to feed the constricted arc. The optimal combination of intensive heating of powders and plasma spraying equipment, featuring a comparatively high cost effectiveness, is achieved by forming the plasma jets of mixtures of monoatomic (argon) and polyatomic high-enthalpy gases (nitrogen and hydrogen).

The basic effect on adhesion strength of TSC is exerted by the stressed state of the coating–substrate system and structure of the transition zone, which can be regulated by thermal, chemical and technological methods, such as surface preparation, preheating of substrate, spraying distance, composition and flow rate of plasma gas and power input. Figures 4 and 5 show dependencies of adhesion strength of the plasma coatings upon spraying distance L and arc voltage U_a.

Adhesion strength of coatings (35 MPa) of the same thickness (0.6 – 0.7 mm), produced from a cleaned slime, is 1.7 – 1.8 times lower than that of coatings produced from the self-fluxing nickel alloy (60 – 65 MPa). Adhesion strength of coatings of cast iron powders with a particle size of 50 – 63 μm is 1.3 – 1.5 times lower than that of coatings of powders with a particle size of 63 – 100 μm. At the same time, powders with a particle size of 50 – 63 μm provide denser coatings. According to the data of [8, 9], coatings of self-fluxing Fe-based powders have higher adhesion strength σ_{ad} on structural steels than coatings of nickel alloys, which is caused to a substantial degree by better matching of their thermal expansion coefficients (TEC) with those of the substrate material. In this case, adhesion strength (40 MPa) of plasma coatings of powders with a particle size of 50 – 63 μm is somewhat higher than that of coatings of powders with a particle size of 63 – 100 μm (σ_{ad} = 34 – 36 MPa). Comparison of the results obtained is indicative of qualitative and quantitative differences in principles of formation of adhesion bonds in PC of self-fluxing alloys and materials having no self-fluxing effect. As TEC of the cast irons considered matches to a better degree TEC of the substrate than that of a self-fluxing Ni-based alloy, the adhesion strength depends not only upon the kind of a stressed state and residual stresses, but also upon the peculiarities of formation of the coating– substrate transition zone.

Analysis of dependencies shown in Figures 4 and 5 allowed the following assumptions to be made on the effect of spraying conditions on strength of adhesion of PC to the substrate. An increase in the spraying distance from 100 to 160 mm, in the case of an insufficient thermal power of the plasma jet at U_a = 40 V, is accompanied by cooling of particles, decrease in contact temperature and, thus, decrease in adhesion strength of coatings of the PG-SR3 nickel alloy powder from 65 to 47 MPa (Figure 4). An increase in the arc voltage to 45 – 50 V leads to an increase in the size of the high-temperature zone of the plasma jet and intensification of heat exchange between particles and plasma. This allows the coatings with a high (57 – 65 MPa) adhesion strength to be deposited over

Table 6. Technological properties of powders

Cast iron grade	Flowability, s			Apparent density, g/cm³		
	Particle size composition, μm					
	–50	+50 – –63	+63 – –100	–50	+50 – –63	+63 – –100
LPKhN-71	11	21/26	28/31	1.80	2.0/2.3	1.90/2.10
LPKhNM-76	12	19/24	26/29	1.70	2.0/2.3	1.80/2.18
LPKhNM-73	10	19/24	26/29	1.70	2.0/2.3	1.80/2.20
LPKh17NM-71	12	22/26	25/28	1.86	2.1/2.4	1.80/2.20

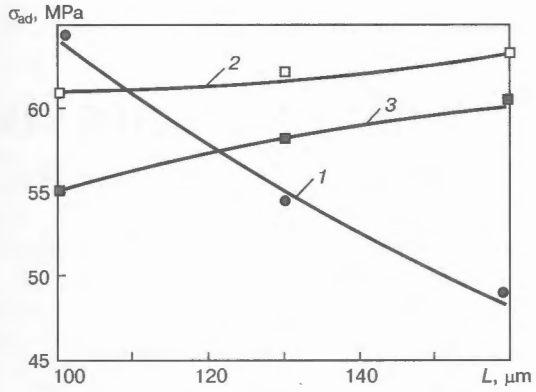

Figure 4. Dependence of adhesion strength of coatings of the PG-SR3 powder with a particle size of less than 100 μm upon the arc voltage at U_a = 40 (*1*), 45 (*2*) and 40 (*3*) V and spraying distance

a wide range of spraying distances (L = 100 – 160 mm). A comparatively low intensity of growth of adhesion strength for alloy PG-SR3 within the entire range of the spraying distances, L = 100 – 160 mm, at U_a = 45 – 50 V is associated with structural features of the eutectic alloy, which transfers into the liquid state and solidifies at a temperature of about 1000 K under any spraying conditions.

In spraying cast iron powders, a marked effect on adhesion strength is exerted by their particle size composition, spraying distance and arc voltage (curves *3* – *6* in Figure 5). A decrease in adhesion strength of coatings of powders with a particle size of 50 – 63 μm is attributable to overheating and oxidation of the spray particles. Formation of non-dissolved oxides on the particle surfaces with a melting temperature which is in excess of that of the base metal limits the adhesion strength values. In self-fluxing Fe-based alloys, plasma spraying of coatings of powders with a particle size of 50 – 63 μm is accompanied by a substantial (as compared to powders with a particle size of 63 – 100 and 100 – 160 μm) burning out of alloying elements, such as boron and carbon [8, 9]. In the electric-arc, flame and plasma coatings of flux-cored wires and powders of the Fe–B, Fe–B–Cr and 40Kh13 systems, the oxidation processes result in a 1.5 – 2.2 times decrease in strength characteristics of TSC [10, 11]. In the electric-arc coatings of flux-cored wire 40Kh13, an increase in the content of oxygen from 1.5 to 4.5 wt.% leads to a decrease in adhesion strength from 45 – 47 to 28 – 30 MPa. According to [2], the content of oxygen in PC of gray cast iron powders can reach 7.0 – 7.2 wt.%.

At the same degree of heating, the PG-SR3 particles remain in the liquid and ductile state for a longer time than the cast iron particles. Therefore, plastic deformation, processes of activation and physical-chemical interaction of particles with a substrate occur in the first case more intensively than in the second case, providing a higher strength of adhesion of the nickel alloy particles to the substrate. In spraying coatings of mechanical mixtures of cast iron powders and PG-SR3 alloy, an increase in the content of the latter from 0 to 100 wt.% leads to a linear increase in adhesion strength from 36 to 63 MPa.

PC of mechanical mixtures of cast iron and self-fluxing alloy powders are characterized by higher tri-

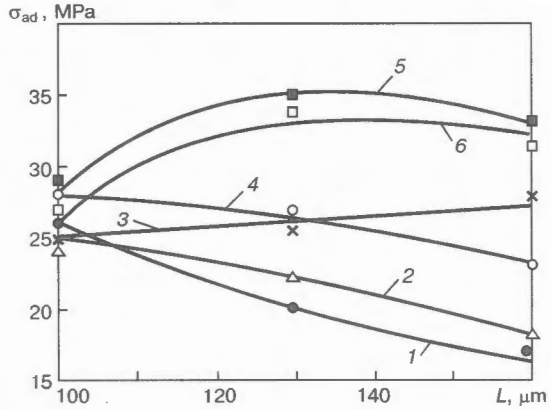

Figure 5. Dependence of adhesion strength of coatings of cast iron LPKhNM-73 upon the arc voltage at U_a = 35 (*1*), 40 (*2*), 40 (*3*) (particle size 50 – 63 μm), 40 (*4*), 45 (*5*) and 50 (*6*) V (particle size 63 – 100 μm) and spraying distance

bological properties than coatings sprayed of PG-SR3 alloy and cast iron powders separately. PC produced from mixtures of powders on crankshafts of cars and trucks passed the tests to advantage.

CONCLUSIONS

1. Slime is the most promising raw material for production of powders from wastes of machining of mill rolls. Processing of the slime provides a high (50 – 55 %) yield of materials with a particle size of 50 – 100 μm, which can be used for thermal spraying.

2. Plasma coatings of cast iron powders are characterized by a lower adhesion strength, as compared with self-fluxing alloys, and by a high porosity. Therefore, they are more efficient for deposition of wear-resistant coatings if used as a component of powder mixtures.

REFERENCES

1. Borisov, Yu.S., Kudinov, V.V. (1989) Thermal spray powders of wastes of metal working: Principles of production and prospects for application. *Poroshkovaya Metallurgia*, **10**, 25 – 30.
2. Borisov, Yu.S., Korzhyk, V.N., Panko, M.T. (1995) Development of the process of manufacture of thermal spray powders from gray cast iron chips. *Avtomaticheskaya Svarka*, **6**, 7 – 12.
3. Borovich, T.L., Kudinov, V.V., Pekshev, P.Yu. *et al.* (1983) Utilization of powders from wastes of various productions for spraying of coatings. In: *Interinst. Transact. on New Methods For Spraying Protective Coatings*. Kalinin: KSU.
4. Roman, O.V., Genkin, V.A., Dmitrovich, A.A. (1986) Porous material with improved performance for friction units operating in oil. In: *Transact. of IPM AN USSR on New Powder Materials*. Kyiv.
5. Skoblo, T.S., Vorontsov, N.M., Rudyuk, S.I. *et al.* (1994) *Mill rolls of high-carbon alloys*. Moscow: Metallurgia.
6. Budagiants, N.A., Karrsky, V.E. (1983) *Cast mill rolls*. Moscow: Metallurgia.
7. Libenson, G.A., Panov, V.S. (1983) *Equipment of powder metallurgy workshops*. Moscow: Metallurgia.
8. Nechiporenko, A.A., Martsevoi, E.P. (1995) Spraying of coatings from powders of self-fluxing iron-based alloys by the plasma-arc method. 1. Evaluation of temperature and velocity of powder particles in plasma flow. *Poroshkovaya Metallurgia*, **1/2**, 35 – 40.
9. Nechiporenko, A.A., Martsevoi, E.P. (1995) Spraying of coatings from powders of self-fluxing iron-based alloys by the plasma-arc method. 2. Structure and properties of coatings. *Ibid.*, **3/4**, 35 – 40.
10. Koziakov, I.A., Korzhyk, V.N., Borisov, Yu.S. (1996) Strength of amorphized flame-spray coatings produced by using flux-cored wires of the Fe–B system under conditions of abrasive wear. *Avtomaticheskaya Svarka*, **11**, 21 – 23.
11. Ivashko, V.S., Belotserkovsky, K.V., Bujkus, K.V. (1999) Repair of friction unit components by activated arc metallizing. *Ibid.*, **4**, 47 – 49.

SEMI-AUTOMATIC DEVICE FOR WELDING TUBES TO TUBE SHEETS FOR SMALL-SIZE HEAT EXCHANGERS

M.I. CHERNOMOROV
East-Ukrainian National University, Lugansk, Ukraine

ABSTRACT

To produce quality permanent joints of the tube-to-tube sheet type, a portable device has been developed, which makes it possible to perform gas-shielded welding of 3 – 5 mm diameter tubes with a preset penetration depth.

Key words: *argon-arc welding, tube sheets, semi-automatic device, heat exchanger*

Modern engineering (chemical, power generation, etc.) requires new upgraded equipment and imposes stringent requirements on its strength, reliability and performance. As a rule, pieces of this type can be made only by fusion welding. These pieces of equipment also include parts of Stirling engines or engines with an external heat supply. Heat exchangers [1] comprising tubes and tube sheets are also regarded as the most critical structures.

Small-size heat exchangers operate under severe conditions: high temperatures, high pressures and helium gas as a working medium. This predetermines requirements to the welds: they should be strong and tight with a guaranteed penetration depth. In manufacture of a heat exchanger comprising 1000 tubes, only 1 % of reject caused by welding leads to the necessity of caulking of 10 tubes, which decreases the efficiency of welding by 18 %. Heat exchanging devices can be made from different materials, although the most extensively used materials are high-alloy and stainless steels. This causes a lot of problems in development of specific technological processes. Thus, welding of tubes to tube sheets may result in a non-uniform penetration, formation of circular cracks, pores and other defects. These drawbacks become apparent in welding small-diameter (3 – 5 mm) tubes to thick (20 – 60 mm) tube sheets.

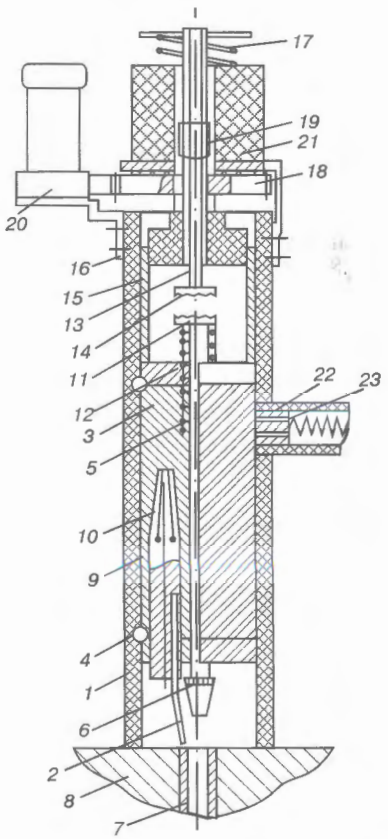

Figure 1. Semi-automatic welding device for making small-diameter circumferential welds (designations here and in Figure 2 are given in the text)

Choice of a welding method is based on a specific type of structure, quantity of welds to be made, their location, service conditions and test methods. The most extensive use for such purposes is made of fusion welding, which is regarded as an independent technological operation. In the case of a large number of welds, it is necessary to have a specialized equipment to ensure their consistent geometry. The East-Ukrainian National University developed a device for welding in the automatic mode of tubes with a diameter of more than 1 mm into tube sheets. The device provides a high quality of the welds [2]. The semi-automatic device allows welds of a small cross section (Figure 1) to be made by the argon-arc tungsten-electrode method. It consists of dielectric fixed casing *1*, which houses electrode rotation mechanism *2* in movable casing *3*. Casings *1* and *3* are connected to each other via balls *4*, which enter the casings by halves to form a combined bearing. Casing *3* has a central hole for aligner *5*, whose lower end is fitted with replaceable extension piece *6* in the form of a cone made from a heat-resistant material (e.g. ceramics, steel). Its root diameter is larger by 0.2 – 0.4 mm than the inside diameter of tube *7* welded into tube sheet *8*. Casing *3* also has an eccentric hole for electrode holder *9*. The upper (bottom) part of the eccentric hole is conical, and the tailing part of the electrode holder has longitudinal slots *10*. When it is installed in casing *3*, the conical surface bends the slotted part of the electrode holder towards the centre. This induces elastic forces which cause its tailing part

to return back to the initial (cylindrical) position. Owing to this, electrode holder *9* is reliably fixed in casing *3*, which provides a good electric contact between them. In addition to improvement of reliability of operation of the device, this also leads to a decrease in requirements for accuracy of making of the internal surface of the eccentric hole and the external surface of the electrode holder. The latter also has an eccentric hole for installation of non-consumable electrode *2*, allowing the position of electrode *2* to be varied (moved off) with respect to the main axis of the device by turning electrode holder *9* about its longitudinal axis. This provides a smooth variation of the diameter of rotation of the electrode within a wide range. The upper end of aligner *5* has tip *11* with radial rippling. Opposing spring *12* is installed under it to lift the aligner over tube *7* to be welded (in Figure 1 the spring *12* is shown in a free position). Rod *13*, whose lower end also has tip *14* with radial rippling, is coaxially located over aligner *5*. Drive shell *15*, half-coupling *16* and opposing spring *17* of rod *13* are located over casing *3*. Half-coupling *16* is fitted with driven gear *18*, which interacts through longitudinal riffling in the central hole with rod *13*, also having longitudinal riffling *19*. Driven gear *18* is set into rotation from drive *20*, which can be mounted directly on dielectric casing *1* or outside it. Electromagnet *21* secured to casing *1* is placed over driven gear *18* with no connection to it.

The semi-automatic device operates as follows. Prior to use of the device, extension piece *6*, matching the diameter of tube *7*, is screwed on the lower end of aligner *5*. Then electrode holder *9* is turned so that distance from electrode *2* to the longitudinal axis of the device corresponds to the outside diameter of tube *7*. The device is placed on tube sheet *8*, and, after pressing rod *13* (manually or by switching on electromagnet *21*), aligner *5* is moved until extension piece *6* contacts tube *7*. In doing so, the axes of the device and the tube are aligned. In this position the device is fixed by a rack or held manually. After this rod *13* is released, springs *17* and *12* return back to the initial position to lift rod *13* and aligner *5*, respectively. Then rotation drive *20* is switched on, which transfers the torque to casing *3* through components *18*, *16* and *15*. The welding current is supplied through brushes *22*, and the shielding gas is fed through hole *23*. The gas is fed to the welding zone via the longitudinal slots on the surface of casing *3*, washing this surface and cooling the casing. Upon completing the circumferential weld on the entire diameter of tube *7* (for this electrode *2* is rotated at a high speed of about 900 – 1200 rpm), the welding

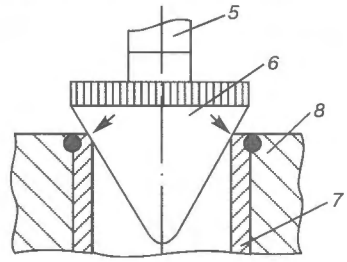

Figure 2. Schematic of the effect exerted by the extension piece on the circumferential weld

current is turned off, the rotation drive being left in the «on» position. Then electromagnet *21* is switched on. Rod *13* is lowered under the effect of the longitudinal magnetic field, while rotating due to interaction of riffling *19* with a matching riffling in gear *18*. Lowering of rotating rod *13* causes mutual engagement of tips *11* and *14*, which in turn causes rotation of aligner *5*. Aligner *5*, while lowering, enters inside welded tube *7* (Figure 2), and extension piece *6* exerts pressure on the weld in a radial direction. This leads to its plastic deformation in a direction of action of the shrinkage force, which results in a decrease in the level of tensile stresses [3]. Owing to rotation of extension piece *6*, the efficiency of impact on the weld increases to cause closing (grinding) of microdefects (cracks, pores), and the weld is sealed. After complete cooling of the weld rotation drive *20* and electromagnet *21* are switched off, and the device is used again.

The device developed has limitations as to welding conditions, which are caused by thickness of the tubes welded. As the tubes to be welded normally have a small thickness, the following welding parameters were set:

Welding current, A	80 – 150
Arc voltage, V	18 – 28
Welding speed, m/h	16 – 30
Electrode diameter, m	0.001 – 0.003
Shielding gas flow rate, l/min	9 – 16

Application of the semi-automatic device makes it possible to produce welds of the 100 % quality (independently of the quantity of the tubes) in the tube-to-tube sheet joints welded in the flat position. The device has been industrially validated.

REFERENCES

1. Baklistov, A.M., Gorbenko, V.A., Udyma, P.G. (1981) *Design, assembly and operation of heat exchanging devices*. Moscow: Energoizdat.
2. Chernomorov, M.I., Gedrovich, A.I., Kalyuzhny, V.K. USSR author's certificate **1586883**, Int. Cl. B 23 K 31/02, 37/02. Publ. 23.08.90.
3. Sagalevich, V.M. (1974) *Methods for elimination of welding strains and stresses*. Moscow: Mashinostroyeniye.

STATISTIC REGULATION OF WELDING TECHNOLOGICAL PROCESSES USING THE METHOD OF CONSTRUCTION OF CHARTS OF CONDITION CONTROL

I.A. TARARYCHKIN
East-Ukrainian National University, Lugansk, Ukraine

ABSTRACT

Method of construction of control charts of the condition of the technological process without use of graphs is suggested. Algorithm of estimation is simplified by using a complex criterion. The method capabilities are described on the example of the narrow-gap arc welding of a butt joint.

Key words: *statistic regulation, quality assurance, estimation of process condition, procedure, control charts, narrow-gap welding, corrective actions*

Statistic regulation of welding technological processes is connected with a need in a periodic estimation of their condition in the solution of problems of the quality assurance of products [1 – 4]. This kind of estimation should envisage the definition of the current process condition and tendency of its changing with time (development of prediction estimates); timely action on the process condition with a next estimation of efficiency of the corrective actions; documenting of the process condition to form the data of its history that corresponds to the requirements of objectivity and conclusiveness, including those in definite situations when the representatives of the customer or body on certification have an opportunity to get familiar with an inspection documentation characterizing the progress in the order fulfilment.

Among the statistic methods allowing inspection and prediction of the quality of products and, consequently, the process condition at different stages of manufacturing, a method of construction of control charts is most widely spread [5]. The traditional scheme of use of the method of control charts (Shewhart's charts) is associated with the necessity of a periodic sampling from the arrival of products and statistic processing of results of fulfilment of the check-out operations. It means that the regulation of processes using the Shewhart's charts corresponds to the greatest extent to the conditions of large-batch or mass production, where there is possibility of a periodic inspection of separate batches or a group of products. However, with respect to the conditions of a single- or small-batch production this method can be not acceptable or low-efficient. If the single-batch production is characterized by a high cost of the production unit, complication in check-out operations, high labour intensity in works for the elimination of defects, then it is rational to inspect directly the condition of the technological process.

Thus, the development of effective methods of inspection, regulation and documenting of the condition of the technological processes in the conditions of a single- and small-batch production is an actual problem, which appears, for example, in using such processes as narrow-gap welding, electroslag, electron beam welding of large-sized structures. Under these conditions the development of the procedure of construction of charts of the process condition control, from the appearance of which it would be possible to estimate its current condition and to predict the tendency of progress, presents interest.

To solve the above-formulated problems it is necessary to define preliminary the process parameter to be checked-out X, which influences significantly its condition and, as a consequence, the quality of products. Then, the requirements to an allowable range of X variation should be formulated (design allowance should be indicated). The number of check-out measurements n and periodicity of their fulfilment should be set in accordance with the technological documentation.

The procedure of processing data is connected with defining of the following characteristics:

• mean value of the check-out parameter $\bar{x}$ and standard deviation S

$$\bar{x} = \sum x_i/n, \tag{1}$$

$$S = \sqrt{\sum (x_i - \bar{x})^2/(n-1)}; \tag{2}$$

• value of a real range of changing the check-out parameter of the process (technological field of allowance) ΔU

$$\Delta U = \sqrt{2}\, S\Phi^{-1}(P), \tag{3}$$

where P is the probability with which a random value X enters the boundaries of the technological field of allowance; $\Phi^{-1}(P)$ is the function, Laplace's inverse

Requirements to the technological process accuracy

Parameter of process accuracy	Accuracy		
	Moderate and mean	Increased	High
P	0.940 – 0.970	0.970 – 0.990	0.990 – 0.999
$\Phi^{-1}(P)$	1.33 – 1.54	1.54 – 1.82	1.82 – 2.35

function [6]. Values $\Phi^{-1}(P)$ can be determined from the Table data depending on the requirements specified to the accuracy of the technological process;

• coefficient of dissipation η, characterizing the relation between fields of technological and design allowances

$$\eta = \Delta U/(W_u - W_l), \qquad (4)$$

where W_u, W_l are, respectively, upper and lower boundaries of design field of allowance, established at the stage of the technology development coming from the need of providing preset conditions of the process proceeding. These can be, for example, requirements to the accuracy of the process, whose fulfilment guarantees the absence of the shape defects in the formation of the weld;

• coefficient of deviation of setting θ characterizing the deviation of the center of distribution of the checked-out characteristics X with respect to the middle of the design allowance field

$$\theta = 2\,|\,\bar{x} - W_0\,|\,/(W_u - W_l), \qquad (5)$$

where $W_0 = (W_u + W_l)/2$ is the middle of the design allowance field.

The current condition of the technological process can be characterized by a position of point $Z(\theta, \eta)$ in the system of coordinates $\theta 0\eta$. It is seen that if the condition of the process is satisfactory, then the point $Z(\theta, \eta)$ enters the region D (Figure 1) [7]. Otherwise, the process does not correspond to the specified requirements and requires correction. As the characteristics of accuracy of the process θ and η can change with time, then the condition of the process can be described by a sequential system of points $Z_1, Z_2, \ldots, Z_c$ on the plane $\theta 0\eta$ determined for the time moments $t_1, t_2, \ldots, t_c$. If the process condition satisfies the requirements to the accuracy, then all the points $Z_1, Z_2, \ldots, Z_c$ will locate within the region D (Figure 2, scheme 1). If from the moment of time t_j the corresponding point Z_j comes beyond the region D, it means that the process does not correspond to the specified requirements to the accuracy and the correction is required (Figure 2, scheme 2).

Thus, the analysis of the condition of the technological process is reduced to the determination of the current position of point $Z(\theta, \eta)$ relative to region D on plane $\theta 0\eta$. To obtain more detailed information about the process condition it is rational to divide the region D into three areas of a smaller size D_1, D_2, D_3 (see Figure 1). Their boundaries can be defined coming from the considerations of a practical nature, if

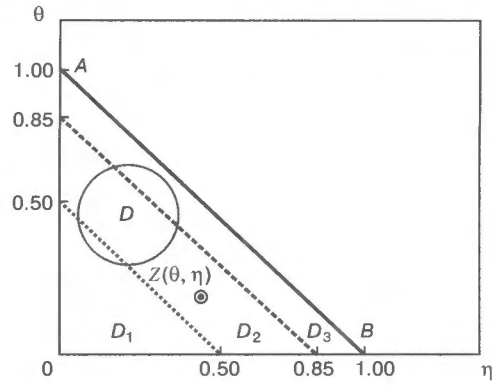

Figure 1. Scheme of mutual arrangement of regions D, D_1, D_2, D_3

to take such process condition optimum at which the condition $0.50 < \theta + \eta < 0.85$ is fulfilled, which defines the boundaries of region D_2 and, thus, the position of regions D_1 and D_3 (see Figure 1). The presence of field D_3 provides some accuracy margin before the process approaches the limiting condition (Figure 1, length AB) that makes it possible to obtain a definite spare time for taking decisions and fulfilment of appropriate corrective actions. The process, for which the position of point $Z(\theta, \eta)$ corresponds to region D_1 is excessively accurate and the use in this case of a high-precision equipment is not, probably, justified [8]. The use of the graphs on plane $\theta 0\eta$ makes it possible to perform the periodic estimation of the process condition in accordance with a suggested algorithm. The process condition can be recognized satisfactory if the current position of point Z_i corresponds to the region D_1 or D_2. If the point Z_i is transferred to the region D_3, then it is necessary to clarify the causes of accuracy violation and to make corrections. In that case when the point Z_i comes beyond the region D, then the process of manufacturing should be interrupted for revealing and eliminating causes of the accuracy violation.

The presented scheme can estimate the condition of the process using the graphs on the plane $\theta 0\eta$. However, it should be noted, that in the conditions of a real production the fulfilment of these graphs encounters certain difficulties. At the same time the algorithm of estimation can be simplified greatly if to use an integrated criterion of accuracy g_s of the following kind:

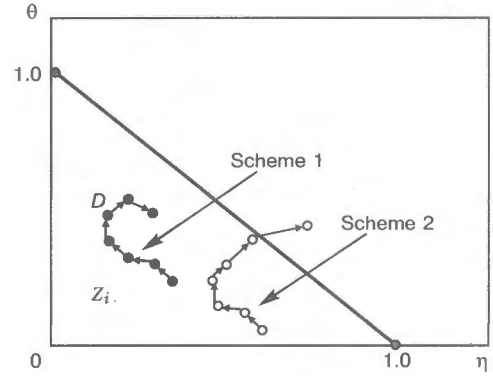

Figure 2. Schematic presentation of different versions of changing the accuracy of technological process with time

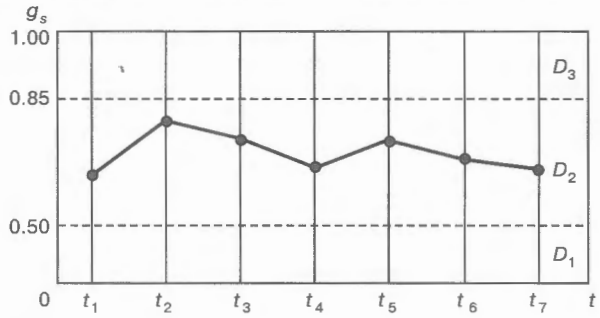

Figure 3. Appearance of control charts of technological process condition with plotted control lines and limiting condition boundaries

$$g_s = \theta + \eta = \frac{2\,|\,\bar{x} - W_0\,| + \Delta U}{W_u - W_l}, \qquad (6)$$

which makes it possible to determine the position of point $Z(\theta, \eta)$ with respect to regions D, D_1, D_2, D_3 and to estimate the process condition not using the graphs.

Thus, if $g_s < 0.50$, then the process analyzed meets the specified requirements, being here excessively accurate (Figure 1, region D_1). If $0.50 < g_s < 0.85$, then the process is proceeding under the optimum condition (Figure 1, region D_2). If $0.85 < g_s < 1$, then the process is characterized by an acceptable condition, however, requires correction as it is proceeding near the boundary of the limiting condition (Figure 1, region D_3). If $g_s > 1$, then the point $Z(\theta, \eta)$ is located beyond the region D and, consequently, the process analyzed does not meet the specified requirements of accuracy.

Thus, the suggested procedure of construction of control charts of the process is reduced to the construction of the system of values $g_s(t_i)$ determined for the set moments of time t_i, in accordance with the described approach. The presence of control lines of a kind $g_s = 0.85$ and 0.50, and also boundaries of the limiting condition $g_s = 1.00$ at the chart of process condition control simplifies the procedure of estimation and makes it more illustrative.

The construction of control charts is suggested to perform as follows:

- to estimate the process condition periodically for moments of time t_i, $i = 1, 2, \ldots, m$ with a definition of appropriate values X_i and S_i;
- to determine the value of parameter $g_s(t_i)$ by formula (6) for the current moment of time t_i;
- to put the estimated values $g_s(t_i)$ on the chart of control of the process condition, shown in Figure 3.

The process condition should be estimated as follows:

- if the nature of changing the position of control points $g_s(t_i)$ corresponds to scheme 1 (Figure 4), then the process should be corrected after sixth check-out measurement;
- if the process is proceeding according to scheme 2 (Figure 4), then, starting from the second check-out measurement, it does not correspond the specified requirement and the quality of the products will not be probably provided;
- if the process is proceeding according to scheme 3, then the accuracy is continuously increased and from the moment of time t_3 it becomes excessively accurate.

The acceptable properties are typical for the processes for which the position of control points corresponds to the region D_2 (see Figure 3).

It should be noted that the developed procedure of construction of the control charts of the process condition cannot be considered as the generalization or alternative to Shewhart's charts. The suggested method of statistic regulation of technological processes represents a self-sustaining tool which has its own field of a rational application connected, first of all, with direct control and documenting of the process condition under the conditions of a single- or small-batch production.

Let us consider the feasibility of the suggested method of estimation of the process condition on the example of the narrow-gap welding of butt joint of 60 mm thick metal. The groove is filled by a scheme of one layer per a pass (Figure 5), therefore, the electrode deviation from the gap axis can lead to the formation of defects of the layer shape in the form of undercuts or lack of fusion. In accordance with the requirements of the technology the deviation of the electrode axis from the gap middle should not exceed 12 % of the current width of gap $2B$. The accuracy control of electrode positioning in the gap was made in three points along the joint length ($n = 3$). The corresponding values of parameter $g_s(m)$ for seven

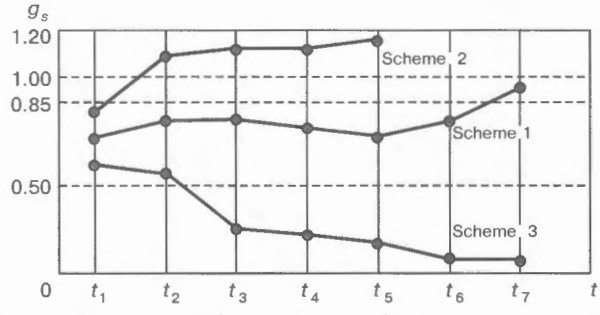

Figure 4. Appearance of control charts of condition depending on the scheme of technological process proceeding

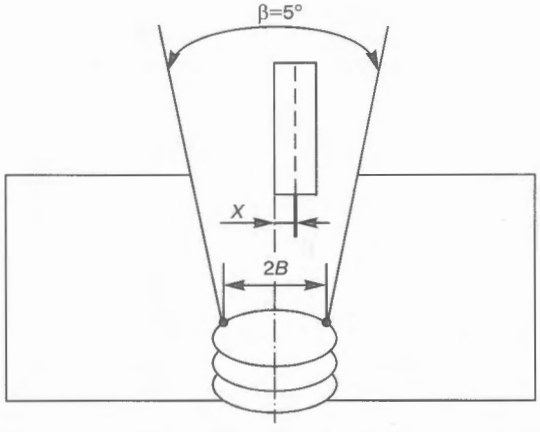

Figure 5. Diagram of appearance of electrode deviation from the gap axis in welding

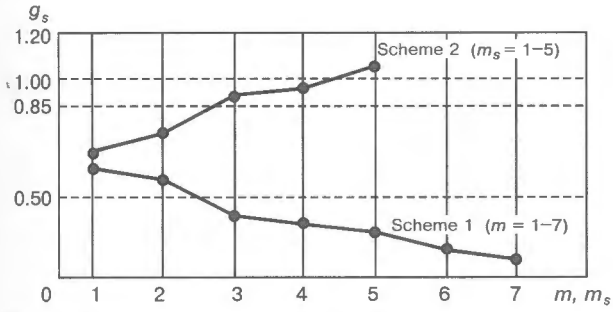

Figure 6. Nature of changing the process condition from layer to layer (scheme 1) and from product to product (scheme 2)

passes (m = 1, 2, ..., 7) are plotted on the control chart (Figure 6, scheme 1).

The obtained data show that the process accuracy is growing with time. This is explained by the fact that during the gap filling the current width of gap $2B$ is increased and, respectively, the allowable value of the electrode deviation from the gap axis is increased.

At the same chart the data of the process condition are plotted in welding of first passes for five successive welded joints (m_s = 1 – 5). It is evident (Figure 6, scheme 2), that the process accuracy is decreased gradually. This is, probably, due to the effect of a gradual wear of a contact tip of the torch. As a result the first layer of the fifth joint (m_s = 5) is made under the conditions, which do not meet the requirements specified for the process. At a proper organizing of works within the scope of the functioning system of quality at the enterprise the search for causes of accuracy violation in this case should be made after welding of the third or fourth joint. In this case the procedure of performance of the works should envisage the finding of causes of appearance of deviations, taking measures for their elimination with a subsequent estimation of effectiveness of the corrective actions [9].

The above-considered example is connected with an analysis of a unidimensional process, when its condition is estimated using one controllable parameter. The real welding processes are, as a rule, multidimensional and these are the processes for which the problem of the condition control and quality assurance is actual.

The estimation of condition of the multidimensional processes with use of suggested control charts is performed similar to the unidimensional processes. The difference consists in that the construction of several charts for each of preset controllable parameters of the process X_1, X_2, ..., X_r is realized simultaneously. The process condition is recognized satisfactory if all the corresponding criteria g_{s1}, g_{s2}, ..., g_{sr} do not exceed unity in their values.

After analyzing the case of the narrow-gap welding of 60 mm thick metal it should be noted that the feasibility of formation of the shape defects in welding is due not only to the deviation of the electrode from the gap axis, but also with possible change in the width of gap $2B$, as a result of development of angular deformations, with a change in electrode stickout h_e,

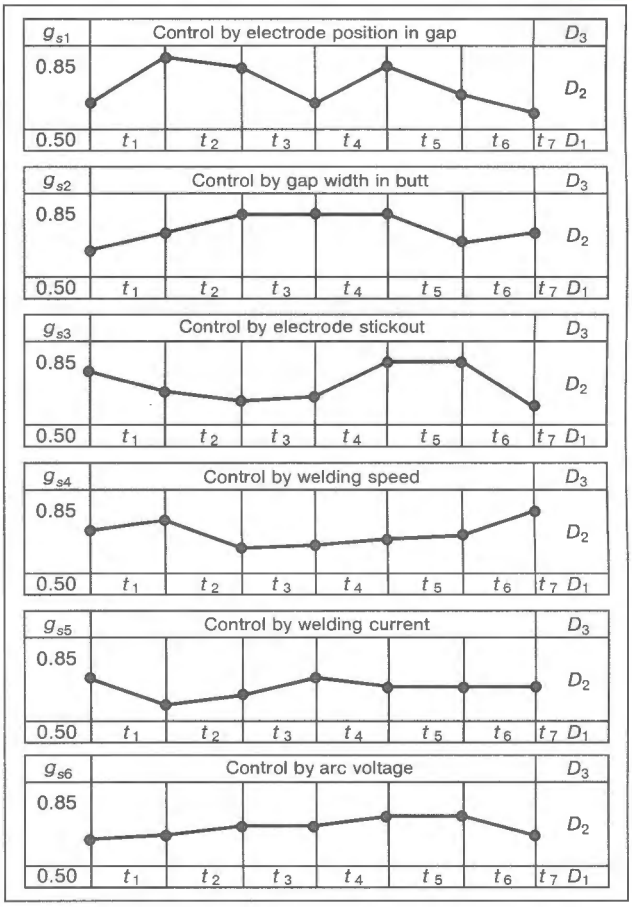

Figure 7. Type of control of condition of multidimensional process of welding

welding speed v_w, welding current I_w, arc voltage U_a. If to perform the control and documenting of the process condition using all the above-listed parameters, then the six-dimensional system will be controlled, for the description of which the simultaneous construction of six control charts of condition is required. The appearance of the control charts of the process condition for the considered six-dimensional system, which meets all requirements of accuracy is given in Figure 7.

REFERENCES

1. *ISO 9001–94*. Quality systems. Model of quality assurance in designing, development, manufacture, assembly and maintenance.
2. *ISO 9002–94*. Quality systems. Model of quality assurance in manufacture, assembly and maintenance.
3. *DSTU ISO 9004-1–95*. Quality management and elements of the quality system. Part 1. Recommendations.
4. Volchenko, V.N., Gurvich, A.K., Majorov, A.N. *et al.* (1975) *Quality control of welding*. Moscow: Mashinostroyeniye.
5. Nouler, L., Hawell, J., Gold, B. *et al.* (1984) *Statistic methods of quality control of products*. Moscow: Izdat. Standartov.
6. Venttsel, E.S. (1962) *Theory of probabilities*. Moscow: Fizmatgiz.
7. Tararychkin, I.A. (2000) Development of methods of estimation of characteristics of technological process based on the requirements of international standards ISO series 9000. *Visnyk SUDU*, **9**, 238 – 242.
8. Tararychkin, I.A. (2001) Optimizing of technology of welding processes in the solution of problems of quality assurance of products. *Svarochnoye Proizvodstvo*, **1**, 4850.
9. (1990) *Seven tools of quality in the Japanese economy*. Moscow: Izdat. Standartov.

CHEMICAL MICROHETEROGENEITY AT THE GRAIN BOUNDARIES OF HAZ METAL OF MARTENSITIC-BAINITIC STEEL 14KhGN2MDAFB

L.I. MIKHODUJ, O.D. SMIYAN, M.B. MOVCHAN, V.D. POZNYAKOV and **S.O. ANTONOV**
The E.O. Paton Electric Welding Institute, NASU, Kyiv, Ukraine

ABSTRACT

The process of a delayed fracture of HAZ in implant samples made from steel 14KhGN2MDAFB at the pre-fracture stage was examined using the method of electron Auger-spectrometry. It was established that during the delayed fracture of the welded joints the HAZ metal is subjected to redistribution of alloying and impurity elements inside the grains, enrichment of their boundaries by a number of embrittling impurity atoms that is an additional (except hydrogen) factor, predetermining the metal fracture at this type of tests.

Key words: *high-strength steel, welded joint, heat-affected zone, Auger-spectrometry, tensile stresses, segregation of alloying and impurity elements, inhomogeneity, delayed fracture*

In most investigations devoted to a delayed fracture (DF) of welded joints made of the alloyed steels the effect of either indirect parameters, characterizing the metal structure (temperature of austenite transformation, amount of martensite, microhardness, etc.) or inhomogeneities of this structure are considered [1, 2]. At the same time the insufficient attention is paid to the study of development of a chemical microheterogeneity in the DF process. Hydrogen, being one of main causes of cold cracking in DF, is an exception [3 – 6]. However, the behaviour of the rest chemical elements, available in steel, is not known in many cases.

As a result of action of the welding thermal cycle the intensive growth of grains occurs, as rule, in the near-weld regions of the alloyed steels. This leads to the widening of the boundaries and accumulation of different kinds of defects and impurities along them. In HAZ metal, both compressive and tensile stresses are acting. The compressive stresses hinder, and the tensile stresses promote the development of segregation processes and metal fracture. The degree of this influence and also a possible nature of processes of mass transfer and redistribution of alloying and impurity elements in these microvolumes are not clear.

Over the recent years the problems connected with the fracture of metals due to microchemical inhomogeneity are studied comprehensively in metallurgy. To perform these investigations, the method of electron Auger-spectrometry (EAS) is used mainly, as its information depth (2 – 3 nm) is commensurable with a thickness of the intergranular layers, equal to 20 – 30 nm [7]. These investigations were made, as a rule, on fractures which were subjected to the action of the surrounding medium. Therefore, each time the purity of the experiment was under the question as the samples entered for investigation were covered with a relatively thick layer of oxides or adsorbates. After removal of these surface impurities using ion etching in the chamber of analysis of the Auger-spectrometer, it was possible easily «to remove» also a part of the useful information about the real composition of the fracture surface proper. If, by any reasons, the metal, adjacent to the grain boundary (GB) was enriched with impurities, then there were no problems and all the changes were taken into consideration [8, 9]. From their results much real information was obtained about the composition of GB and effect of separate chemical elements on the fracture of metals [8 – 13]. When the causes of hot cracking in austenitic steels of 10Kh23N18 type, and also in Fe–34Ni alloy were analyzed the metal was subjected to deforming at 550 – 850 °C temperature using different rates.

The investigations showed that GB of these steels are enriched with oxygen and sulphur, which cause the metal embrittlement at the above-mentioned temperatures [9]. In case of fracture in vacuum $5 \cdot 10^{-7}$ Pa of R6M5 type tool steel samples, which passed the heat treatment at a subsequent examination of the surface fracture using the EAS it was shown that phosphorous is a harmful impurity for these steels [13]. The clusters of impurity atoms can be formed in the conditions of low temperatures not only under the action of the deformation, but also at the presence of thermal stresses, cyclic stresses in particular. For example, the thermal cycling at temperature from −150 to +150 °C causes not only destroying of higher oxides of metals and metal saturation with hydrogen, but also the redistribution of impurity and alloying elements in steel 12Kh18N10T [10]. In all these examinations the «freely arranged» metal was subjected to thermal and deformational action, i.e. metal, which is capable to change its form and structure freely. At a DF in the conditions of a confined deformation the process of initiation and propagation of cold cracks in the welded joints occurs mostly at loads which are

Table 1. Conditions of preparation of 14KhGN2MDAFB steel samples for tests

No. of series of sample	*Conditions of preparation and sample region to be analyzed*	*Conditions of loading of implant samples*
1	Parent (initial) metal	–
2	Parent metal is annealed at 800 °C for 2 h	–
3	HAZ after welding	–
4	Same	σ_4 = 610 MPa, 5 min
5	»	σ_5 = 255 MPa, 30 min

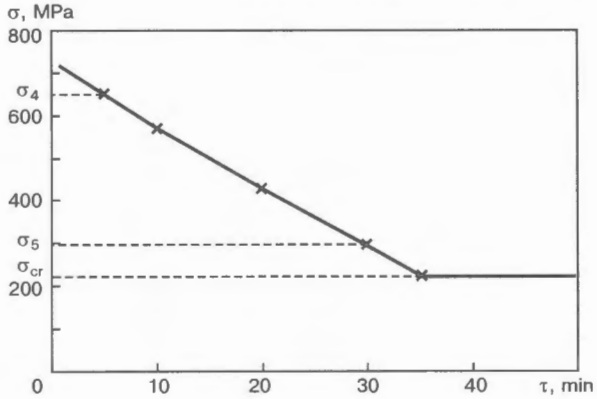

Figure 1. Curves of DF of implant samples (steel 14KhGN2MDAFB)

lower than the yield strength of the parent metal. Therefore, some specific features can be expected in proceeding of processes of migration, redistribution of impurity atoms in the near-weld zone metal and the nature of its fracture. The aim of the present work is to analyze the chemical composition of GB of the HAZ metal, being the pre-fracture state, under the action of the static load.

The most unfavourable conditions of testing implant samples (Table 1), made from high-strength steel 14KhGN2MDAFB, were selected as basic for investigations. The required complex of properties in this steel ($\sigma_{0.2} \geq 690$ MPa, $\sigma_t \geq 790$ MPa, $\delta_5 \geq 14$ % and $KCV^{-40} \geq 39$ J/cm^2) is reached at a mass fraction of carbon up to 0.17 %, complex alloying, microalloying, and also after refining and heat treatment (quenching and tempering). For manufacture of implant samples the steel of $\sigma_{0.2}$ = 815 MPa, σ_t = = 928 MPa and the following mass fraction of chemical elements, %: C – 0.14; Si – 0.37; Mn – 1.36; Cr – 1.23; Ni – 2.2; Mo – 0.22; V – 0.15; Al – 0.03; Nb – 0.07; Cu – 0.45; N – 0.014; Si – 0.008, were used. The implant samples were manufactured by a manual arc welding with electrodes ANP-9 (C – 0.08; Si – 0.3; Mn – 0.96; Cr – 0.4; Ni – 2.5; Mo – 0.3; S – 0.017; P – 0.02 wt.%) of 4 mm diameter without preheating. Here, the conditions of preparation of electrodes and welding conditions (I_w = 170 – 180 A, U_a = 24 – 25 V, v_w = 9.0 – 9.5 m/h) remained unchanged. This made it possible to maintain constant rate of HAZ metal cooling within the interval of 600 – 500 °C temperatures ($w_{6/5}$ = = 25 – 26 °C/s) and limited content of diffusive hydrogen in the deposited metal (at the level of 3.5 – 4.5 ml/100 g). Under these conditions of welding and cooling the structure of HAZ metal of steel 14KhGN2MDAFB contains about 85 % martensite, the rest – bainite [14].

In the process of cooling to temperatures 100 – 150 °C the implant sample was loaded for 1 min to reach the constant preset force, then it was subjected to the selected load during a time to cause the fracture. The graph of relationship between the metal stress, σ, occurred under the action of this load, and the loading time, τ, for the above-mentioned technological condition of welding is given in Figure 1. Maximum tensile stress σ_{cr} caused by external load at which the implant samples are not fractured during 20 h is assumed as a characteristic of crack resistance of a definite technological variant in the process of which the HAZ metal is resistant to the cold crack formation [1].

With a study of fractures of specimens, being cut from the implant samples after their loading at recorded conditions of tension, it is possible to investigate the separate stages of the process of initiation and growth of cracks under the conditions of a DF at definite loads using an interruption of the tension process for some time until the moment of fracture. This procedure makes it possible to study the processes associated with a change in chemical composition of GB metal of the sample in the pre-fracture state. Therefore, the implant samples were subjected to such action of the load (see Table 1) which was removed 1 – 2 min before the expected moment of fracture. Then, the specimen was cut from the sample central part in the form of 3.9 mm diameter bar with a boring-notch (Figure 2) which was made in the near-weld zone. The specimens were subjected to the final fracture inside the installation LAS -2000 in vacuum $1 \cdot 10^{-8}$ Pa during cooling with liquid nitrogen vapours to the temperature –160 °C. This made it possible to produce the brittle intercrystalline fractures and to examine directly the intergranular surfaces, GB, their chemical and element composition, distribution of elements from GB into the depths of its body. In these conditions ($p = 1 \cdot 10^{-8}$ Pa) a single-layer of adsorbates is

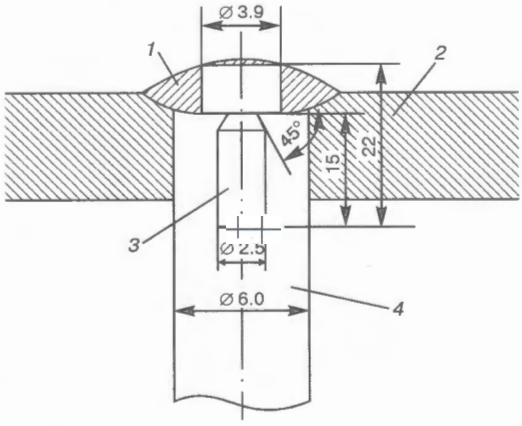

Figure 2. Diagram of cutting specimens from the implant sample: *1* – deposit; *2* – support plate; *3* – test specimen; *4* – implant sample

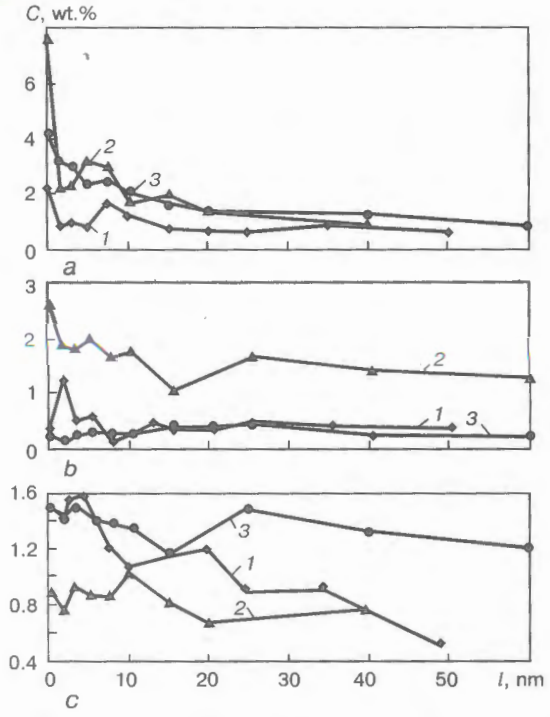

Figure 3. Distribution of oxygen (*a*), sulphur (*b*), carbon (*c*) at the GB and adjacent grain body in metal of specimens of series No.1 – 3 after thermal action (Table 1); here and further the number of curves corresponds to the numbers of series of specimens

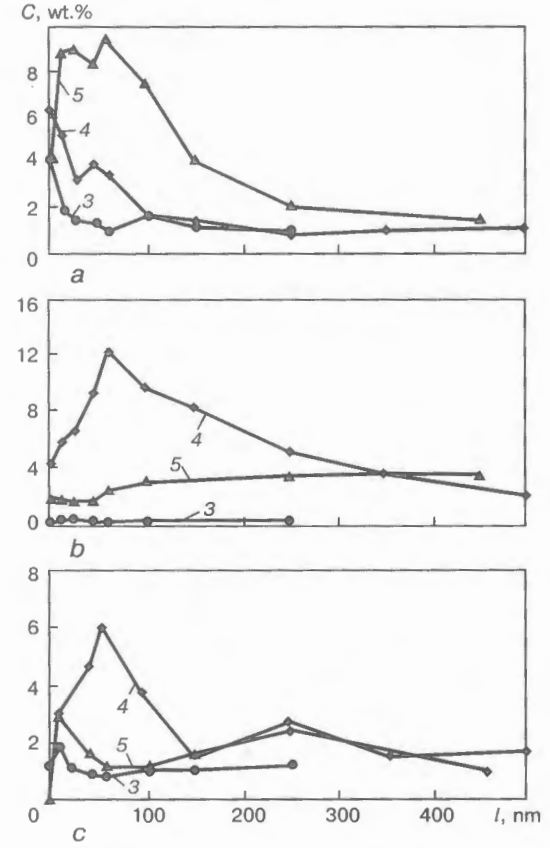

Figure 4. Distribution of oxygen (*a*), sulphur (*b*), manganese (*c*) at the GB and adjacent grain body in near-weld zone metal of specimens of series No.3 – 5 (Table 1) at the pre-fracture stage during DF

formed at the metal surface for 17 h. This time is sufficient for examination. The fracture surface was examined by using the EAS method. The layer-by-layer etching was made by an ion gun CI-40 with ions Ar^+ of energy E = 4 keV and 5 nm/min rate of ion etching.

As a rule, the fracture of the implant samples occurs in the near-weld zone from the artificial notch apex. Therefore, all next investigations were made at this region of the welded joint.

According to the type of action of external factors the test specimens (see Table 1) can be divided into two groups. The first group includes specimens, manufactured from the parent metal (series No.1) and those subjected to the thermal action as a result of annealing (series No.2) and also in the process of welding (series No.3). Here, the surface of fracture of the «freely arranged» metal was investigated. The second group includes the specimens of series No.4 and 5, cut from the implant samples, which were subjected to intensive disturbances, but not to state of the natural fracture (pre-fracture state was studied).

In the specimens of the first group the carbon, phosphorous and chromium are forced out from the GB with manganese and also oxygen and sulphur (Figure 3, *a*, *b*, curve *2*). Here, the significant enrichment of GB with oxygen (≈12 times), sulphur (≈10 times) and manganese to a less extent (≈2 times) occurs as compared with the content of impurities in the body of the initial metal grain. Heating and cooling of metal in the process of welding is performed more intensively than in annealing. Therefore, the thermal cycle of welding leads only to a partial replacement of carbon by oxygen at the GB, to decrease in manganese content on them and to the complete transfer of sulphur into the grain body (Figure 3, *b*, curve *3*).

Complex processes are proceeding near the GB in specimens of the second group (series No.4 and 5), being, respectively, under stress σ_4 and σ_5 which cause the deformation and fracture of metal. In this case a large amount of sulphur and oxygen is accumulated at the near-weld metal GB, and carbon is forced out inside the grain and to the periphery of the specimen (Figures 4 and 5). The zone of enrichment with impurities is rather large, i.e. more than 500 nm. The largest enrichment of the GB and adjacent regions with oxygen is observed in specimens of series No.5. Its content at the GB as compared with that in HAZ metal which was not subjected to loading, increased by 8 times, and in the volume of grain – by 33 times (Figure 4, *a*). The oxygen content increased to a less degree at the GB and in the grain in specimens No.4 – by 4 and 18 times, respectively. At the same time, a mass fraction of sulphur increased greatly in these regions of HAZ metal of specimens (series No.4): by 19.4 times at the GB and by 52 times at the distance l = 60 nm from it (Figure 4, *b*). The enrichment of GB with sulphur in specimens of series No.5 was not

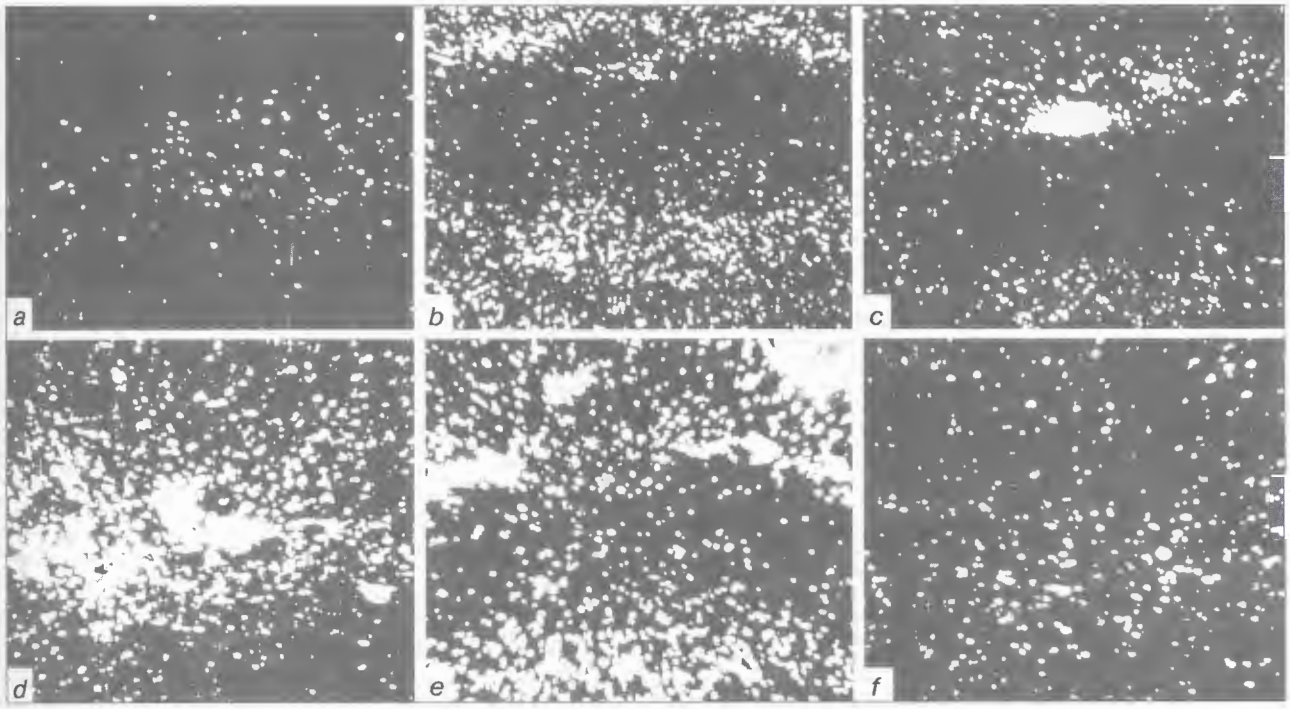

Figure 5. Maps of Auger-distribution of oxygen (*a, b*), sulphur (*c, d*), carbon (*e, f*) in near-weld zone metal of specimens after their loading according to the condition given in Table 1: *a, c, e* — series No.4; *b, d, f* — No.5; GB is located in the frame center horizontally; light spots indicate the presence of element (×200) (reduced by 3/5)

so significant, however, in this case its content is by 8.6 times higher than that in the HAZ initial metal.

The changes in chemical composition of metal at the GB are remarkable at the pre-fracture state for such alloying elements as manganese and chromium. Independently of values of the applied load and time of its action in the specimens of series No.4 and 5 the transfer of these chemical elements from the boundaries into the grain body was observed (Figure 6, *b*, *c*). Here, in specimens of series No.5 and 4 the region of maximum concentration is located at the distance, respectively, $l = 15$ and 60 nm for manganese, 10 and 100 nm for chromium. As compared with the near-weld zone metal the content of manganese in the mentioned zone is increased, respectively, by 6 and 3 times (Figure 4, *c*). For the majority of alloying elements the thickness of the «disturbance» layer of chemical composition is 50 – 100 nm. The less remarkable changes in the chemical composition were observed for other impurity and alloying elements. The peculiarities of distribution of some of them in the near-boundary zone are given in Table 2.

Thus, it was established that at the GB and adjacent regions of near-weld zone metal of the welded joints made from the steel considered the enrichment with impurity and alloying elements occurs mainly under the action of static tensile load. As it causes the deforming and fracture of metal, then this process can be, probably, regarded as a dislocation creep proceeding at room temperature. Two types of creep are distinguished: diffusion (vacancy) creep, proceeding, as a rule, at elevated temperatures and lower loads, and dislocation creep, which is observed at not-high, including room, temperatures under the action of increased loads. It was established that the contribution made by the vacancy creep into the transportation of the impurity and alloying elements is comparable with the contribution of the dislocation creep only at temperatures $T > 0.5T_{melt}$, where T_{melt} is the temperature of melting, and stress $\sigma < 9.6$ MPa [15]. Here, the

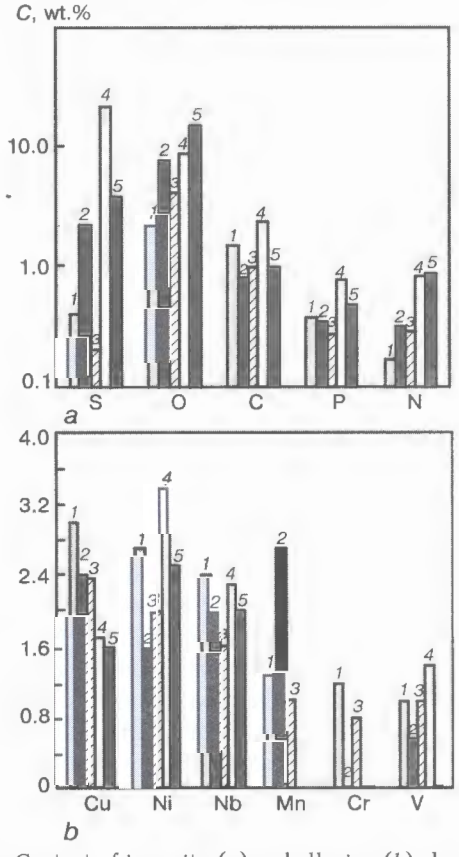

Figure 6. Content of impurity (*a*) and alloying (*b*) chemical elements at GB and near-weld zone of specimens at the pre-fracture stage: *1 – 5* — numbers of specimens from Table 1

Table 2. Effect of load condition at DF on content (wt.%) and distribution of elements from GB into the near-boundary of grain body

l, nm	*C*	*N*	*P*	*Ni*	*Cr*	*Cu*	*Nb*	*V*	*Ca*	*Cl*
				Specimens of series No.3						
0	1.54	0.31	0.27	1.65	1.11	2.38	1.35	1.09	0	0.15
2.5	1.51	0.24	0.40	2.06	0.68	2.84	2.13	1.11	0	0.15
25.0	1.45	0.28	0.48	1.71	1.50	1.82	1.32	0.46	0	0
40.0	1.30	0.32	0.44	2.97	1.33	4.09	2.00	1.01	0.50	0
60.0	1.22	0.25	0.54	2.44	1.11	2.09	2.01	1.27	0.40	0
250.0	1.28	0.28	0.41	2.63	1.19	2.01	1.74	0.43	0.61	0
				Specimens of series No.4						
0	1.23	0.56	0.57	3.44	0	1.70	2.32	1.40	0.59	0
2.50	1.35	0.39	0	2.42	0.69	3.94	1.68	0.82	0	0.15
25.0	0.88	0.24	0.35	2.35	0.94	2.46	1.10	0.61	0.39	0.13
40.0	0.89	0.52	0.36	3.35	0	4.25	2.52	1.01	0.64	0.21
60.0	1.17	0.48	0.54	3.13	1.57	5.33	3.45	1.59	0.37	0
250.0	1.29	0.44	0.49	3.75	1.67	2.21	2.19	0.64	0.21	0
500.0	2.08	0.21	0.24	3.44	1.92	2.37	1.41	1.08	0.33	0
				Specimens of series No.5						
0	1.33	0.54	0.32	2.50	0	1.64	2.03	0	0	0.22
2.5	1.57	0.46	0.34	2.61	0.65	1.58	1.51	0.87	0	0.17
25.0	1.33	0.35	0.59	2.28	0.85	2.28	1.75	1.39	0	0.23
40.0	1.39	0.35	0.49	4.07	1.13	3.17	1.83	1.37	0	0
60.0	1.11	0.37	0.30	2.57	0.47	3.45	2.08	1.25	0.76	0
250.0	1.19	0.19	0.36	2.58	1.33	1.95	1.47	0.95	0.39	0
450.0	1.38	0.38	0.48	2.33	1.18	2.10	1.30	0.78	0.23	0

amount of vacancies in the metal is in the exponential dependence on the temperature. In addition, the dislocations themselves at the elevated temperature become generators of vacancies, while at lower and room temperatures they become sites of their drain [15]. However, in service of the welded structures, the metal of their separate sub-assemblies is in a stressed state during a long time. In this case even at climatic temperatures the processes of vacancy redistribution of impurity and alloying elements can proceed if the metal is subjected to alternating loads.

In the course of present investigations the conditions of loading and heating ($\sigma > 220$ MPa, $T = 20 - 150$ °C) differed greatly from those at which the transfer of impurity and alloying elements occurs by the mechanism of the vacancy creep. Consequently, there are grounds to assume that dislocation creep was observed under the conditions of the experiment, because the diffusion creep has no time (5 – 30 min) to influence significantly the processes of mass transfer and redistribution of chemical elements in metal. In this case the diffusion in metal of almost all chemical elements (except hydrogen) is very small and cannot hinder the process of movement of dislocations as was observed at temperatures 550 – 850 °C [8]. It is known, that in plastically-deformed medium at the temperature below 250 °C almost all mass transfer of oxygen and carbon is realized by a dislocation transport [16]. This occurs in those cases when the rate of deforming does not exceed the critical rate, and the Suzuki atmospheres, appearing around the nuclei of edge dislocations, does not begin to detach from them. But even then the impurity atoms rush the moving dislocation and, having no time to precipitate on it with the formation of the equilibrium atmosphere, they form tails from the atoms of diffusate (impurities) in the region of plane of the dislocation slipping. It is also known that the contribution of the dislocation transport to a total mass transfer in metal deforming is larger with the lower temperature and smaller coefficient of diffusion.

At the same time the atoms of the impurity should have a sufficient mobility not to block its movement in segregating on the slipping dislocation. Consequently, there are all grounds to assume that in case of DF proceeding at room temperatures the decisive role in transportation of the impurity atoms is played by the edge dislocations. Probably, these dislocations, sorbing the impurity atoms, promote their movement from the body to the GB, changing the free energy of the latter.

At a relatively small, but long-term loading (specimens of series No.5) the development of the plastic deformation occurs more intensively than in specimens of the series No.4. It is possible, that this explains the different nature of distribution of sulphur and

oxygen at the same loading and also different degree of sorption of these impurities by the moving dislocations. The sulphur content near the GB is higher in the specimens of series No.4 than in specimens of series No.5 (Figure 6, *a*). This, probably, is due to a different rate of detachment of moving dislocation from the impurity atmospheres of sulphur and oxygen. This is also proved by different nature of distribution of sulphur near GB: in specimens of series No.5 the processes od dislocation transporting of sulphur are clearly developed and in series No.4 the active drain of the condensed atoms of this impurity is observed. Behaviour of oxygen in both cases is adequate.

Almost all the elements have 1 – 2 concentration peaks from the side of the grain body in front of the GB. This can be explained as follows.

First version. The final fracture occurs not accurately along the GB, but along the intergrain layer. Therefore, the maximum of a local concentration of the element, which should correspond to the GB, is located at some distance from the surface of a final fracture. This variant is possible, but then the position of GB for the same region, marked by such peaks, should coincide for different chemical elements, first of all, for oxygen and sulphur. However, the data given in Figures 3, 4 and in Table 2 do not confirm this.

Second version. It is known that during fracture the stresses are relaxed in metal after formation of two new planes, and at the surface itself the compression forces are appeared which are stipulated by the state of energetic non-saturation of the surface atoms. The latter circumstance should lead to some reduction in content of impurities adsorbed by metal earlier during the action of the tensile load. The more intensive the load, leading to the formation of moving dislocations, entrapping and transporting of impurity atoms from the atom depth to their boundaries and shorter the time of this action, the smaller zone of the plastic deforming and higher share of the elastic deformation and so the region of its consequences, i.e. relaxation and desorption associated with it [17, 18]. Therefore at high load and shorter time of its action (specimens of series No.4) the zone of desorption caused by a final fracture will be wider than that in case of use of the lower load and longer time of its action (specimens of series No.5). It is this phenomenon that was stated in the experiment.

Substitutional impurities are reacting on the change in compressive and tensile stresses not so strong as the interstitial impurities. However, even in this case the plastic deformation leads to the redistribution of atoms of such impurities in volume and at the GB (Table 2 and Figure 5, *c*).

There is such a conception in physics of surface as a factor of enrichment (F) which means the ratio of element concentration at the surface of a solid body, grain, phase to its content in volume of this body, grain and phase. Depending on the composition of matrix and the nature of a impurity element this value can vary within the very wide ranges (from units to hundreds of thousands). In the steel investigated in the pre-fracture state the maximum values were observed: F = 1503 for sulphur and 200 for oxygen. It is natural, that this high enrichment of the GB with the mentioned impurities can weaken the interatomic bonds and make metal fracture much easier. This is proved by data given in [11,12]. Thus, M. Seach [11] showed that carbon, molybdenum, boron and niobium promote the increase in strength of adhesion of the GB in iron alloys, and phosphorous, oxygen, sulphur and manganese increase the embrittlement (Figure 7).

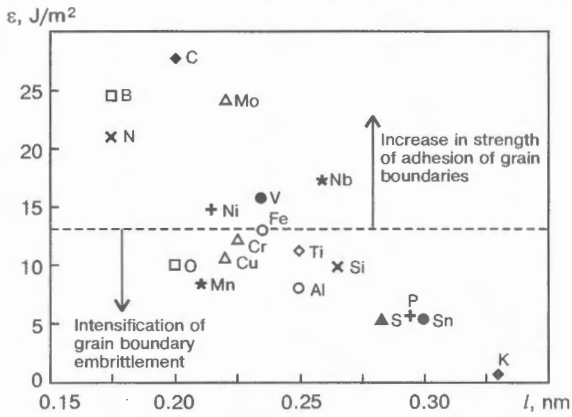

Figure 7. Effect of impurity atoms adsorbed at the GB on the ductility and embrittlement of iron alloys [11]; ε – adhesion strength

There are several models which explain the effect of impurity atoms absorbed at the GB on the nature of the metal fracture [12]. In our opinion, the approach according to which a segregating atom in perfect solutions substitutes for matrix metal, thus changing the metal–metal bond by the weaker metal–segregating atom bond is most acceptable and has a good correlation with a thermodynamic theory [11].

It should be noted that these data are given for the perfect solid solution. However, in the real steel the interaction of separate chemical elements between themselves is possible with a formation of a new phase which can influence the size and number of grains and also the strength properties of metal as a whole (for example, at steel deoxidation with aluminium, titanium and so on). In the given case we mean not the metal as a whole, but the GB, therefore, the formation of different compounds, for example, oxides or hydrides leads, as a rule, to an additional weakening of the intergranular bonds.

Thus, as the investigation showed, an additional cause of embrittlement of welded joints at a delayed fracture of HAZ metal of high-strength alloyed steel of 14KhGN2MDAFB type is, except hydrogen, the process of a dislocation creep leading to the adsorption of several chemical elements, including embrittling, at the GB.

CONCLUSIONS

1. The change in chemical composition of grain boundaries and near-boundary region of grain of the near-weld zone of specimens made from implant sam-

ples of steel 14KhGN2MDAFB in a pre-fracture state at a separate action of thermal and force factors was examined using the electron Auger-spectrometry.

2. Thermal cycle of welding of 14KhGN2MDAFB steel implant samples, not subjected to loading, does not cause a noticeable change in carbon concentration at the GB, but, as compared with the initial metal it leads to the GB enrichment with oxygen and nitrogen.

At different conditions of loading in the process of a delayed fracture the HAZ metal of high-strength steel 14KhGN2MDAFB is subjected to the dislocation creep. Here, a dislocation transport is a main method of a mass transfer of impurity and alloying elements.

3. Change in value and time of action of loading at DF influence the content and distribution of impurity atoms in the GB and in the near-boundary region. The short-time action of the tensile loading of a high level promotes the increase in an elastic component of deformation and initiates the increase in content of sulphur, nitrogen, niobium, nickel and vanadium at the GB. The decrease in the tensile load and increase in time of its action lead to the increase in a plastic component of deformation and significant growth of oxygen content at the GB.

4. At a delayed fracture of welded joints an additional cause of metal embrittlement is, probably, except hydrogen, the process of a dislocation creep, leading to change in chemical composition of microvolumes of metal in the GB zone, their mechanical properties and adsorption of several chemical elements, including embrittling, at the GB.

REFERENCES

1. Makarov, E.L. (1981) *Cold cracks in welding alloyed steels*. Moscow: Mashinostroyeniye.
2. Yakushina, G.M., Makarov, E.L., Ryzhov, N.M. (1973) Relation of cold crack source to the high-strength steel weld metal structure. *Svarochnoye Proizvodstvo*, **5**, 4 – 6.
3. Pokhodnya, I.K., Shvachko, V.I. (1997) Physical nature of hydrogen-induced cold cracks in welded joints of structural steels. *Avtomaticheskaya Svarka*, **5**, 3 – 10.
4. Kasatkin, O.G., Mikhoduj, L.I., Kasatkin, S.B. *et al.* (1995) Resistance of HAZ metal of high-strength steel of 14Kh2GMR type to a delay and brittle fracture. *Ibid.*, **2**, 7 – 10.
5. Kasatkin, B.S., Musiyachenko, V.F. (1974) Mechanism of formation of intercrystalline cracks in near-weld zone of hardening steels. *Problemy Prochnosti*, **10**, 3 ≥ 9.
6. Smiyan, O.D. (1987) Hydrogen and delayed fracture of high-strength steel. *Diagnostika i Prognoz. Razrush. Svarn. Konstr.*, **5**, 29 – 36.
7. Movchan, B.A. (1962) *Microscopic inhomogeneity in cast alloys*. Kyiv: Gostekhizdat Ukr. SSR.
8. Savchenko, V.S., Yushchenko, K.A., Smiyan, O.D. *et al.* (1988) Modelling of conditions of hot crack formation in stable austenitic weld of Fe–Ni alloying system. *Inform. Mater. SEV*, **2**, 1012.
9. Savchenko, V.S., Yushchenko, K.A., Smiyan, O.D. (1988) Peculiarities of segragation of impurity and alloying elements at the grain boundaries of high-alloyed welds and steels of austenitic class. *Avtomaticheskaya Svarka*, **6**, 19 – 23.
10. Smiyan, O.D., Grigorenko, G.M., Mikhajlovskaya, E.S. *et al.* (1966) Features of chemical elements migration in the near-surface layers of metals and alloys during thermal cycling. In: *Proc. of SPIE on Space Mater.*, 4 – 5 Aug., Denver, USA.
11. Seach, M.P. (1983) Auger-spectroscopy in metallurgy. In: *Practical surface analysis by Auger- and X-ray photoelectron spectrometry*. N.Y.: Wilbey&Sons.
12. Poletika, I.M. (1988) *Intercrystalline adsorption of impurities and fracture of metals*. Novosibirsk: Nauka.
13. Degtyarev, V.N., Orlov, M.R. (1987) Study of fracture of high-speed steel R6AM5F3 using Auger-spectroscopy. *Fizika Metallov i Mettalloved.*, **3**, 565 – 571.
14. Musiyachenko, V.F., Mikhoduj, L.I., Zhdanov, S.L. *et al.* (1985) Structural transformations in steel 14KhGNMD and properties of welded joints. *Avtomaticheskaya Svarka*, **4**, 10 – 14, 18.
15. Rozenberg, V.M. (1967) *Creep of metals*. Moscow: Metallurgia.
16. Zharinov, V.P., Zotov, V.S., Pavlychev, A.N. (1988) Account for increase in dislocations in diffusion in plastically-deforming medium. *Fizika Metallov i Mettalloved.*, **2**, 230 – 233.
17. Smiyan, O.D. (1980) Distribution of hydrogen in the zone of deformation cracks. *Zhurnal Fiz. Khimii*, **11**, 2913 – 2917.
18. Smiyan, O.D., Grigorenko, G.M., Vajnman, A.B. (1999) Effect of different kinds of cycling on behaviour of hydrogen in metals. *Mashinoznavstvo*, **5**, 4 – 9.

DETERMINISTIC-STATISTICAL MODEL OF WELD SHAPE IN ARC WELDING

I.F. KORINETS and **JI CHENG CHUN**
NTUU «Kyiv Polytechnic Institute», Kyiv, Ukraine

ABSTRACT

The paper gives theoretical substantiation of the rationality of construction of deterministic-statistical models in the form of a product of exponential functions. The adequacy of the constructed mathematical models, combining the advantages of deterministic (representation of physical processes and versatility) and statistical (simplicity and high accuracy) models, was checked for the case of CO_2 arc welding. Model applications are described.

Key words: *arc welding, mathematical simulation, weld shape, weld dimensions, deterministic model, statistical model*

Arc welding, despite its complexity, is a predominant process in welding fabrication. This welding process is the subject of many systems of CAD for design of welded joints and technologies, and CAM for controlling the technological processes and robotic work stations, diagnostics of quality, for research and training. This sphere of activity is unthinkable without applying computer systems and the appropriate software and hardware [1]. Therefore, the need for mathematical simulation grows steadily.

Experience of simulating various arc welding processes, in particular weld formation, has been gained by now, as indicated by numerous publications. So this study is aimed at selection of a prototype of the model of weld shape for arc welding, that furtheron could be used in the system of technological adaptation of the robot. This model should be simple, so as to support the control system operation in real time, and also sufficiently sensitive to technological disturbances (gap deviation and edge geometry, edge deformation during welding, etc.).

Analysis of weld formation models. The final result of the arc welding process is the weld, its quality depending primarily on the shape (shape ratios of penetration ψ_p and bead ψ_b) and dimensions of its cross-section (depth h and width e of penetration, bead height g) (Figure 1). The model should correlate these weld parameters with the arc welding mode (electrode diameter d, welding current I, arc voltage U, welding speed v and wire melting rate v_m, etc.).

All the mathematical descriptions are divided into two kinds, namely deterministic and statistical [2]. The most versatile is the deterministic description, that is based on fundamental laws.

A widely accepted deterministic model of penetration of the metal being welded (N.N. Rykalin) was developed on the basis of the theory of thermal processes of welding [3]. It allows calculation of the penetration area and ensures satisfactory accuracy with correction factors [4]. However, the penetration shape and dimensions according to this model, do not correspond to the actual process, and the calculation provides poor accuracy.

The non-linear nature of heat conduction process and the dependence of the metal properties on temperature, do not always permit simple analytical solutions to be obtained. Modern computer systems, however, allow more accurate computation of weld shape to be performed, using complex deterministic mathematical models, that are based on a system of differential equations and are solved by the numerical methods [5, 6]. Interrelation of the concurrent processes of different physical nature in arc welding, makes the researchers separate the model into a number of partial models and solve simpler problems.

Study [7] presents a deterministic model of formation of the crater surface and the weld in arc welding, constructed on the basis of a balance of forces of surface tension, gravity and mechanical pressure of the arc. However, the main parameters of the weld, (h, e, g) are not determined, but are the input parameters of this model.

Works [8, 9] suggest a relatively simple deterministic model of weld formation in CO_2 arc welding, that allows for the balance of forces of arc pressure and metal-static pressure of liquid metal of the pool, and the penetration area is determined on the basis of the above-mentioned study [3]. This model provides a dependence of weld dimensions not on the individual welding parameters, but on an integrated parameter, namely the welding heat input

$$q_h = IU/v. \quad (1)$$

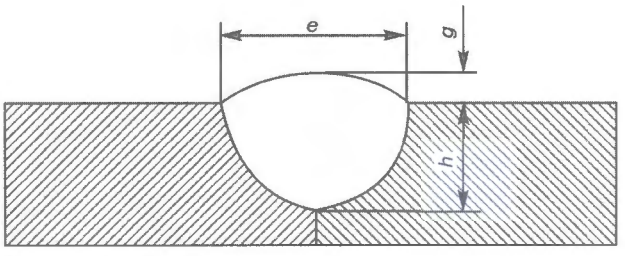

Figure 1. Butt weld parameters

It is known [4] that at the same heat input, weld dimensions can vary considerably. Therefore, it does not seem possible to obtain a highly accurate estimate of the significance of the individual welding parameters from this model. A good correlation of the design and experimental data is found in a narrow range of welding speeds.

When more complex deterministic models are used, the better and more accurately are the input parameters taken into account, the longer is the computing time, required for weld shape calculation and its optimisation, thus limiting their application in adaptive systems of arc welding control.

Statistical models of weld shape, systematised in [10], have become widely accepted over the last years. These models cover all the major welding processes, namely coated electrode [11], submerged-arc welding and surfacing [12 – 16], gas-shielded consumable [17 – 19] and non-consumable [20, 21] arc welding with electrodes of various steels and alloys. These models use mathematical dependencies in the form of polynomials [11, 13 – 15, 17 – 19], product of exponents [12, 20, 21] and of a mixed kind [16]. Statistical models are comparatively simple and have a sufficient accuracy. However, their application is restricted by the limits of the parameters, varied in the model. In addition, they have an implicit deterministic dependence between the input, control and output parameters.

Mixed deterministic-statistical models are also finding an application [22 – 25]. In the mathematical description of [22] prevalent is an empirical approach, using equations in the form of a product of exponential functions. It, however, lacks a theoretical substantiation of the derived system of equations.

The known model [23, 24], allowing calculation of the mode and dimensions of a weld in automatic submerged-arc welding, is based on the earlier mentioned dependence of penetration area on welding heat input [3]. V.I. Dyatlov suggested representing the penetration shape as a semi-ellipse, with an area equivalent to the theoretically found area of a semicircle, while the penetration shape ratio is chosen from experimental data [22]. These data were further used to derive an equation for calculation of the penetration shape ratio [24]. This deterministic-statistical model allows weld dimensions and welding mode to be calculated in an iteration mode.

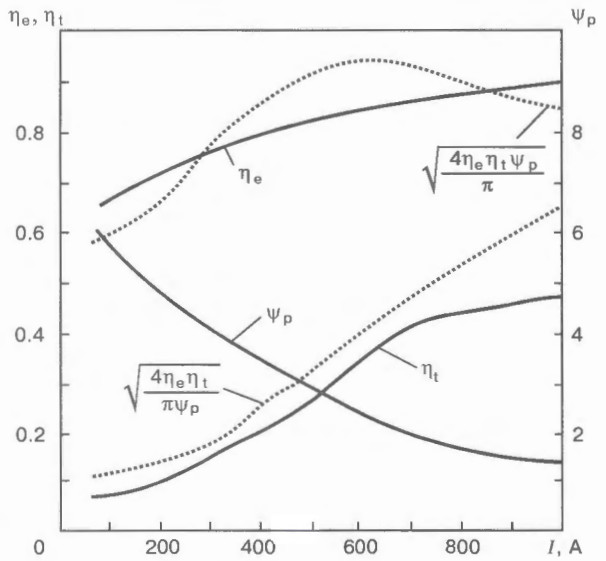

Figure 2. Evaluation of the influence of welding current on the complex index of η_e, η_t and ψ_p characteristics

Development of a deterministic-statistical model. The above analysis indicates, that in order to solve the problem posed in the study, it is rational to select a method of deterministic-statistical simulation and develop a model, combining the advantages of deterministic (representation of the physical processes and versatility) and statistical (simplicity and high accuracy) models.

It is obvious that any deterministic model of a weld in fusion welding, should primarily allow for the dependence of penetration on the energy input parameters, i.e. for arc welding these are I, U and v. In the further derived dependencies of depth h and width e of penetration on the main parameters of arc welding I, U and v, let us single out, as individual multipliers, the physical properties (first multiplier), efficiency with the penetration shape ratio (second multiplier) and welding mode parameters (third multiplier):

$$h = \sqrt{\frac{1}{c_p\rho T_m}}\sqrt{\frac{\eta_e\eta_t}{(\pi/4)\psi_p}}\sqrt{\frac{IU}{v}}, \quad (2)$$

$$e = \sqrt{\frac{1}{c_p\rho T_m}}\sqrt{\frac{\eta_e\eta_t\psi_p}{\pi/4}}\sqrt{\frac{IU}{v}}, \quad (3)$$

where c_p, ρ, T_m are the specific heat, density and melting temperature of the metal being welded; η_e, η_t are the effective and thermal efficiency, respectively; ψ_p is the penetration shape ratio, equal to e/h.

In expressions (2) and (3) h and e are not assigned explicitly, as they are incorporated in ψ_p. Furthermore, η_e and η_t essentially depend on the welding mode. Therefore, in such a form, these expressions are unfit for practical application. If the specific heat is assumed to be constant and equal to the mean value in the temperature range T_0–T_m, the first multiplier can be taken to be constant.

Characteristics, included into the first multiplier, depend in a different way on the welding mode. The penetration shape ratio ψ_p and effective efficiency η_e depend less on welding speed v. Optimal welding voltage U in arc welding usually increases in proportion to the rise of welding current I, and its value varies in narrow ranges. Therefore, it is rational to consider the second multiplier as a function of welding current (Figure 2). The nature of this multiplier dependence on current is different in (2) and (3). So, the second multiplier in expression (2) grows monotonically with the increase of current, while in expression (3) it is a curve with a maximum. Therefore, different shapes of dependence (3) are anticipated at current variation in a broad range. Indeed, based on experimental data, obtained in

Table 1. Range of CO_2 arc welding modes

Welding parameters	Electrode wire diameter, d, mm			
	1.2	1.4	1.6	2.0
Welding current, I, A	100 – 350	150 – 350	140 – 410	180 – 465
Welding voltage, U, V	20 – 33	22 – 35	20 – 35	21 – 38
Welding speed, v, mm/s	4.4 – 14.9	4.4 – 14.9	4.4 – 22.9	4.4 – 14.9

CO_2 arc welding [25], the dependence of weld width on current has a maximum.

This analysis gives grounds to present the second multiplier as a function of welding current and the expressions for penetration depth and width, on the whole, as products of exponential functions [26]:

$$h = K_h \frac{I^a U^b}{v^c}, \quad (4)$$

$$e = K_e \frac{I^m U^n}{v^k}. \quad (5)$$

In this connection, a considerable increase of the exponent of welding current in expression (4) is anticipated, compared to the theoretical value, i.e. $a > 0.5$. The model can be simplified further, if voltage is expressed through welding current:

$$U = K_U I^0 \quad (6)$$

and excluded from (4) and (5). Then, the expressions for calculation of weld dimensions, have the following form [26]:

$$h = K_h \frac{I^p}{v^q}, \quad (7)$$

$$e = K_e \frac{I^s}{v^t}. \quad (8)$$

In welding butt joints without a gap, the height of bead reinforcement can be determined, using the bead fullness coefficient μ_b [24]:

$$g = F_d / \mu_b e. \quad (9)$$

Let us determine the deposited metal area from the balance of the molten and deposited metal:

$$F_d = F_w v_f (1 - \psi_{sp})/v, \quad (10)$$

where F_d, F_w are the cross-sectional areas of the deposited bead and wire; v_f is the wire feed rate; ψ_{sp} – is the coefficient of spatter.

Substituting into expression (9) the values of penetration width e (3), deposited metal area F_d (10) and wire melting rate v_m [27], we get the dependence of g on the welding mode parameters.

$$g = \frac{K_1 I^{0.5} + K_2 I^{1.5}/d}{v^{0.5} U^{0.5}}, \quad (11)$$

where the constant values are combined in coefficients K_1 and K_2.

Simplifying the polynomial in the numerator of expression (11), and substituting it in the form of an exponential function of current, we have the expression to determine the weld convexity

$$g = K_g \frac{I^r}{v^w U^v} \quad (12)$$

or

$$g = K_g \frac{I^i}{v}. \quad (13)$$

Exponents r, w, u, i, j should be determined more precisely by experimental data.

The penetration shape ratio ψ_p can be presented as the ratio of expressions (4) and (5), (7) and (8), or it can be determined directly as a result of statistical processing of the experimental data:

$$\psi_p = K_\psi \frac{U^x}{I^y} v^z, \quad (14)$$

$$\psi_p = K_\psi \frac{v^l}{I^f}. \quad (15)$$

Verification of the model adequacy. The adequacy of the developed simulation procedure has been verified in CO_2 consumable-arc welding. Table 1 gives the range of welding parameters. Welding (surfacing) was performed with Sv-08G2S (C – 0.11; Si – 0.5; Mn – 1.4; Cr – up to 0.1 wt.%) wire on VSt.3 killed steel plates (C – 0.14 – 0.22; Cr – up to 0.3; Si – 0.12 – 0.3; Mn – 0.4 – 0.65; Ni – up to 0.3; Cu – up to 0.3; S – up to 0.05; P – up to 0.4; As – up to 0.08 wt.%) 10 mm thick in ADG-602 automatic machine, using VDU-601 power source.

Table 2 gives the data on the modes of welding with 1.6 mm diameter wire, experimental, as well as design parameters of welds, derived from models M1, M2 and M3 (Table 3) after statistical processing of experimental data by the regression analysis method.

The best agreement of the experimental and design weld dimensions is provided by all the models across the penetration depth. Mean value of relative error does not exceed 10 % (Table 4).

Deviations by weld width in different models are greater, than those by penetration depth. A satisfactory accuracy is provided by model M2 (10.0 %), covering the three main welding parameters (I, U, v), as well as model M3 (10.4%), allowing for two mode parameters (U, v), that have the strongest influence on weld width. If a model does not allow for

Table 2. Comparison of experimental and design dimensions of the weld

N	Welding mode			Weld					
	I, A	U, V	v, mm/s	h				e	
				exp.	des. M1	des. M2	des. M3	exp.	des. M1
1	150	20.2	6.4	2.0	1.8	1.8	1.8	6.5	5.9
2	152	25.7	4.4	2.0	1.9	1.9	2.0	11.8	11.6
3	140	25.8	6.4	2.0	1.5	1.5	1.6	6.5	8.4
4	210	20.5	4.4	2.8	3.2	3.2	3.1	8.1	9.1
5	210	20.5	6.4	2.5	2.9	2.9	2.7	6.2	6.7
6	205	23.0	4.4	3.0	3.0	3.0	3.0	10.4	10.7
7	204	23.0	6.4	2.6	2.7	2.6	2.6	7.6	7.9
8	220	28.1	4.4	2.2	3.1	3.1	3.3	16.1	14.8
9	218	28.2	6.4	3.4	2.8	2.7	2.8	10.0	11.0
10	197	28.6	10.7	1.6	2.1	2.0	2.1	7.9	7.2
11	250	22.0	4.4	4.6	4.0	4.1	3.8	7.1	10.6
12	255	21.7	6.4	3.5	3.7	3.7	3.5	6.4	7.7
13	255	25.6	4.4	3.9	4.0	4.0	3.9	10.5	13.4
14	255	25.6	6.4	3.3	3.6	3.5	3.5	8.3	9.9
15	270	28.0	4.4	4.6	4.2	4.2	4.2	15.1	15.7
16	260	29.0	6.4	3.6	3.5	3.5	3.6	12.2	12.0
17	255	30.0	10.7	2.5	2.9	2.8	2.9	8.4	8.3
18	230	30.3	14.9	2.2	2.3	2.2	2.3	6.7	6.3
19	294	26.4	6.4	4.3	4.3	4.3	4.2	8.5	10.8
20	292	26.3	10.7	3.6	3.7	3.6	3.5	7.0	7.1
21	338	30.3	4.4	5.5	5.7	5.6	5.7	20.0	18.9
22	330	30.4	6.4	5.3	4.9	4.8	4.8	11.7	13.9
23	328	30.4	10.7	4.4	4.2	4.0	4.0	8.0	9.1
24	300	30.8	14.9	3.1	3.3	3.2	3.2	7.0	6.9
25	250	31.5	22.9	2.2	2.3	2.1	2.2	6.3	4.8
26	355	28.9	14.9	4.4	4.3	4.1	4.0	7.7	6.6
27	302	29.1	22.9	2.6	3.0	2.8	2.8	6.2	4.5
28	390	33.8	4.4	6.5	6.7	6.7	6.8	23.4	23.2
29	410	33.6	6.4	6.2	6.5	6.4	6.4	14.0	17.2
30	390	33.8	10.7	5.4	5.2	5.0	5.0	11.4	11.3
31	380	33.9	14.9	4.1	4.6	4.3	4.3	9.0	8.6
32	325	34.7	22.9	2.7	3.2	3.0	3.1	7.2	6.0

welding voltage, the error rises up to 20.5 %. In individual experiments the error across the weld width is essentially higher, than the mean values, this being due to formation of rolls or undercuts in welding at high currents at low or high welding speeds. In such cases difficulties were encountered in determination of the penetration boundary in the weld upper part and measurement of weld width. In addition, as noted earlier, the dependence of weld width on current, has a maximum, thus lowering the accuracy of the model, which is a monotonic function. Model M3 with a selective combination of two significant parameters I, U, v also provides satisfactory accuracy.

Analysis of the derived models in the form of exponential expressions (Table 3) shows that they quantitatively and qualitatively represent deterministic dependencies of weld dimensions on the main parameters of arc welding. Note the ambiguous influence of arc voltage on penetration depth (see Table 3, model M2). It is obvious that in case of CO_2 arc welding with thin wire ($d \le 1.2$ mm) electrode metal transfer proceeds through short-circuiting at a short arc, and the influence of voltage on penetration depth is determined by its energy input (voltage is in the numerator of the fraction), this corresponding to the initial theoretical prerequisite (2). In welding with wires of larger diameters ($d \ge 1.4$ mm) at higher current and voltage, electrode metal transfer proceeds, as a rule, without short-circuiting with a long arc, thus increasing the amplitude of the arc erratic oscillations, lowering the density of the applied energy and decreasing the penetration depth, respectively (voltage is in the denominator of the fraction).

Comparison of the exponents of welding parameters (I, U, v) in the theoretically derived expressions (2) and (3) with the exponents (see Table 3, model M2) after statistical processing of experimental data, reveals a significant difference, this being related to the assumed idealisation of penetration [3]. The closest to the theoretical value (0.5) are the exponents of welding speed in the equations for h (0.22 – 0.34) and e (0.74 – 0.88), this being attributable to the influence of welding speed on weld dimensions, as a mechanical parameter. The situation is different with

dimensions, mm			Penetration shape ratio						
			g				Ψ_p		
des. M2	des. M3	exp.	des. M1	des. M2	des. M3	exp.	des. M1	des. M2	des. M3
5.3	5.3	2.3	2.4	2.5	2.4	3.3	3.1	3.0	3.1
11.8	12.1	2.5	2.1	2.1	2.9	5.9	5.7	6.4	6.2
8.8	9.1	1.6	1.7	1.6	2.3	3.3	5.1	6.1	5.9
7.4	7.3	4.1	4.1	4.3	3.5	2.9	2.6	2.3	2.5
5.6	5.5	3.1	3.5	3.7	2.9	2.5	2.2	2.0	2.1
9.5	9.4	3.5	3.4	3.6	3.5	3.5	3.3	3.2	3.3
7.1	7.1	2.7	2.9	3.0	2.8	2.9	2.8	2.7	2.8
14.6	14.8	3.3	2.9	2.9	3.6	7.3	4.4	4.8	4.7
11.0	11.2	2.3	2.5	2.4	2.9	2.9	3.7	4.1	4.1
7.6	7.7	1.7	1.7	1.7	2.1	4.9	3.2	3.9	3.9
8.7	8.5	4.8	4.5	4.8	3.9	1.5	2.5	2.2	2.3
6.4	6.2	4.8	4.1	4.3	3.2	1.8	1.9	1.7	1.9
12.1	12.0	4.2	3.8	4.0	3.9	2.7	3.2	3.1	3.2
9.0	9.0	3.6	3.3	3.4	3.2	2.5	2.6	2.6	2.7
14.7	14.7	3.0	3.7	3.8	4.1	3.3	3.5	3.5	3.6
11.8	11.9	2.4	2.9	2.9	3.3	3.4	3.2	3.5	3.5
8.5	8.6	1.5	2.2	2.1	2.4	3.4	2.6	3.1	3.1
6.7	6.8	1.7	1.7	1.6	1.9	3.0	2.5	3.1	3.1
9.8	9.6	4.8	3.7	3.8	3.5	2.0	2.3	2.3	2.4
6.5	6.4	3.8	3.0	3.0	2.6	1.9	1.8	1.8	1.9
17.6	17.5	4.6	4.3	4.4	4.6	3.6	3.1	3.2	3.2
13.3	13.2	3.9	3.6	3.6	3.7	2.2	2.6	2.8	2.8
8.9	8.9	2.9	2.9	2.8	2.8	1.8	2.0	2.2	2.3
7.1	7.1	2.5	2.3	2.2	2.2	2.3	1.9	2.3	2.3
5.3	5.3	2.3	1.5	1.4	1.6	2.9	2.0	2.5	2.5
6.3	6.1	2.4	3.0	2.9	2.5	1.8	1.4	1.5	1.6
4.5	4.5	1.8	2.1	2.0	1.8	2.4	1.4	1.6	1.7
22.4	22.4	5.0	4.4	4.5	5.0	3.6	3.2	3.4	3.4
16.7	16.5	3.2	4.0	4.1	4.2	2.3	2.5	2.6	2.7
11.3	11.3	2.6	3.1	3.0	3.1	2.1	2.0	2.3	2.3
8.8	8.8	2.1	2.6	2.5	2.6	2.2	1.8	2.1	2.1
6.6	6.6	2.0	1.8	1.7	1.9	2.7	1.7	2.2	2.3

Table 3. Weld shape models

Model	Electrode wire diameter, d, mm			
	1.2	1.4	1.6	2.0
M1	$h = 0.007 \frac{I^{1.415}}{d^{0.337} U^{0.262} v^{0.289}}$	$e = 0.063 \frac{d^{0.020} I^{0.297} U^{1.513}}{v^{0.812}}$	$g = 0.954 \frac{I^{1.141}}{d^{0.593} U^{1.251} v^{0.399}}$	$\Psi_p = 9.0 \frac{d^{0.357} U^{1.775}}{I^{1.118} v^{0.523}}$
M2	$h = 0.002 \frac{I^{1.389} U^{0.172}}{v^{0.340}}$	$h = 0.010 \frac{I^{1.539}}{U^{0.684} v^{0.219}}$	$h = 0.006 \frac{I^{1.455}}{U^{0.340} v^{0.325}}$	$h = 0.007 \frac{I^{1.444}}{U^{0.339} v^{0.342}}$
	$e = 0.054 \frac{I^{0.460} U^{1.254}}{v^{0.741}}$	$e = 0.055 \frac{I^{0.408} U^{1.406}}{v^{0.858}}$	$e = 0.026 \frac{I^{0.066} U^{2.131}}{v^{0.768}}$	$e = 0.313 \frac{I^{0.082} U^{1.453}}{v^{0.886}}$
	$g = 0.290 \frac{I^{1.254}}{U^{1.109} v^{0.392}}$	$g = 1.253 \frac{I^{1.098}}{U^{1.323} v^{0.410}}$	$g = 1.024 \frac{I^{1.193}}{U^{1.415} v^{0.441}}$	$g = 0.609 \frac{I^{0.792}}{U^{0.649} v^{0.401}}$
M3	$h = 0.201 \frac{I^{0.556}}{v^{0.198}}$	$h = 0.006 \frac{I^{1.249}}{v^{0.258}}$	$h = 0.005 \frac{I^{1.288}}{v^{0.342}}$	$h = 0.005 \frac{I^{1.308}}{v^{0.398}}$
	$e = 0.058 \frac{U^{1.938}}{v^{0.655}}$	$e = 0.146 \frac{U^{1.804}}{v^{0.877}}$	$e = 0.026 \frac{U^{2.245}}{v^{0.772}}$	$e = 0.354 \frac{U^{1.554}}{V^{0.889}}$
	$g = 0.089 \frac{I^{0.817}}{v^{0.431}}$	$g = 0.341 \frac{I^{0.573}}{v^{0.492}}$	$g = 0.391 \frac{I^{0.559}}{v^{0.535}}$	$g = 0.410 \frac{I^{0.499}}{v^{0.469}}$

Table 4. Relative error, %, of weld shape models in CO_2 arc welding with 1.6 mm wire

Model	Weld dimensions, mm			ψ_p
	h	*e*	*g*	
M1	9.9	12.6	13.5	18.7
M2	8.7	10.0	13.2	16.8
M3	8.8	10.4	17.4	16.2

respect to welding current and voltage. In the equation for *h* calculation, the exponent is much higher, than the theoretical value (0.5), and is equal to 1.4 – 1.5, this being indicative of a high significance of this parameter. The equation for *e* calculation demonstrates, that in terms of weld width, voltage with 1.3 – 2.0 exponent is a more significant parameter.

Analysis of the models shows that they do not contradict the existing concepts. Combining the welding parameters in the models and varying the coefficients, it is possible to derive dependencies, giving the most accurate representation of the essence of physical processes with satisfactory accuracy.

The simulation method can find application when studying the influence of the process parameters (material composition, type of joint and weld, welding position, accuracy of assembly, etc.) on the weld shape in arc welding.

Such models can be used in development of systems of automated control of the arc welding process, procedures of design and optimisation of the welding mode parameters, systems of automated training, CAM modules, technologist workstations and expert systems.

CONCLUSIONS

1. The known theory of thermal processes of welding was used as a basis to demonstrate the rationality of representing a mathematical model of weld shape in arc welding as a product of exponential functions.

2. The simulation procedure incorporates deterministic dependencies between the weld shape and dimensions and the main parameters of arc welding mode.

3. Comparison between the experimental and design weld dimensions for the case of CO_2 consumable-arc welding (surfacing) demonstrated a satisfactory level of adequacy of the developed models. Relative error by the main weld parameters does not exceed 10 – 15 %.

4. The models can be used for further studies of the process of penetration and weld formation in arc welding. The model simplicity (two control parameters) and satisfactory accuracy allow them to be used in the automatic control systems with technological adaptation.

REFERENCES

1. Makhnenko, V.I. (1986) Mathematical methods and scientific-technical progress in welding production. In: *Mathematical methods in welding*. Kyiv: PWI.
2. Skurykhin, V.I., Shafran, V.B., Dubrovsky, V.V. (1983) *Mathematical modelling*. Kyiv: Tekhnika.
3. Rykalin, N.N. (1951) *Calculation of thermal processes in welding*. Moscow: Mashgiz.
4. Erokhin, A.A. (1973) *Principles of fusion welding. Physico-chemical laws*. Moscow: Mashinostroyeniye.
5. Sudnik, V.A. (1986) Mathematical methods of deterministic evaluation of welded joint formation. In: *Mathematical methods in welding*. Kyiv: PWI.
6. Denisov, V.M., Nesterov, A.F., Sudnik, V.A. *et al.* (1994) Mathematical modelling of weld formation in argon-arc welding of butt joints of sheet fiber-reinforced composite material of aluminium–boron system. *Svarochnoye Proizvodstvo*, **11**, 14 – 17.
7. Berezovsky, V.M. (1986) Mathematical modelling of weld formation in arc welding in different spatial positions. In: *Mathematical methods in welding*. Kyiv: PWI.
8. Popkov, A.M. (1986) Calculation of weld parameters in CO_2 welding of square-butt joints. *Svarochnoye Proizvodstvo*, **9**, 21 – 22.
9. Popkov, A.M., Khudyakov, V.I. (1988) Calculation of fillet weld parameters in CO_2 welding. *Ibid.*, **10**, 21 – 22.
10. Lebedev, B.D., Peremitko, V.V. (1998) *Calculation methods in fusion welding*. Dneprodzerzhinsk: DGTU.
11. Dudko, D.A., Zatserkovny, S.A., Sidoruk, V.S. *et al.* (1987) Influence of parameters of the mode of manual arc welding at modulated current on weld shape. *Avtomaticheskaya Svarka*, **6**, 19 – 22.
12. Turyk, E., Lyasovsky, E. (1981) Development of a mathematical model for determination of the geometry of a layer deposited by submerged-arc welding. In: *Mathematical methods in welding*. Kyiv: Naukova Dumka.
13. Korenyuk, Yu.M., Mishina, L.N. (1989) Optimization of the mode of submerged-arc welding of 70 mm thick aluminium. *Svarochnoye Proizvodstvo*, **7**, 16 – 17.
14. Varenchuk, P.A., Privalov, N.T., Galinich, V.I. *et al.* (1991) Influence of overhead submerged-arc welding parameters on weld shape and dimensions. *Avtomaticheskaya Svarka*, **3**, 38 – 41.
15. Ryzhov, F.N., Vu Guy Lan (1994) Optimization of restoration technology for cranckshafts made of hardening steels. *Svarochnoye Proizvodstvo*, **1**, 4 – 6.
16. Vasiliev, N.G. (1994) Optimisation of the technology of hardfacing worn parts. *Ibid.*, **7**, 4 – 7.
17. Dubovetsky, S.V., Sergatsky, G.I., Kasatkin, O.G. (1980) Optimization of CO_2 welding mode. *Avtomaticheskaya Svarka*, **12**, 30 – 34.
18. Dubovetsky, S.V., Sergatsky, G.I., Kasatkin, O.G. (1982) Optimization of the mode of CO_2 welding of fillet welds in different spatial positions. *Ibid.*, **5**, 34 – 38.
19. Dubovetsky, S.V., Kasatkin, O.G. (1986) Optimization of welding mode, using regression models of weld formation. In: *Mathematical methods in welding*. Kyiv: PWI.
20. Nerodenko, M.M., Kovalenko, R.I., Vasilenko, T.N. (1979) Calculation of pool parameters in automatic helium-arc welding of sheet niobium and molybdenum alloys. *Avtomaticheskaya Svarka*, **12**, 13 – 15.
21. Nerodenko, M.M., Demchenko, A.D., Kundik, V.V. (1982) Calculation of pool geometry in mechanised arc welding of vanadium and tungsten alloy sheets. *Ibid.*, **6**, 17 – 20.
22. Babkin, A.S., Krivosheya, V.E. (1985) Development of an algorithm for calculation of CO_2 welding mode parameters, using a micro-computer. *Svarochnoye Proizvodstvo*, **4**, 3 – 5.
23. Dyatlov, V.I. (1959) *Calculation of automatic welding modes*. Kyiv: KPI.
24. Akulov, A.I., Belchuk, G.A., Demyantsevich, V.P. (1977) *Technology and equipment of fusion welding*. Manual. Moscow: Mashinostroyeniye.
25. Potapievsky, A.G. (1974) *Gas-shielded metal-arc welding*. Moscow: Mashinostroyeniye.
26. Korinets, I.F. (1988) Development of engineering methods for calculation of the arc welding mode. In: *Application of mathematical methods in welding*. Kyiv: PWI.
27. Korinets, I.F. (1995) Mathematical model of electrode wire melting in arc welding. *Avtomaticheskaya Svarka*, **10**, 39 – 43.

STATIC AND DYNAMIC VOLT-AMPERE CHARACTERISTICS OF TUNGSTEN–ALUMINIUM ARC OF SQUARE ALTERNATING CURRENT

V.A. KOSOVICH, I.E. LAPIN, A.N. POTAPOV, A.V. SAVINOV and **V.I. LYSAK**
Volgograd State Technical University, Volgograd, Russia

ABSTRACT

Dependence of the arc gap voltage in pulses of current at straight (SP) and reverse polarity (RP) and also effective values of voltage on current and duration of current pulses at reverse polarity is considered. The decrease in voltage in pulses of current at straight polarity down to anomalously low values at increase in duration of current pulses at reverse polarity is outlined.

Key words: *volt-ampere characteristics, non-consumable electrode, argon arc welding, AC arc, square shape voltage*

Recently, the AC arc power sources, in which the voltage at the output terminals is changed along the square curve, have been developed and find application. If in this case the inductance of the welding circuit is close to zero, then the power source operates at active load, i.e. at arc, and the arc current is changed by the same law (curve of changing pulses has a square shape). The use of these power sources widens the technological feasibility of the argon arc welding of aluminium alloys, making it possible to adjust separately the frequency and duration of current pulses at straight and reverse polarity and also their amplitude. It should be noted that the term «pulses» instead of a traditional «half-cycles» is used here due to possible inequality in their durations.

Based on the investigations of the arc supplied from such power sources, the data were obtained about its power and technological properties [1 – 4] which prove the prospects of application of square alternating current in welding aluminium alloys. However, to realize this it is necessary to investigate arc to clarify its technological features and electrical properties and, first of all, the volt-ampere characteristics. Data about the latter are required for the effective use of this arc for welding, as the use of the known method of estimation of the power parameters of the arc at changing current close to sinusoidal in the case considered is hardly possible.

The present work presents the results of investigation of the volt-ampere characteristics of the square AC arc.

As a non-consumable electrode, the lanthanized tungsten rods, whose working edge was sharpened for a hemisphere, were used. Plates from alloy AMg5, moved under the fastened torch at 12 m/h rate were the second electrode. The set length of the interelectrode gap was 2 mm. During experiments the power source developed by the authors was used. This power source consisted of a single-phase thyristor bridge inverter of voltage with a forced parallel commutation and also main and auxiliary adjustable DC power sources. The power source is capable to change the ratio of amplitudes of current pulses within the range of 0.25 – 40.00 and separate adjustment of current pulse duration from 2 to 20 ms at straight τ_{SP} and reverse τ_{RP} polarity. Here, the stable arc burning without use of a pulsed stabilizer is provided within the 6 – 350 A current range. The argon consumption was 8 l/min. The current, arc voltage, duration of current pulses were measured and controlled using double-beam memory oscillograph S8-14. Oscillograms of current and voltage of the arc considered are given in Figure 1.

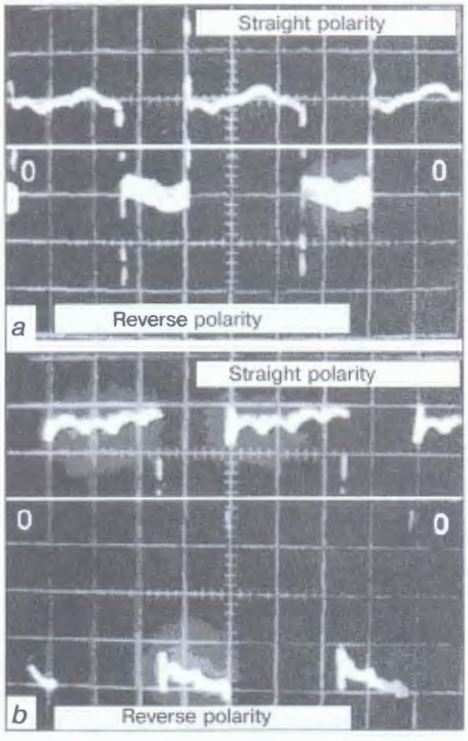

Figure 1. Oscillograms of current (*a*) and arc voltage (*b*) at I_a = = 200 A, τ_{SP} = 12.5 and τ_{RP} = 7.5 ms (scale in voltage is 5 V/div.)

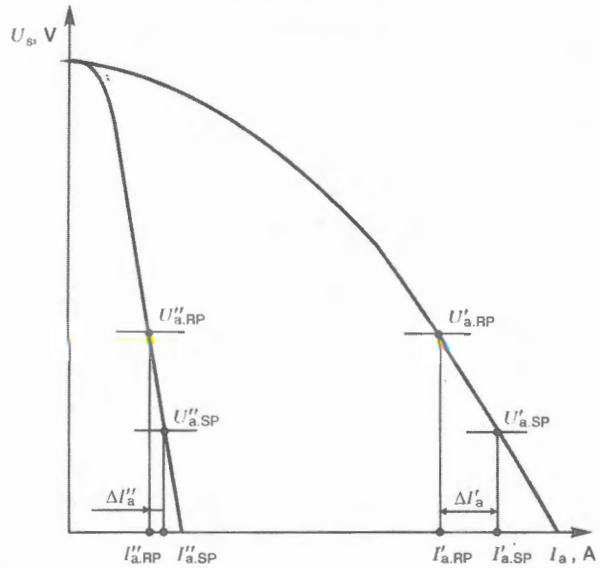

Figure 2. Effect of drop steepness of external volt-ampere characteristics of power source on $I_{a.SP} - I_{a.RP}$

As is seen, after changing polarity the exciting of the arc discharge occurs almost instantaneously, without a pause, and the values of arc voltage and current during the pulse duration can be taken constant only at certain assumptions. The values of arc voltage during pulse both at straight and also reverse polarity do not always remain unchanged. Thus, at comparatively high values of current some increase in arc voltage values is observed. Their increase during the pulse duration at a SP can be explained presumably by the reduction in temperature of the cathode spot at the electrode, as its heating is higher in current pulses at the RP. The growth of voltage in pulses at RP is due, probably, to the increase in «wandering» (with time) of the active spot at the aluminium cathode. Such change in voltage is correlated with data of [5]. Its authors consider that the intensive movement of the active spot at the aluminium cathode is a result of a high emissivity of oxides of this metal. The destroying of oxides in the process of arc burning under the action of the cathode sputtering leads to a continuous shifting of the active spot to the side of the oxidized regions and, as consequence, to the growth of the zone of the cathode cleaning. By the absolute value the voltage in arc gap in current pulses at reverse polarity ($U_{a.RP}$) is higher significantly than the similar value at straight polarity ($U_{a.SP}$) This is explained by differences in cathode processes occurring at the tungsten electrode and aluminium plate.

The value of arc current in pulses of current at straight polarity $I_{a.SP}$ and reverse polarity $I_{a.RP}$ are close and can be assumed equal. The allowable error, here, is equal to the difference $I_{a.SP} - I_{a.RP}$ and depends on the steepness of external volt-ampere characteristics of the power source, i.e. the large steepness the lower error (Figure 2). Power source which was used in the experiments had the external volt-ampere characteristics with a steepness 0.25 – 1.50 V/A in the operating region, that made it possible to consider $I_{a.SP} \cong I_{a.RP} \cong I_a$. In those cases when the current values in pulses at straight and reverse polarity are different initially ($I_{a.SP} \neq I_{a.RP}$) the effective current value should be determined from expression

$$I_a = \sqrt{1/T \int_0^T i_a^2 dt}, \qquad (1)$$

where i_a is the instantaneous value of arc current; T is the period duration.

Due to complexity of the processes occurring in the arc discharge, the static volt-ampere characteristics of the arc are presented usually graphically. In the case considered two variants of the graphical presentation of characteristics are possible. The first variant suggests the plotting of two volt-ampere characteristics (for arc gap of the same value): the first – for current pulses at reverse polarity (cathode–aluminium plate); the second – at straight polarity (cathode–tungsten electrode). The first volt-ampere characteristic is actually characteristic of arc of DCRP, while the second – at SP. Such approach is quite lawful, as τ_{SP} and τ_{RP} exceed many times the time of setting the arc discharge [6]. Some increase in voltage, observed above at separate conditions during the duration of pulses occurs under the conditions of a stationary burning of the arc [7].

The second variant suggests the plotting of the volt-ampere characteristics in which the effective value of voltage will serve a function. In a general case its value is determined by expression

$$I_a = \sqrt{1/T \int_0^T u_a^2 dt}, \qquad (2)$$

where u_a is the instantaneous value of voltage.

If to assume the values of voltages in current pulses at straight $U_{a.SP}$ and reverse $U_{a.RP}$ polarity constant, then the expression (2) for the AC arc is transformed as follows:

$$U_a = \sqrt{1/T}(U_{a.SP}^2 \tau_{SP} + U_{a.RP}^2 \tau_{RP}). \qquad (3)$$

Strictly speaking, only at the second variant the volt-ampere characteristics of AC arc are provided, because, as was above-mentioned, the volt-ampere characteristics plotted by the first variant are actually characteristics of arc of the direct current at straight and reverse polarity. However, to analyze the arc processes both variants of these characteristics are necessary.

The volt-ampere characteristics, obtained with the use of two variants, are presented in Figure 3. In both cases the frequency of AC pulses was 50 Hz, 3 mm electrode diameter, the duration of current pulse at the reverse polarity τ_{RP} was 1.25 ms, i.e. $0.0625T$ (Figure 3, *a*) and 6.25 ms, i.e. $0.3125T$ (Figure 3, *b*). It should be taken into consideration that values $U_{a.SP}$ and $U_{a.RP}$ are opposite in sign, though in Figure 3 they are shown similar for making the analysis more convenient. As is seen, characteristics $U_a = f(I_a)$,

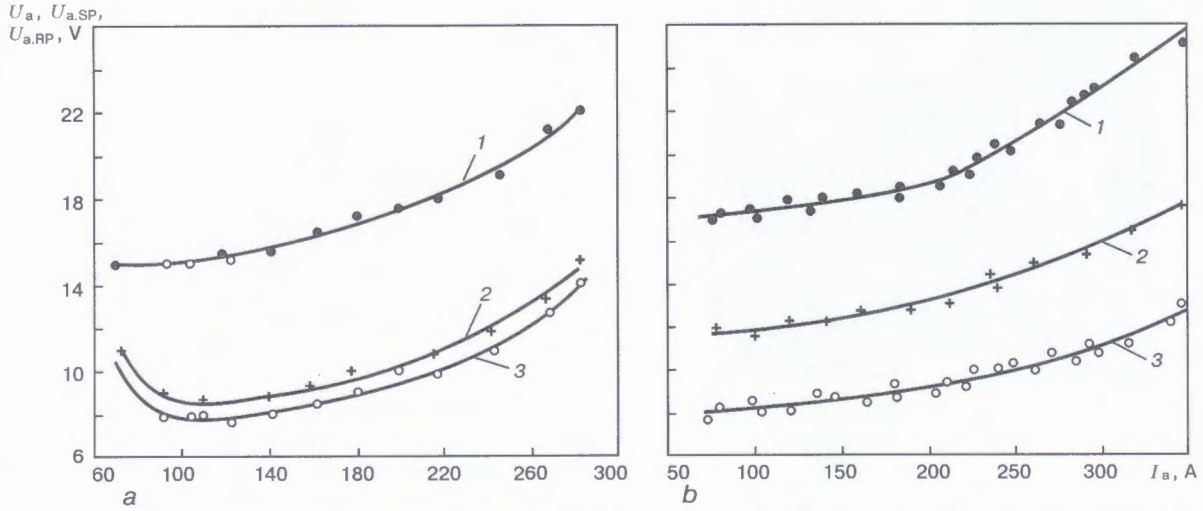

Figure 3. Volt-ampere characteristics of tungsten–aluminium arc at frequency of AC pulses 50 Hz and τ_{RP} = 1.25 (*a*) and 6.25 ms (*b*): *1* – $U_{a.RP}$; *2* – U_a; *3* – $U_{a.SP}$

$U_{a.SP} = f(I_a)$ and $U_{a.RP} = f(I_a)$ have a rising nature. The curves of volt-ampere characteristics shown in Figure 3, *a*, having the falling region within the 70 – 120 A current range, are an exception.

The more steep rising of curves of volt-ampere characteristics at current above 200 A is explained, probably, by increasing (with current increase) arc deepening into aluminium plate and, as consequence, by the arc elongation. It is known that with the increase in the arc length the curves of its volt-ampere characteristics are shifted to the side of the higher values of voltages. Consequently, the curves in Figure 3 are the volt-ampere characteristics only in the range of current values, not exceeding 200 A, when the arc deepening into the metal is absent or negligible; at the higher values of current these curves represent trajectories of transition from one volt-ampere characteristics to another characteristics corresponding to the larger length of the arc. As this deepening of the arc in welding is inevitable it is rational to make the appropriate corrections for producing the physically accurate volt-ampere characteristics.

The comparison of data presented in Figure 3 shows that with increase in τ_{RP} the volt-ampere characteristic $U_a = f(I_a)$ is shifted to the side of the higher voltages. As the results of experiments show the duration of τ_{RP} influence not only the effective values of voltage U_a that is quite evident, but also the values $U_{a.SP}$ and $U_{a.RP}$. Figure 4 presents relationships $U_a = f(\tau_{RP})$, $U_{a.SP} = f(\tau_{RP})$ and $U_{a.RP} = f(\tau_{RP})$. It should be noted that the value τ_{RP} is not occasionally selected as an argument. It is this parameter on which the most important characteristics of the arc in AC welding of aluminium and its alloys such as: life of the non-consumable electrodes, quality of the cathode cleaning of the surface welded, penetrability, depend [2]. As is seen the value of voltage U_a with a growth of τ_{RP} is first decreased a little (the arc power is also decreased here), and then it begins to grow, approaching the value $U_{a.RP}$. The voltage $U_{a.RP}$ at arc current 50 A is first increased to 17 V (with growth of τ_{RP}) and then remains unchanged (Figure 4, *a*). At current 100 A (Figure 4, *b*) the voltage $U_{a.RP}$ has almost constant (16.5 – 17.0 V) value within the whole range of changes τ_{RP}.

The relation $U_{a.SP} = f(\tau_{RP})$ presents a great interest. With the increase in duration τ_{RP} the value of voltage of the current pulse at straight polarity $U_{a.SP}$ is decreased monotonically, approaching 3.0 – 4.5 V when τ_{RP} constitutes a prevailing part of the period. Earlier, we did not meet such low value of the arc voltage in our experiments, as well as in the works

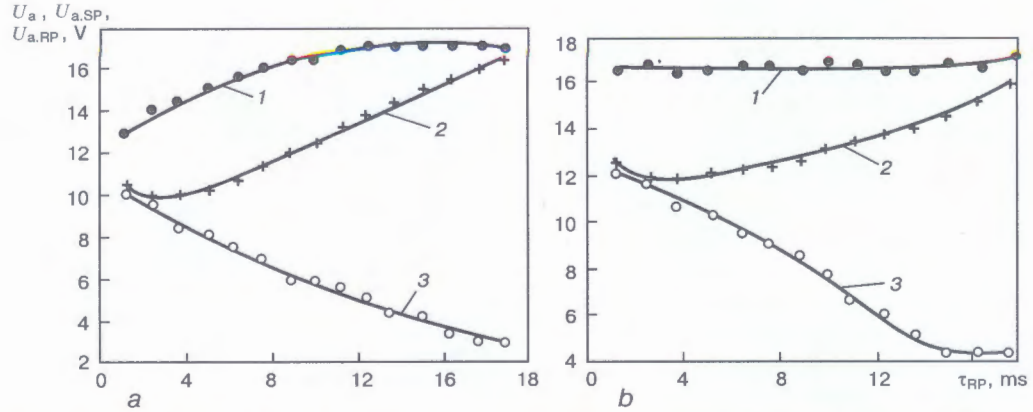

Figure 4. Effect of duration of current pulse at reverse polarity on voltage of tungsten–aluminium arc at I_a = 50 (*a*) and 100 A (*b*) (for designations *1* – *3* see Figure 3)

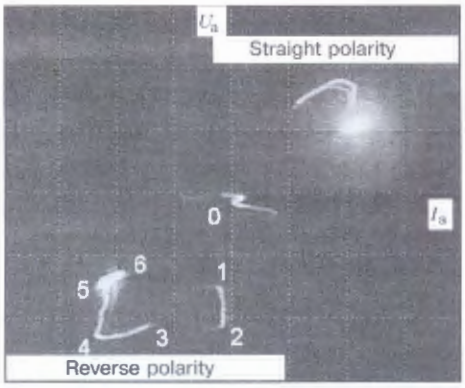

Figure 5. Dynamic volt-ampere characteristic of arc of square alternating current at 100 A, τ_{SP} = 16.25 and τ_{RP} = 3.75 ms (scale in voltage is 10 V/div.)

of other authors. It can be assumed that the decrease in $U_{a.SP}$ is caused to some extent by increase in the temperature of the working region of the tungsten electrode simultaneously with τ_{RP}. As a result the density of thermoemission current is increased and the voltage drop in the cathode region in pulses of current at straight polarity is decreased. However, this circumstance hardly explains such anomalously low value of the arc voltage. Probably, this problem requires a separate study.

The dynamic volt-ampere characteristics of the tungsten–aluminium arcs of square alternating current have also some peculiar features as compared with the arc of sinusoidal alternating current. These features are associated, first of all, with a high rate of changing the voltage in the arc gap at the moments of changing polarity and constancy of the current (if to neglect its negligible pulsating) during the duration of pulses of current at straight and reverse polarity.

Figure 5 presents the typical volt-ampere characteristic of such arc. It should be noted that to preserve the scale factor at taking characteristics, a shunt with a linear volt-ampere characteristic was used as a current sensor. In this connection some regions of the volt-ampere characteristic of the arc corresponding to the quickly proceeding processes are not seen in the oscillogram. A special interest is attracted by the processes connected with a repeated excitings of the arc at reverse polarity using an aluminium cathode which, as is known, play a great role for the stability of the arc burning [5, 6]. As is seen from the given dynamic characteristic, the arc voltage reaches jumpy the value close to the voltage of arc burning in the steady condition after changing polarity from straight to reverse due to a high rate of this process and, consequently, low level of the plasma deionizing (point *1* in Figure 5). However, there is no arc discharge at this moment, and in the interelectrode gap pre-arc processes are proceeding which are characterized by the growth of voltage at some decrease of the current values (region between *1* and *2*).

The data obtained in the oscillograph showed that the initial value of the pre-arc current is varied in the range from 5 to 30 A, and time of its proceeding is 20 – 80 μs.

After completion of formation of the cathode processes on aluminium the mechanisms typical of an electric arc are put into action and begin to be developed that is accompanied by an abrupt increase in current value and arc voltage decrease (regions *2* – *5*). The region between *5* and *6* is characterized by the arc burning in the steady condition during the duration of the pulse of current at reverse polarity and its length is determined by pulsating of the output voltage of the power source.

In case of exciting the arc of current at straight polarity the development of the arc processes begins only when the arc gap voltage after the polarity change exceeds the arc voltage due to a significant thermoelectron emission from the surface of the tungsten electrode and provided by its high conductivity of the cathode zone. The time of pause on the current curve in this case does not exceed 3 – 5 μs and determined, probably, by the rate of voltage increment in the arc gap. It should be noted that the time of transition processes at the moment of changing polarity in welding at sinusoidal alternating current can reach 4 – 6 ms. In this connection at current value of less than 70 A the arc is not steady in spite of use of the stabilizer of pulses [8].

By the above-mentioned peculiarities of the proceeding of the transition processes in changing polarity of square alternating current of tungsten–aluminium arc, this discharge is characterized by the higher elasticity and stability at tension as compared with the arc of the sinusoidal alternating current. As the practice showed the use of this arc for aluminium welding is possible at current of 5 A and more. Moreover, the auxiliary stabilizing devices are not required. To provide the stable arc burning the pulses of excess voltages, occurring in the arc gap as a result of commutation of power thyristors of inverters, are sufficient. Probably, the formation of these pulses explains the presence of the oscillogram region (see Figure 5) located near the zero mark, which is typical for all the conditions of the arc burning.

REFERENCES

1. Ishchenko, A.Ya., Chayun, A.G., Mishenkov, V.A. *et al.* (1978) Argon arc welding of aluminium alloy 01420 with variable-polarity square pulses of current. *Avtomaticheskaya Svarka*, **10**, 48 – 50.
2. Ishchenko, A.Ya., Poklyatsky, A.G., Yavorskaya, M.R. *et al.* (1990) Effect of asymmetry of variable-polarity square current on the parameters of welds in argon arc welding of AMg6 alloy. *Ibid.*, **1**, 26 – 28.
3. Korotkova, G.M., Slavin, G.A., Filippov, M.A. (1971) Investigation of process of welding with square AC arc. *Svarochnoye Proizvodstvo*, **10**, 4 – 6.
4. Novikov, O.M., Tokarev, V.O., Kazakov, V.A. *et al.* (1990) Effect of alternating current and condition of surface of aluminium alloys on efficiency factor in argon arc nonconsumable electrode welding. *Ibid.*, **8**, 43 – 44.
5. Finkelburg, V., Mekker, G. (1961) *Electric arcs and thermal plasma*. Moscow: Inostr. Literatura.
6. Leskov, G.I. (1970) *Electrical welding arc*. Moscow: Mashinostroyeniye.
7. Mirdel, G. (1972) *Electrophysics*. Moscow: Mir.
8. Korotkova, G.M. (1984) Dynamic characteristics of AC arc in welding aluminium alloys. *Avtomaticheskaya Svarka*, **11**, 30 – 32.

PECULIARITIES OF OPERATION OF HOT TUBULAR CATHODE HEATED BY LASER RADIATION

I.V. KRIVTSUN
The E.O. Paton Electric Welding Institute, NASU, Kyiv, Ukraine

ABSTRACT

Model of cathode processes for a hot tubular cathode of the laser-arc plasmatron, which takes into account additional heating of the working surface of the cathode by a passing laser beam, is suggested. Detailed computer modelling of cathode processes for the cathode under consideration was made. It is shown that additional laser heating can provide an efficient control of the cathode processes and, therefore, characteristics of plasma in the near-cathode region. The results obtained were used as the basis to design the cathode assembly for the laser-arc plasmatron intended for powder cladding. Experimental investigations of the plasmatron demonstrated a high operational stability and strength of the developed tubular cathode.

Key words: *hot tubular cathode, cathode processes, thermoemission, electric arc, laser beam, laser-arc plasmatron, investigations*

It is a known fact that interaction of the laser beam with the arc plasma may lead to formation of a special type of gas discharge, i.e. combined laser-arc discharge [1], which serves as the base for a new class of plasmatrons applied for hybrid laser-plasma welding and treatment of materials [2 – 4]. These devices differ from other known arc or optical (laser) plasmatrons in that they have extra capabilities for control of characteristics of the plasma (through varying parameters of the laser beam) and laser beam (through varying the arc burning mode). In addition, the laser-arc plasmatrons allow a substantial increase in a space-time stability of parameters of the generated plasma and decrease in the risk of arc twinning, which makes them highly promising for implementation of various technological processes [5].

Main peculiarity of the axisymmetric-type laser-arc plasmatrons [2 – 5] is a design of the cathode assembly. For example, it may be a refractory tubular cathode (Figure 1) or a system of the pin-like cathodes located on the circumference, which enables the laser beam to be introduced into the arc plasma along the axis of the plasma-shaping channel. The use of the hot tubular cathode also allows peripheral rays of the laser beam that passes through the cathode (Figure 1) to be employed for additional heating (in addition to arc heating) of the internal surface of the cathode tip. In this case, on the one hand, the cathode surface may be laser heated up to temperatures which ensure a minimum starting erosion of its material during initiation of the arc. On the other hand, this opens up a new way for controlling the cathode processes and, therefore, characteristics of the plasma in the near-cathode region of the combined discharge. In this connection, investigation into peculiarities of operation of the hot tubular cathode under atmospheric pressure of a surrounding gas, associated with laser heating of the tip of such a cathode, is a topical problem.

The purpose of the work described in this article consisted in development of a mathematical model and detailed numerical investigation of the cathode processes for the case of a hot tubular cathode heated up by laser radiation. In modelling these processes, for the cathode type under consideration we will use the most general approach which consists in a self-adjusting account for the entire set of interrelated physical phenomena occurring in the bulk of the cath-

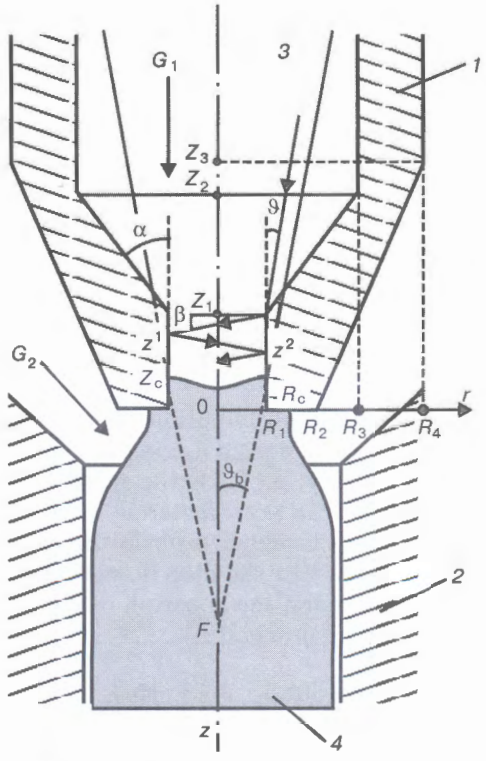

Figure 1. Schematic of the hot tubular cathode for the laser-arc plasmatron: *1* — refractory tubular cathode; *2* — plasma-shaping nozzle; *3* — laser beam; *4* — combined laser-arc discharge; G_1 and G_2 — flows of internal and external plasma gases, respectively; R_1, ..., R_4 and Z_1, ..., Z_3 — coordinates of points that determine the cathode surface shape; R_c and Z_c — coordinates of points that determine size of cathode fixation of the arc

ode, on its surface and in the near-cathode layer of the plasma [6].

The near-cathode layer of the plasma can be conditionally subdivided into two zones: quasi-neutral ionization region in which charged particles are generated, and layer of the space charge where the major part of the cathode potential drop occurs. The layer of the space charge, which directly adjoins the cathode surface, has thickness which is approximately equal to the Debye radius. It can be considered collisionless, as under a pressure of the surrounding gas close to the atmospheric one the length of a free path of particles is much larger than the Debye radius [7]. Electrons emitted by the cathode are accelerated by the electric field of the space charge and acquire the energy sufficient for ionization of atoms of the plasma gas in a collision ionization layer. The formed ions and high-energy electrons of the plasma, which are capable of overcoming the cathode potential drop (so-called reverse electrons), get onto the surface of the cathode and give it their energy required for heating the cathode and generating the thermoemission current.

As it has been noted above, in addition to input of the energy through the arc spot, design of the hot tubular cathode under consideration makes it possible to use part of the power of the laser beam that passes though a opening in the cathode for heating the internal surface of the cathode. For this purpose, geometrical parameters of this surface should be selected so that peripheral rays of the beam, upon reflection from the internal conical surface of the cathode, get into its cylindrical discharge opening and have a sufficient amount of reflections to be fully absorbed by the cathode material.

To calculate the resulting temperature field in the bulk of the cathode, which is assumed to be axisymmetric, we will use the stationary quasi-linear equation of thermal conductivity with allowance for Joule heat release:

$$\frac{1}{r}\frac{\partial}{\partial r}\left(r\chi_c \frac{\partial T_c}{\partial r}\right)+\frac{\partial}{\partial z}\left(\chi_c \frac{\partial T_c}{\partial z}\right)+\rho_c j_c^2 = 0, \qquad (1)$$

where $T_c(r, z)$ is the distribution of temperature in the bulk of the cathode; $\chi_c(T_c)$ is the coefficient of thermal conductivity; $\rho_c(T_c)$ is the specific electrical resistance of the cathode material and $j_c(r, z) = -\nabla\Phi_c/\rho_c$ is the current density in the cathode.

Here distribution of the electric potential, $\Phi_c(r, z)$, can be found using the equation of continuity of the electric current in metal

$$\frac{1}{r}\frac{\partial}{\partial r}\left(\frac{r}{\rho_c}\frac{\partial\Phi_c}{\partial r}\right)+\frac{\partial}{\partial z}\left(\frac{1}{\rho_c}\frac{\partial\Phi_c}{\partial z}\right)=0. \qquad (2)$$

Boundary conditions on the cathode surface for equations (1) and (2) are set on the basis of the following assumptions. It is assumed that the refractory cathode investigated is pressed-in into a copper water-cooled yoke. Then, at

$$z = -L_e, \quad R_3 \le r \le R_4,$$

where L_e is the length of the cathode extension, it can be considered that

$$T_c = T_w, \quad \Phi_c = 0, \qquad (3)$$

where T_w is the cooling water temperature. It is assumed that conditions on the external surface of the cathode, outside the arc fixation zone, involve the presence of convection-radiation heat exchange with the surrounding gas and absence of a component of the electric current density, normal to this surface. Therefore, at $r = R_4$, $-L_e \le z < Z_3$, $r = R_2 + \frac{(R_4 - R_2)z}{Z_3}$, $Z_3 \le z < 0$ and $R_c < r \le R_2$, $z = 0$ (see Figure 1), the boundary conditions have the following form:

$$-\chi_c \nabla_n T_c = \alpha_{c_2}(T_c - T_2) + \varepsilon_c\sigma_0 (T_c^4 - T_2^4),$$
$$\nabla_n\Phi_c = 0, \qquad (4)$$

where ∇_n is the temperature gradient component, normal to the cathode surface; α_{c_2} is the coefficient of heat exchange of the cathode surface with an external flow of the plasma gas; T_2 is the temperature of this gas; ε_c is the emissivity factor of the cathode material and σ_0 is the Stefan–Boltzmann constant. Boundary conditions on the internal surface of the cathode, outside the zone of contact with the plasma, i.e. at $r = R_3$, $-L_e \le z < Z_2$, $r = R_1 + \frac{(R_3 - R_1)(z - Z_1)}{Z_2 - Z_1}$, $Z_2 \le z < Z_1$ and $r = R_1$, $Z_1 \le z < Z_c$ (see Figure 1), are selected in a similar way (4)

$$-\chi_c \nabla_n T_c = -\alpha_{c_1}(T_c - T_1) - \varepsilon_c\sigma_0 (T_c^4 - T_1^4),$$
$$\nabla_n\Phi_c = 0, \qquad (5)$$

where α_{c_1} is the coefficient of heat exchange of the cathode surface with an internal flow of the plasma gas and T_1 is its temperature*.

Boundary conditions in a region of the cathode fixation of the discharge (see Figure 1) are set as follows:

$$-\chi_c \frac{\partial T_c}{\partial z} = -q_c^a, \quad -\sigma_c \frac{\partial\Phi_c}{\partial z} = -j_c \text{ at } R_1 \le r \le R_c,$$
$$z = 0 \qquad (6)$$

and

$$-\chi_c \frac{\partial T_c}{\partial r} = q_c^a, \quad -\sigma_c \frac{\partial\Phi_c}{\partial r} = j_c \text{ at } r = R_1,$$
$$Z_c \le z \le 0, \qquad (7)$$

*Values of α_{c_1} and α_{c_2}, as well as the corresponding values of temperatures $T_1(z)$ and $T_2(z)$, are determined depending on the G_1 and G_2 flows of the plasma gas used, and on its feed conditions and thermal-physical properties.

where q_c^a is the density of the heat flow introduced into the cathode by the arc; j_c is the current density on the cathode surface (q_c^a and j_c are assumed to be distributed over the cathode fixation region).

Distribution of the heat flow of the arc, $q_c^a(r_s, z_s)$ over the surface of the cathode fixation of the discharge (here r_s and z_s are the point coordinates on this surface) can be found using the system of equations given in [3]. To allow for additional laser heating of the internal cathode surface, boundary conditions (5) and (7) for the equation of thermal conductivity should be corrected by adding term q_c^a to the right parts of the above conditions to describe distribution of the power of laser radiation absorbed by the internal conical surface of the cathode and the surface of its discharge opening.

Prior to determination of distribution of the radiation power absorbed by the internal surface of the cathode, consider condition at which all rays of the laser beam reflected from the conical part of this surface get into the discharge opening of the cathode. If

$$F^2 >> [\lambda/(\pi\, \vartheta_b^{\,2})]^2$$

(here λ is the laser radiation wave length and ϑ_b is the angle of focusing of the laser beam), in the $z < 0$ range this beam can be assumed to be a set of straight-line rays, spherically converging to the point of intersection of the focal plane with the beam axis, where each ray is characterized by its peculiar value of angle ϑ (see Figure 1). By defining ϑ_b as the angle within which 99 % of the laser radiation power is distributed, and by assuming it to be small ($\mathrm{tg}\, \vartheta_b \approx \vartheta_b$), the unknown condition for the rays which get onto the internal conical surface of the cathode can be written as follows:

$$R_1 [(\mathrm{tg}\, \alpha - 2\vartheta)\, \mathrm{tg}\, \beta + 1] + (F - Z_1)(\mathrm{tg}\, \alpha\, \mathrm{tg}\, \beta - 1)\, \vartheta \geq 0, \quad \left(\frac{R_1}{F - Z_1} \leq \vartheta \leq \vartheta_b\right) \tag{8}$$

In this case, location of the conjugate points for the reflected rays in the discharge opening of the cathode (see Figure 1) can be determined using recurrent relationships

$$z^1(\vartheta) = Z_1 + \frac{R_1 [(\mathrm{tg}\, \alpha - 2\vartheta)\, \mathrm{tg}\, \beta + 1]}{\mathrm{tg}\, \alpha - \vartheta} + \frac{(F - Z_1)(\mathrm{tg}\, \alpha\, \mathrm{tg}\, \beta - 1)\, \vartheta}{\mathrm{tg}\, \alpha - \vartheta}, \tag{9}$$

$$z^{i+1}(\vartheta) = z^i(\vartheta) + 2R_1 \mathrm{tg}\, \beta \quad (i = 1, 2, 3, \ldots),$$

where $\beta(\vartheta) = \frac{\pi}{2} - 2\alpha + \vartheta$ is the angle of inclination of the reflected rays with respect to the horizontal plane. These rays have no less than n reflections in the discharge channel of the cathode, provided that

$$z^n(\vartheta) \leq 0, \quad \left(\frac{R_1}{F - Z_1} \leq \vartheta \leq \vartheta_b\right), \tag{10}$$

and the required number n of reflections of the rays within the discharge channel for their efficient (no less than 90 %) absorption by the cathode surface can be estimated using the following relationship:

$$(1 - \Gamma)^{n+1} \leq 0.1, \tag{11}$$

where Γ is the coefficient of absorption of laser radiation with a given wave length by the cathode surface material*.

Condition (8) being met, distribution of the laser radiation induced heat flow, $q_c^l(R_1, z)$, along the length of the cathode discharge channel ($Z_1 \leq z \leq 0$) can be written as follows:

$$q_c^l = \int_{\frac{R_1}{F - Z_1}}^{\vartheta_b} \sum_{i=1}^{\infty} \delta [z - z^i(\vartheta)]\, \theta [-z^i(\vartheta)] \times S^i(\vartheta) \cos \beta\, \Gamma^i(\vartheta)\, d\vartheta. \tag{12}$$

Here $\delta(x)$ is the delta function;

$$\theta(x) = \begin{cases} 1 & \text{at } x \geq 0, \\ 0 & \text{at } x < 0; \end{cases}$$

$S^i(\vartheta)$ is the intensity of incident laser radiation for the corresponding conjugate points of the discharge channel surface; $\Gamma^i(\vartheta) \equiv \{T_c[R_1, z^i(\vartheta)]\}$ are the values of the coefficient of absorption of laser radiation by the cathode material at the same points. Absorption of the reflected rays in plasma at $z \leq Z_c$ being ignored, values of the intensity of incident radiation for all conjugate points, $z^i(\vartheta)$, can be found using the following recurrent relationships:

$$S^1(\vartheta) = S^0(\vartheta) \frac{\mathrm{tg}\, \alpha}{\cos \beta} R(\vartheta) \frac{[(F - Z_1)\, \mathrm{tg}\, \alpha - R_1]^2 \vartheta}{R_1 z_\vartheta^1 (\mathrm{tg}\, \alpha - \vartheta)^3}, \tag{13}$$

$$S^{i+1}(\vartheta) = S^i(\vartheta)\, [1 - \Gamma^i(\vartheta)] \frac{z_\vartheta^i}{z_\vartheta^{i+1}} \quad (i = 1, 2, 3, \ldots),$$

which use the following designations: $z_\vartheta^i \equiv \frac{dz^i}{d\vartheta}$, $S^0(\vartheta)$ is the intensity of radiation of the initial laser beam $S^0(r, z)$ at a point of incidence of a ray at angle ϑ on the internal conical surface of the cathode, i.e. at

$$r = \frac{[(F - Z_1)\, \mathrm{tg}\, \alpha - R_1]\vartheta}{\mathrm{tg}\, \alpha - \vartheta}, \quad z = \frac{Z_1 \mathrm{tg}\, \alpha - F\vartheta + R_1}{\mathrm{tg}\, \alpha - \vartheta},$$

$R(\vartheta)$ is the coefficient of reflection of laser radiation at the same point on the surface. Using the accepted

*As the angle of incidence of the reflected rays onto the surface of the discharge opening of the cathode is small, here and below Γ will stand for the value of the absorption coefficient at a normal incidence of the rays, which is independent of the radiation polarization and corresponds to a local value of the surface temperature.

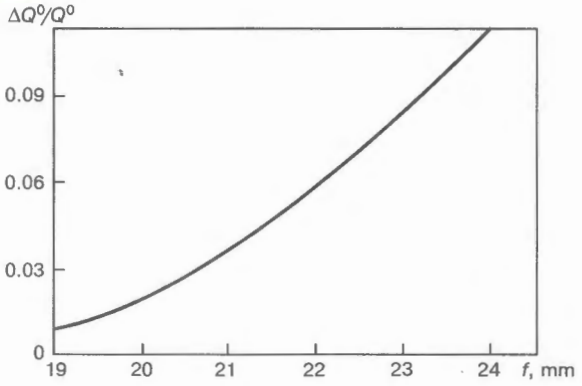

Figure 2. Part of power of the laser beam falling on the internal surface of a tubular cathode as function of its position with respect to the focal plane of the initial beam (see designations in the text)

designations for the density of heat flow q_c^l introduced by laser radiation through the conical part of the internal surface of the cathode ($z < Z_1$) at the point of incidence of a ray, ϑ, yields

$$q_c^l = S^0(\vartheta) \sin \alpha [1 - R(\vartheta)]. \qquad (14)$$

Note that distributions of the heat flow (12) and (14) are assumed to be axisymmetric. Therefore, for laser beams with azimuth variations in the intensity of radiation, to determine dependence $S^0(\vartheta)$ it is necessary to use the azimuth-averaged distribution of the initial beam intensity. As far as the reflection coefficient $R(\vartheta)$ is concerned, since the angle of incidence of the rays onto the internal conical surface (it is approximately equal to $\pi/2 - \alpha$) is not small, this coefficient will depend not only upon the temperature of the surface at the point of incidence of a corresponding ray, but also upon the polarization of radiation in the initial laser beam. To avoid the azimuth dependence of q_c^l, which arise in this case, the approximate corresponding value of the reflection coefficient can be used as $R(\vartheta)$ in (13) and (14) for a non-polarized radiation that has an incidence angle of $\pi/2 - \alpha$.

Numerical investigations of cathode processes for a hot tubular cathode used in the laser-arc plasmatron were conducted on the basis of assumptions of the suggested mathematical model [5]. This plasmatron was designed for operation at arc currents of $100 \leq I \leq 300$ A using the radiation beam of a CO_2 laser with the TEM_{20} mode, power $Q^0 \leq 5$ kW and focusing angle $\vartheta_b = 0.053$ determined as indicated above. The following external sizes of the tubular cathode (see Figure 1) were selected for design of the cathode assembly: $R_2 = 2.0$ mm, $R_4 = 4.5$ mm, $Z_3 = -5.0$ mm and $L_e = 20$ mm. At the same time, the provision was made to enable regulation of laser heating of the cathode tip. For this purpose, radius of the cylindrical discharge opening of the cathode, R_1, was assumed to be equal to 1 mm and distance from plane $z = Z_1$ to the focus of the initial beam, $f = F - Z_1$, was supposed to be varied within a range of $16 \leq f \leq 24$ mm. For the above values of R_1 and ϑ_b, the noticeable heating of the cathode by laser radiation will be observed at $f \geq 19$ mm. Dependence of the power of laser radiation falling on the internal surface of the cathode, ΔQ^0, upon its position with respect to the focal plane of the beam with the TEM_{20} mode is shown in Figure 2. It should be noted at this point that further increase in distance from the initial beam focus to the cathode ($f > 24$ mm) is unreasonable, as this, in addition to growth of ΔQ^0, leads to a substantial diffraction distortion of the beam passing through the cathode opening.

Flare angle α of the internal conical surface of the cathode and length of its discharge opening, $-Z_1$ (see Figure 1) were selected on the basis of optimal utilization of the power of laser radiation consumed for heating of the surface of the cathode discharge opening. Conditions (8), (10) and (11) were used for this purpose. They mean that peripheral rays of the laser beam reflected from the conical part of the internal surface of the cathode get into the discharge opening of the cathode and have there the sufficient number of reflections for their efficient absorption. As the coefficient of absorption of laser radiation with a wave length of $\lambda = 10.6$ μm by the surface of the tungsten cathode at a temperature of 2000 to 3000 K and normal incidence is equal to $\Gamma \approx 0.1$ [8], the required number of reflections within the discharge channel of the cathode for condition (11) to be met should be not less than 20. On this basis, the optimal values (for the entire range of variations in values of f) of geometrical parameters of the internal surface of the cathode were determined as follows: $\alpha = 42.5$ deg, $Z_1 = -2$ mm and $R_3 = 3$ mm.

Activated tungsten ($W + 1\ \% Y_2O_3$), having a work function equal to $\varphi_c = 3.3$ eV [9], was selected as the cathode material. Temperature dependencies of thermal conductivity coefficient χ_c, specific electrical resistance ρ_c, emissivity factor ε_c and coefficients of absorption, Γ (at normal incidence), and reflection, R (at an incidence angle of 47.5 deg), of a non-polarized radiation of the CO_2 laser for tungsten were derived on the basis of data in [10, 11].

Flow rate of the plasma gas (argon) fed through the cathode opening was selected to be equal to 0.5 l/min (under standard conditions), while that of the gas fed through the gap between the cathode and the plasma-shaping nozzle was varied from 1.5 to 3.5 l/min. Values of temperatures of the internal, $T_1(z)$, and external, $T_2(z)$, argon flows, averaged over the channel sections, were determined with allowance for heating of the gas from the cathode surface. Here the initial temperature of the plasma gas was assumed to be equal to the temperature of water that cools the cathode: $T_1(-L_e) = T_2(-L_e) = T_w = 300$ K. The following criterial dependencies [12] were used to calculate heat exchange coefficients α_{c_1} and α_{c_2} that are included into (4) and (5):

$$\alpha_{c_j} = \mathrm{Nu}_j \frac{\chi(T_j)}{D_j} \left[\frac{\eta(T_j)}{\eta(T_c)}\right]^{0.14} \quad \text{at } j = 1, 2, \qquad (15)$$

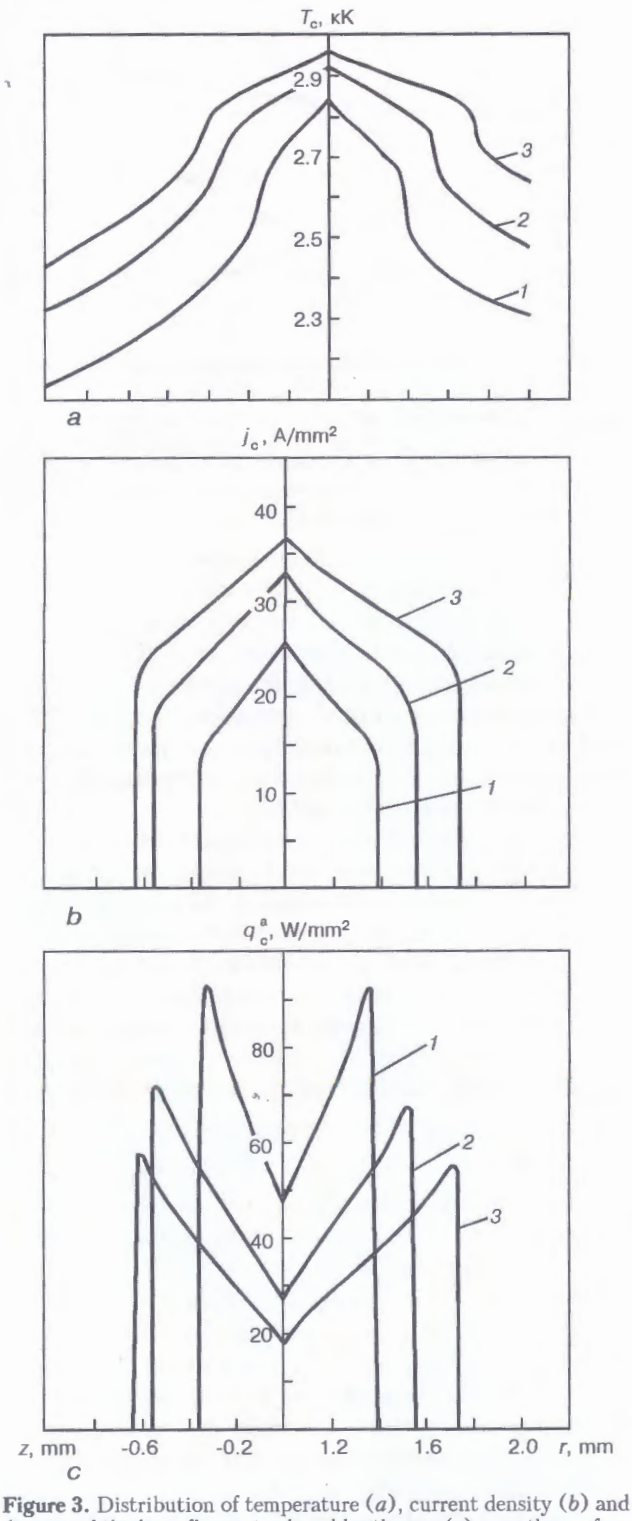

Figure 3. Distribution of temperature (*a*), current density (*b*) and density of the heat flow introduced by the arc (*c*) over the surface of the hot tubular cathode operating at different currents (G_2 = = 2.5 l/min, $Q^0 = 0$ or $F < 17$ mm): *1* — $I = 100$; *2* — $I = 200$; *3* — $I = 300$ A

where $Nu_1 \cong 4$, $Nu_2 \cong 5$ are the Nusselt numbers for the internal and external gas flows, respectively; D_1 and D_2 are the internal and external diameters of the cathode, respectively; χ and η are the temperature dependencies of the heat exchange coefficients for argon [1].

Results of numerical modelling of operation of the investigated hot tubular cathode both in the conventional arc mode and in the mode involving an additional laser heating of the cathode tip are shown in Figures 3 – 7. In particular, Figure 3 shows distribution of temperature, current density and heat flow introduced by the arc at the absence of laser heating of the cathode over the working surface of the cathode. As it follows from Figure 3, *a* and *b*, an increase in current is accompanied by an increase in temperature of the cathode surface and area of the cathode fixation of the arc, this area at $I > 200$ A being increased mostly due to the cathode tip. This is associated with the fact that further immersion of the arc into the discharge opening of the cathode becomes unfavourable in terms of energy, as it is accompanied by a substantial growth of voltage in the plasma region inside this opening.

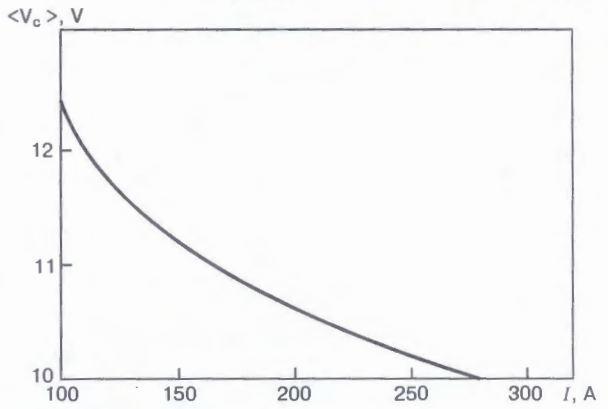

Figure 4. Mean cathode potential drop as function of the arc current for the hot tubular cathode (see the rest of the cathode operation parameters in Figure 3)

As the arc current increases from 100 to 300 A, the mean current density at the cathode

$$<j_c> = I/S_c,$$

where $S_c = \pi\left(R_c^2 + 2R_1Z_c - R_1^2\right)$ is the area of the cathode fixation of the discharge (see Figure 1), increases from 19.2 to 29.2 A/mm². As to the mean density of the heat flow directed to the cathode

$$< q_c^a > = Q_c^a/S_c,$$

where Q_c^a is the total heat flow from the arc, calculated by integration of q_c^a with respect to the area of the cathode fixation of the arc, it, on the contrary, decreases from 70.9 (at $I = 100$ A) to 37.8 W/mm² (at $I = 300$ A). In addition, unlike distributions T_c and j_c, having maximum values at points $r = R_1$, $z = 0$ (Figure 3, *a*, *b*), maximum values of heat flow q_c^a are observed at the periphery of the arc fixation region (Figure 3, *c*). It should be noted that this distribution of the heat flow at the cathode takes place also for solid (not tubular) hot cathodes [13].

Figure 4 shows the arc current dependence of mean cathode potential drop $<V_c>$, calculated using values of components of the current density at the cathode, its surface temperature that ensurs the corresponding mean density of the emission current, and mean temperature of the plasma in the ionization layer, aver-

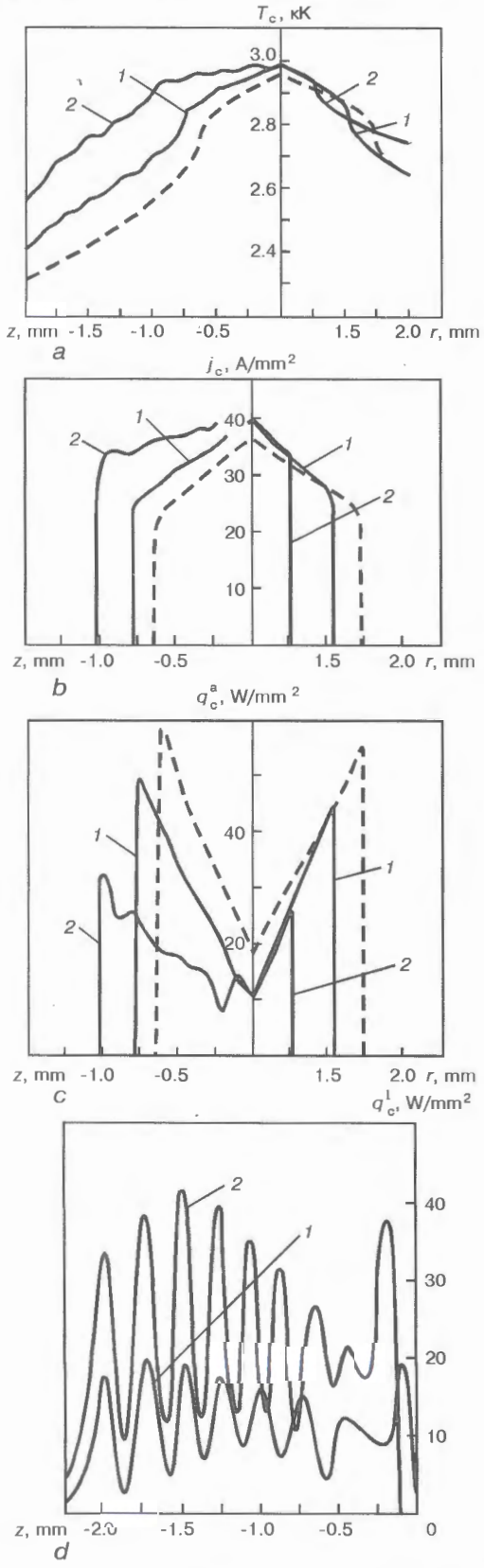

Figure 5. Distribution of temperature (*a*), density of the electric current (*b*), density of the heat flows introduced by the arc (*c*) and laser beam (*d*) over the surface of the hot tubular cathode additionally heated by laser radiation (I = 300 A, Q^0 = 5 kW, G_2 = = 2.5 l/min) at a different distance from the cathode exit section to the focal plane of the initial laser beam: *1* — F = 19 mm (Q_c^l = = 166 W); *2* — 21 mm (Q_c^l = 325 W); dashed lines — F < 17 mm (Q_c^l = 0)

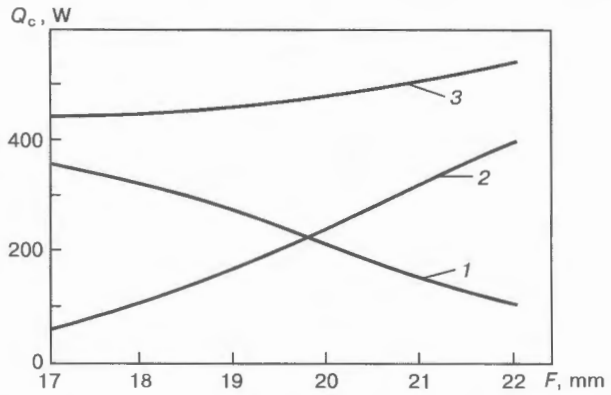

Figure 6. Components of the total heat flow introduced into the cathode operating in the laser-arc mode as function of the distance from the cathode to the focal plane of the laser beam: *1* — Q_c^a; *2* — Q_c^l; *3* — Q_c^{tot} (the rest of the parameters of the cathode operation are the same as in Figure 5)

aged over the cathode fixation region. The mean temperature of the plasma in the ionization layer was found using the equation of energy balance of the near-cathode plasma [3], written down with respect to the corresponding averaged values. As it follows from the given calculated dependence, for the hot tubular cathode under consideration $<V_c>$ decreases with an increase in current, which is characteristic in general of the hot cathodes [6].

The effect of additional laser heating of the tip of the cathode investigated on the character of occurrence of the cathode processes is illustrated in Figures 5 – 7. For example, Figure 5 shows distribution of temperature, current density and density of the heat flows introduced by the arc and laser beam, respectively, over the working surface of the cathode at different values of the power of laser radiation absorbed by the cathode, Q_c^l, determined as integral of q_c^l with respect to the internal surface of the cathode. Growth of Q_c^l (curve *2* in Figure 6), occurring with an increase in distance F, causes some increase in temperature of the surface of the cathode, which is especially noticeable inside its discharge opening (Figure 5, *a*). Distribution of temperature, as well as j_c and q_c^a (Figure 5, *b, c*), along the length of the discharge channel of the cathode, which non-monotonous in this case, is associated with a non-uniformity of heating of the cathode surface by laser radiation (Figure 5, *d*), increasing with a growth of F (compare curves *1* and *2* in Figure 5, *d*).

Important peculiarity of the cathode processes for the cathode under consideration is a decrease in density of the heat flow introduced into the cathode by the arc, at an increase in Q_c^l and constant current (Figure 5, *c*). In this case, the mean density of the heat flow at the cathode, $<q_c^a>$, varies from 37.8 (F < 17 mm) to 13.4 W/mm² (F = 22 mm), and Q_c^a decreases so that the total heat input into the cathode, $Q_c^{tot} = Q_c^a + Q_c^l + Q_c^j$, increases with growth in F very insignificantly (curve *3* in Figure 6). It should be noted here that power released in the bulk

of the cathode due to the current flow, Q_c^j, is not in excess of 10 % of Q_c^{tot}.

As far as the mean density of the current at the cathode is concerned, since the area of the cathode fixation at an increase in Q_c^l and constant arc current ($I = 300$ A) decreases to some extent, the mean current density $\langle j_c \rangle$ rises from 29.2 ($F < 17$ mm) to 37.4 A/mm^2 ($F = 22$ mm). In this case, the region of the cathode fixation of the discharge shifts from the tip of the cathode to its internal, more heated surface (Figure 5, *b*). This immersion of the discharge into the cathode opening becomes possible owing to a local decrease in the cathode potential drop that occurs here (see, e.g. dependence of the mean cathode potential drop upon the values of F and, thus, upon Q_c^l as shown in Figure 7). This leads to a substantial growth of that part of the total discharge current which flows to the cathode within the limits of its discharge opening. For example, at $I = 300$ A, $Q^0 = 5$ kW and $F = 21$ mm ($Q_c^l = 325$ W), this part of the current is about 230 A, and density of the current in the plasma at the exit section of the discharge opening of the cathode is about 100 A/mm^2, which is much higher than at the cathode surface. Therefore, the use of additional laser heating of the internal surface of the hot tubular cathode allows an efficient control of distribution of the current density and, thus, the concentration of energy in the plasma near such a cathode. This enables density of the energy introduced by the arc into a workpiece to be fundamentally increased not only in laser-plasma treatment of materials (by using the plasma arc in the combined process), but also in combined laser-arc welding using a short free-burning arc and a refractory tubular cathode heated up by laser radiation. In the latter case the role of the plasma-shaping channel is played by the discharge channel of such a cathode.

In general, results of numerical modelling of the cathode phenomena for a hot tubular cathode are indicative of the possibility of increasing the temperature of the cathode surface and current density in a region of the cathode fixation of the arc, changing location of this region and, therefore, redistributing the current density in the near-cathode plasma due to additional regulated heating of the working surface of the cathode by a passing laser beam. The calculation results were used as the basis for design of the cathode

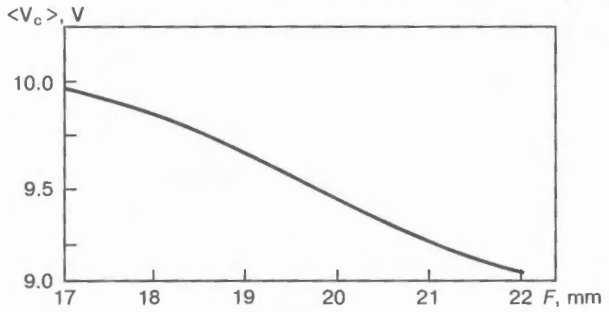

Figure 7. Mean cathode potential drop for the hot tubular cathode additionally heated by laser radiation as function of the distance of the cathode from the focal plane of the laser beam (parameters are the same as in Figure 5)

assembly of the integrated laser-arc plasmatron intended for powder cladding [5]. Experimental studies of the plasmatron developed proved the results of modelling of the cathode processes, and demonstrated a high stability of operation of the hot tubular cathode heated up by laser radiation and the absence of a marked erosion of its material after more than eight-hour operation with multiple arc ignitions.

REFERENCES

1. Gvozdetsky, V.S., Krivtsun, I.V., Chizhenko, M.I. *et al.* (1995) Laser-arc discharge: Theory and application. *Welding and Surfacing Rev.*, Vol. 3, Part 3. Harwood A.P.
2. Paton, B.E. (1995) Upgrading of the welding methods – one of the ways of improvement of the quality and cost effectiveness of welded structures. *Avtomaticheskaya Svarka*, **11**, 3 – 11.
3. Krivtsun, I.V., Chizhenko, M.I. (1997) Principles of calculation of laser-arc plasmatrons. *Ibid.*, **1**, 16 – 23.
4. Dykhno, I.S., Krivtsun, I.V., Ignatchenko, G.N. *Combined laser and plasma arc welding torch*. Pat. **5700989** USA, Int. Cl. I 23 K 26/00, 10/00. Publ. 23.12.97.
5. Som, A.I., Krivtsun, I.V. (2000) Laser + plasma: search for new possibilities in surfacing. *The Paton Welding Journal*, **12**, 34 – 39.
6. Zhukov, M.F., Kozlov, N.P., Pustogarov, A.V. *et al.* (1982) *Near-electrode processes in arc discharges*. Novosibirsk: Nauka.
7. Krivtsun, I.V. (2001) Model of evaporation of metal in arc, laser and laser-arc welding. *The Paton Welding Journal*, **3**, 2 – 9.
8. Dewley, W. (1986) *Laser technology and analysis of materials*. Moscow: Mir.
9. Fomenko, V.S. (1981) *Emissive properties of materials*. Refer. Book. Kyiv: Naukova Dumka.
10. (1976) *Tables of physical values*. Refer. Book. Ed. by I.K. Kikoin. Moscow: Atomizdat.
11. Noskov, M.M. (1983) *Optical and magneto-optical properties of metals*. Sverdlovsk: UNTs AN SSSR.
12. Kutateladze, S.S. (1979) *Principles of the theory of heat transfer*. Moscow: Atomizdat.
13. Mojzhes, B.Ya., Nemchinsky, V.A. (1973) On the theory of the high-pressure arc at a refractory cathode. *Zhurnal Tekhn. Fiziki*, **11**, 2309 – 2317.

IMPROVEMENT OF ARCING STABILITY IN THE TWO-LOOP RESONANCE DEVICES

A.E. KOROTYNSKY
The E.O. Paton Electric Welding Institute, NASU, Kyiv, Ukraine

ABSTRACT

A resonance welding source, made as a two-loop circuit, is described. It is shown that a high stability of the welding arc is achieved by using a high-voltage complementary loop of not more than 400 W power. An example of the complementary loop calculation is given, as well as the results of testing the unit with different types of stick electrodes.

Key words: *arc welding, voltage resonance, arc elasticity*

Arcing stability is one of the major process parameters, determining the quality of welded joint formation. It depends not only on the composition and properties of the arc column plasma, but to a greater extent, on the static and dynamic characteristics of arc power sources [1].

Voltage increase across the arc gap at polarity reversal, is a traditional method of improvement of the welding arc stability. It is usually achieved by increasing the open-circuit voltage of the welding transformer [2], this, however, leading to a higher cost of the source, lowering of its efficiency and power factor, as well as lower electrical safety.

Such technical solutions should be regarded as more suitable, which use pulsed arc stabilizers [3], allowing a 20 – 30 % decrease of open-circuit voltage. The range of suitable types of electrodes is also widened. In some units [4], arcing stabilization is achieved by applying a complementary high-frequency converter of ≤ 20 kHz frequency, connected parallel to the arc gap. Superposition of high-frequency oscillations of a small amplitude provides 1.5 – 1.8 times increase of the arc breaking length. The main drawback of this equipment class is a significant widening of the spectrum of noise, penetrating into the mains and the environment. In a number of cases, when these units do not meet the electromagnetic compatibility requirements, their application is inadmissible.

Resonance welding sources, mostly made by a single-loop circuit for use with rutile electrodes [5, 6], do not have the above short-comings. Circuits with voltage resonance in the secondary loop are often used. The voltage present on the capacitive reactor, is limited at the level of $U_2 \leq 42$ V, this being related to the reliability of functioning of electrolytic capacitors, making up the reactor. This voltage, however, is not sufficient for a stable operation of this type of units, in welding with electrodes with the basic and rutile coating. Even at increase of secondary voltage up to 48 V, it is difficult to provide reliable conditions of the arc reignition.

This problem can be solved by using a two-loop circuit for supplying power to the welding arc. The essence of this suggestion is as follows. A complementary loop is co-phased with the main loop with the current load of 90 – 95 %. The voltage at the reactor of this additional loop is equal to 75 – 80 V. Considering the small current (10 – 20 A), flowing through the complementary reactor, it is rather simple to en-

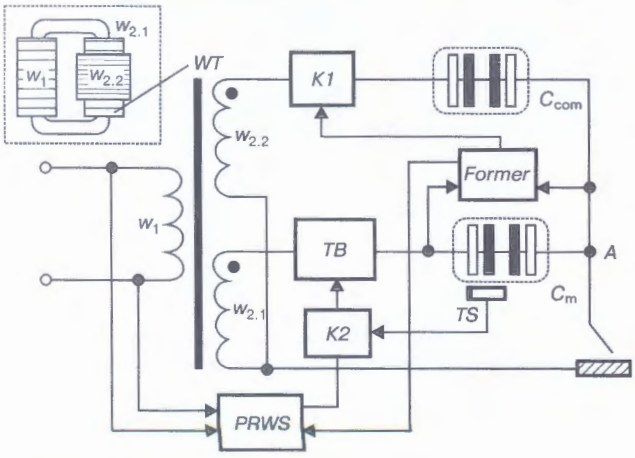

Figure 1. Block-diagram of a welding source

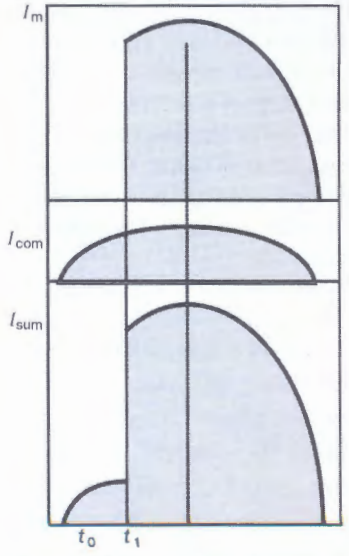

Figure 2. Time diagrams of currents in the summation point

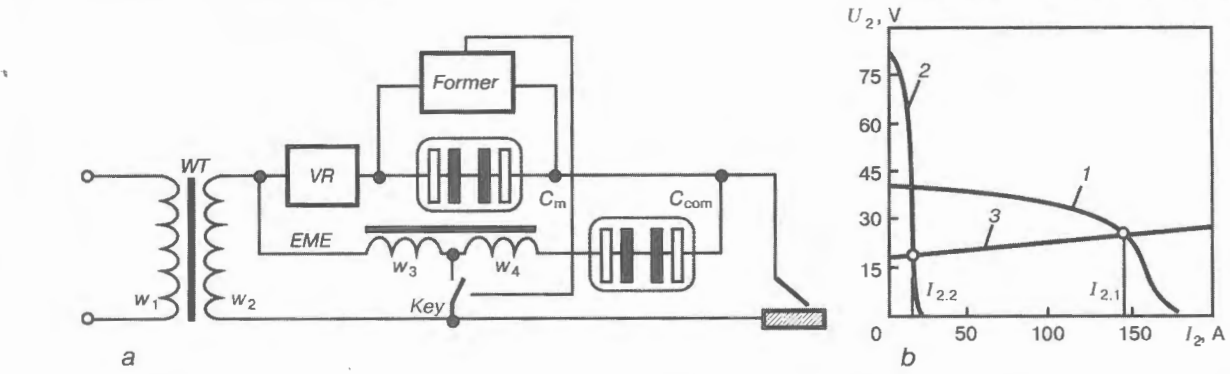

Figure 3. Welding source, made by a two-loop circuit with a changing structure (*a*) and its external characteristic (*b*): *1* — external characteristic of the main loop; *2* — the same for the complementary loop; *3* — dependence of U_2 on welding current ($U_2 = 18 + 0.04I_2$); *VR* — voltage regulator

sure its reliable operation. A high arcing stability in welding with basic and rutile electrodes is guaranteed exactly due to increase of voltage in the complementary loop.

As an example, let us calculate the complimentary loop parameters with the following initial data: $U_{2com} = 80$ V; $I_{2com} = 20$ A. As the loop Q-factor is not more than a unity, the voltage present at the complementary reactor, can be taken to be $U_{c.com} = 80$ V. Therefore, the magnitude of capacitive impedance with be equal to $X_c = 4$ Ohm/r. Let us determine the capacitance of complimentary reactor $C_{com} = 1/2\pi f X_c = 800$ μF. At resonance setting up, let us calculate the leakage inductance of the complimentary loop by the following equation: $L_s = 1/4\pi^2 f^2 C_{com} = 5$ mH.

As follows from the above calculation, welding transformer (*WT*) should be made so that one of its secondary windings had a very strong leakage. In terms of design (Figure 1), this is achievable by making the complementary winding $w_{2.2}$ in a narrow section of the main secondary winding $w_{2.1}$. Now, when it is impossible to provide this condition by design methods, it is necessary to mount a complementary choke between key *K1* and main reactor C_m.

Block diagram of a two-loop welding unit, implementing the above approach, is given in Figure 1. Winding $w_{2.1}$, thyristor block (*TB*) and reactor C_m form the main secondary loop, and winding $w_{2.2}$, key *K1*, complementary reactor C_{com} form the complementary secondary circuit. In open-circuit mode the phase regulator of welding current (PRWC), the operation of which is synchronized with the mains voltage, is brought into a condition, in which a not more than 12 V voltage is present at *TB* output. During welding, a signal, used for switching on key *K1*, appears at the output of former (*Former*), that is connected in parallel to C_m. Key *K1* is required for switching off the difference current, that should have been generated in the open-circuit mode, because of the voltage difference between windings $w_{2.1}$ and $w_{2.2}$. So, in the stand-by mode, preceding the start of welding, key *K1* is open, and *TB* is in the cutoff mode, in which effective voltage of 12 V is present at reactor C_m. The main loop circuit is open, and no current flows through C_m, and, therefore, the voltage on its plates is close to zero. When the electrode touches the item, voltage is induced in C_m, that is used to switch on *Former*. A signal appears at its output, that simultaneously closes key *K1* and switches *PRWC* into the mode of smooth adjustment of *PRWC* welding current. To prevent thermal overload of the main capacitive reactor, the unit incorporates a thermosensor (*TS*), that uses key *K2* to interrupt the signal controlling the thyristor block. Thus, the main welding current is interrupted, voltage on C_{com} drops, and the channel of complementary current formation, is switched off by a signal from *Former* output.

The stage of the welding process termination should be described in somewhat greater detail. When

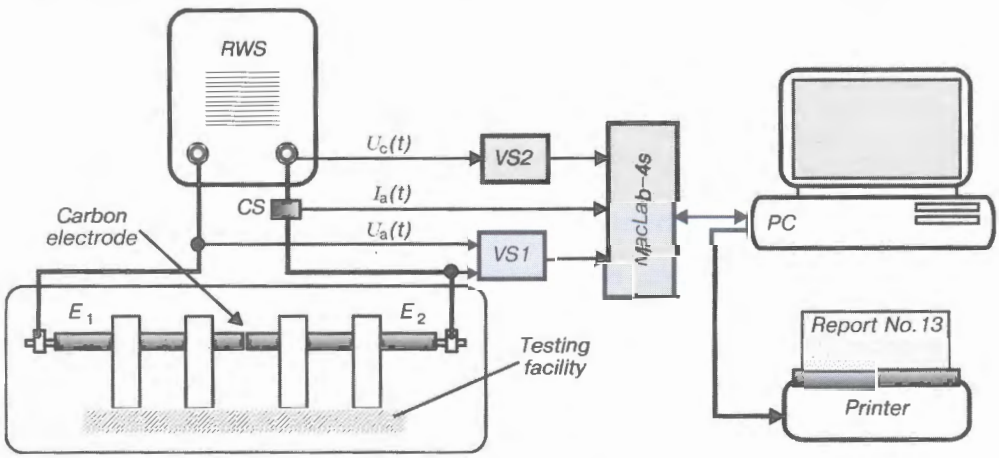

Figure 4. Experimental set up for studying the welding arc elasticity

the welding circuit is opened, voltage on C_m drops by an exponent, the time constant of which is preset in the former block so that switching off time did not exceed 1 s. Key *K1* should go off somewhat earlier, depending on the output voltage of *Former* discriminator.

Time diagrams, illustrating the unit operation, are given in Figure 2. In point *A* (see Figure 1) summation of the main I_m and complementary I_{com} current, formed by the high-voltage loop, is performed. Thus, the welding current is $I_{sum} = I_m + I_{com}$.

The above approach was implemented in practice in a source, the circuit of which is shown in Figure 3, *a*. This unit is a two-loop circuit of a changeable structure, as the electromagnetic element (*EME*) has different functions, depending on the operational mode. In the open-circuit mode *EME* is a choke, connected in series with complementary reactor C_{com}. Complementary current, generated by the complementary series resonance loop, facilitates the conditions for initial arc excitation. Going over to the welding mode, when electronic key (*Key*) is closed, *EME* becomes a step-up transformer. Its output voltage, exceeding U_2 2.0 – 2.5 times as to its level, provides a high stability of the welding arc, even when electrodes with a basic coating are used. Figure 3, *b* gives the curves, describing the external characteristic of the welding unit.

Experimental evaluation of the arc breaking length L_b for the above electrodes was conducted in a facility, the block diagram of which is shown in Figure 4. A unit, described in [7] was used as arc process analyser. This unit is a computer system on Apple platform, fitted with appropriate sensors of current (*CS*) and voltage *VS1* and *VS2*, as well as system interface *MacLab-4s*.

The elasticity of a welding arc running between two horizontal electrodes, was studied by a procedure, suggested in [8]. The arc was excited using a carbon electrode, closing the arc gap, the length of which was preset to be 0.5 mm. After the arc extinction, slide callipers were used to measure length L_b. All the measurements were taken for four values of open-circuit voltage of the main circuit in the resonance welding source (*RWS*), namely 30, 33, 36 and 39 V and electrodes of the same diameter of 3 mm.

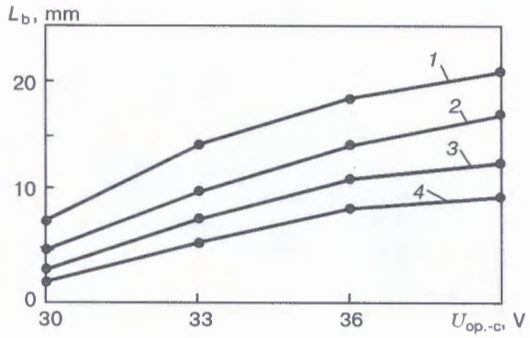

Figure 5. Dependence $L_b = f(U_{op.-c})$ for different electrodes of 3 mm diameter: *1* – *3* – two-loop circuit; *4* – single-loop circuit

The results of testing in the form of a functional dependence $L_b = f(U_{op.-c})$ are given in Figure 5. The obtained data indicate that the arc breaking length is significantly increased with the two-loop circuit. Comparison of curves also shows that for basic electrodes (curves *1* and *4*), L_b increases by 70 – 80 %. The rutile electrodes (curves *2* and *3*), that practically do not excite the welding arc with the single-loop circuit, have a rather high stability in the two-loop circuit. For instance, for $U_{op.-c} = 36$ V the arc breaking length was 11.0 and 7.5 mm, respectively. At $U_{op.-c} \leq 33$ V, with basic electrodes, however, it was not possible to ensure a stable process even with the two-loop circuit.

REFERENCES

1. (1978) *Technology and equipment for fusion welding*. Ed. by G.D. Nikiforov. Moscow: Mashinostroyeniye.
2. Paton, B.E., Lebedev, V.K. (1966) *Electrical equipment for arc and slag welding*. Moscow: Mashinostroyeniye.
3. Paton, B.E., Zavadsky, V.A. (1954) Pulsed arc ignition with the aim of a significant lowering of open-circuit voltage of the welding transformer. *Avtomaticheskaya Svarka*, **4**, 7 – 10.
4. Chernov, A.V., Poletaev, Yu.V., Kavrishvili, Z.O. *et al.* (2000) Improvement of arcing stability in coated-electrode welding. *Svarochnoye Proizvodstvo*, **2**, 7 – 9.
5. Lebedev, V.K., Korotynsky, A.E. (1994) AC arc in a circuit with inductance and capacitance, connected in series. *Avtomaticheskaya Svarka*, **12**, 47 – 48.
6. Lebedev, W.K., Korotynskij, A.E., Zuk, G.W. (1997) O niektorych wlasnosciach procesu spawania lukowego z wykorzystaniem zrodel zasilania z obwodem resonansowym LC. *Biuletyn Instytutu Spawalnictwa*, **3**, 34 – 36.
7. Paton, B.E., Korotinskij, A.E., Skopjuk, M.J. (1997) Programowalny interfejs MacLab do tworzenia systemow informacyjno-pomiarowych w spawalnictwe. *Ibid.*, **3**, 27 – 30.
8. Arlauskas, V.Yu., Narushkevichyus, I.R., Dubashinsky, V.M. *et al.* (1974) Investigation of elasticity of the welding arc with power supply from a source with an inductance and capacitance. *Svarochnoye Proizvodstvo*, **10**, 14 – 16.